Optical spectroscopy and applications of atomically precise graphene nanoribbons: from light emission to photodetection

Dissertation
zur
Erlangung des Doktorgrades (Dr. rer. nat.)
der
Mathematisch-Naturwissenschaftlichen Fakultät
der
Rheinischen Friedrich-Wilhelms-Universität Bonn

von
Seyed Khalil Alavi Eshkaftaki
aus
Shahrekord, Iran

Bonn 2020

Angefertigt mit Genehmigung der Mathematisch-Naturwissenschaftlichen Fakultät der Rheinischen Friedrich-Wilhelms-Universität Bonn

1. Gutachter: Prof. Dr. Klas Lindfors
2. Gutachter: Prof. Dr. Dieter Meschede

Tag der Promotion: 14.07.2020
Erscheinungsjahr: 2020

Abstract

Atomically precise graphene nanoribbons (GNRs) are narrow stripes of graphene with a width of a few atoms and a well-defined edge structure. On-surface synthesis of GNRs from molecular precursors enables atomic precision in producing GNRs with identical width and edge topology. This allows synthesizing GNRs with tunable electronic and optical properties that hold promise for exploration of fundamental materials physics and applications in the next generation of nanoscale electronic and optoelectronic devices. In the present work, the optical properties of such GNRs are explored and they are applied to demonstrate nanoscale photodetectors.

The first study of this work was dedicated to exploring the photophysics of single layers of aligned seven-atom wide armchair GNRs (7–AGNRs) in order to answer the question of whether such GNRs are fluorescent. For this purpose, polarized photoluminescence (PL) and Raman microspectroscopy were carried out in the visible spectral range. It is found that the GNRs are intrinsically dim as a result of non-radiative transitions. This is analogous to their sister materials, carbon nanotubes (CNTs). I discovered that the GNRs could be rendered bright through a photo-induced brightening mechanism in which localized defects are created in the GNRs under laser exposure in ambient conditions. The process of defect formation is activated by continuous low-power blue laser illumination. This mechanism facilitates controlled local modification of the PL emission of GNRs, which enables patterning of microscopic emitting structures. This is in contrast to chemically-driven methods to induce defects, which are commonly used to render CNTs bright.

Extinction spectroscopy was applied to gain additional insight into the role of defects on the PL brightening of GNRs. For this purpose, I measured the extinction spectrum of a single-atom-thick layer of the GNRs. The extinction is anisotropic in accordance with the structure and alignment of the GNRs. The results reveal the dominant presence of excitonic effects in optical response, which is consistent with earlier work. In pristine GNRs, one of these features spectrally coincides with the peak of PL emission (at 1.8 eV) in defected GNRs. Observation of a decrease in the intensity of this feature upon formation of defects, and its relation with PL increase, suggests that this originates from a quenching state in the energy structure of pristine GNRs. The absorption of GNRs is significantly higher than that of graphene due to excitonic effects, making them interesting for photodetection.

In the final part of the work, I harness the merit of atomically precise GNRs for photodetection in the visible range. The fabricated photodetectors consist of a single layer of aligned 7–AGNRs placed between source and drain electrodes. The channel length of preliminary devices is larger than the length of GNRs. Thus the electrical transport is mediated by charge hopping between GNRs, being distinct with respect to transport in graphene. The dark current of the photodetectors in photoconductive operational mode is low in comparison to graphene photodetectors while the responsivity is similar.

This thesis presents the photophysical properties of semiconducting AGNRs and successful application of them to demonstrate atomically-thin photodetectors. With this work, I introduce the application of GNRs in optoelectronic devices.

Parts of the present thesis have been published in the following articles:

[1] **B. V. Senkovskiy**, **M. Pfeiffer**, **S. K. Alavi**, A. Bliesener, J. Zhu, S. Michel, A. V. Fedorov, R. German, D. Hertel, D. Haberer, L. Petaccia, F. R. Fischer, K. Meerholz, P. H. M. van Loosdrecht, K. Lindfors, and A. Grüneis, *Making Graphene Nanoribbons Photoluminescent*, Nano Letters **17**, 4029–4037 (2017).

Author's contribution: The author carried out the wavelength-dependent Raman and photoluminescence experiments in ambient conditions. He independently realized the defect-driven brightening of graphene nanoribbons. He took part in preparation of the manuscript.

[2] **S. K. Alavi**, B. V. Senkovskiy, M. Pfeiffer, D. Haberer, F. R. Fischer, A. Grüneis and K. Lindfors, *Probing the origin of photoluminescence brightening in graphene nanoribbons*, 2D Materials, **6**, 035009 (2019).

Author's contribution: The author performed all the optical measurements, and interpreted the data together with Klas Lindfors. He contributed to the writing of the manuscript together with co-authors.

Parts of the present thesis have been submitted for publication:

[3] **S. K. Alavi**, B. V. Senkovskiy, D. Hertel, D. Haberer, Y. Ando, K. Meerholz, F. R. Fischer, A. Grüneis, and K. Lindfors, *Photodetection using atomically precise graphene nanoribbons*, submitted for publication (2020).

Author's contribution: The author took part in preparation of photodetectors together with Klas Lindfors. He equipped a confocal microscopy setup for optoelectronic measurements and carried out all the electrical and optical characterizations. The author interpreted the data together with Klas Lindfors. He contributed to the writing of the manuscript together with co-authors.

Contents

CHAPTER 1

Introduction

Since the discovery of novel phenomena in single layer of graphene by Geim and Novoselov in 2004, two-dimensional (2D) materials have turned into a hot topic discovering novel aspects of matters and investigating fundamental physics in low dimensions. The term 2D material here refers to single layers of atoms with the thickness of few angstroms. These individual layers, which stacked and bound together with weak van der Waals forces, form bulk 3D stacks. Due to strong quantum confinement, the individual layers often have highly different properties with respect to bulk materials and this makes them attractive for exploration of fundamental physics as well as for technology purposes.

Weak van der Waals forces between the individual layers aid to easily decouple the single layers. As an example, mechanical exfoliation is a traditional method to isolate the single layers from bulk. This was the method that led to discovery of graphene, i.e. a single layer of carbon atoms forming a hexagonal honeycomb lattice, which was exfoliated from bulk graphite.

The extraordinary properties of graphene and its use in the demonstration of devices has promoted significant interest in exploring other 2D materials. In particular, for optical and optoelectronic applications, semiconducting 2D materials are preferred to graphene, which has a vanishing bandgap. transition metal dichalcogenides (TMDs), black phosphorus (BP), and hexagonal boron nitride (hBN) are examples of materials beyond graphene. The TMDs are semiconductors and exhibit a transition from indirect bandgap in bulk to direct bandgap for single layers [4]. They have the chemical structure MX_2 with M being a transition metal layer, e.g., Mo, W, and Re, and X is a chalcogen, e.g., S, Se, and Te. Graphene and TMDs together with BP and hBN cover a broad range of properties from metal to semiconductor and large bandgap insulators. A schematic illustration of selected 2D materials is shown in Fig. 1.1a.

Demonstration of electronic and optoelectronic devices based on 2D materials has already revealed their merit. These often have features such as transparency, flexibility, and small dimensions with respect to analogous devices based on 3D bulk materials. Combination of different 2D materials in the form of, e.g., heterostructures is an avenue to develop entirely 2D devices. The coupling between 2D layers is provided by van der Waals forces with no concern about lattice mismatch [5–7]. This allows harnessing the full advantage of 2D materials for a variety of devices [8].

The collection of 2D materials is growing fast thanks to the development in fabrication and synthesis techniques. It has even expanded to novel quasi-1D and modified 2D materials. Presence of defects and disorder in the lattice of 2D materials leads to significant changes in their properties such that the material acts as a completely different type of material [9]. An example of such modification is

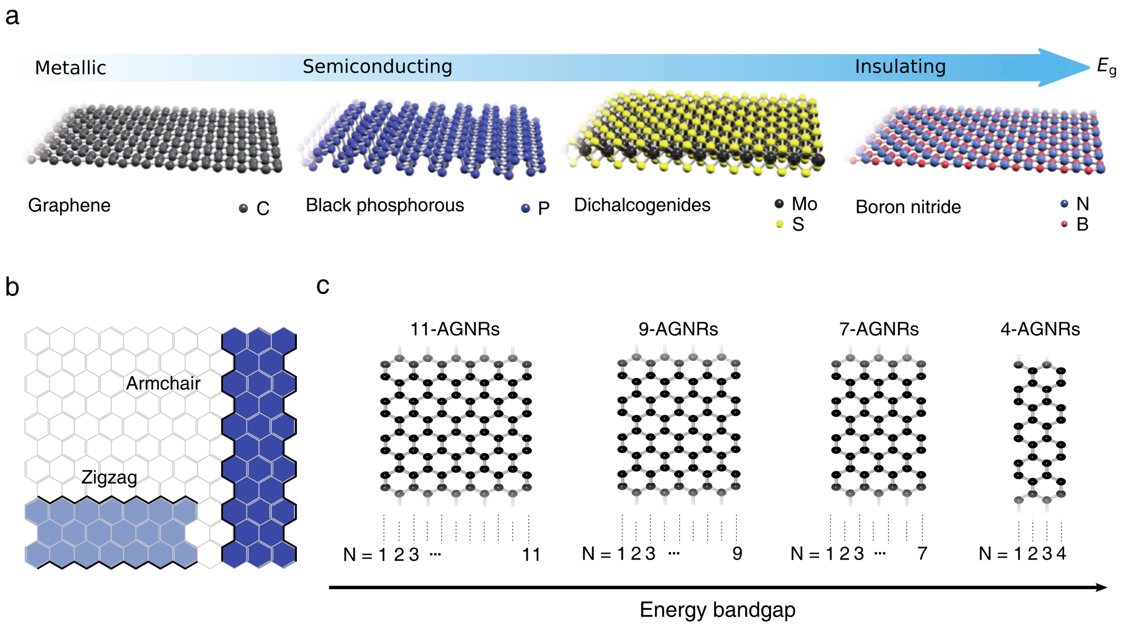

Figure 1.1: **a** schematic illustration of selected 2D materials with atomic structures. The materials are sorted as a function of the energy bandgap, covering a broad range of properties from metal to insulators (adapted from [7]). **b** Two edge morphologies, i.e. Armchair and Zigzag forms of the edges of the GNRs are schematically depicted. **c** The armchair GNRs with different widths (4, 7, 9, 11–AGNRs) are sorted as a function of their bandgap.

creation of color centers in hBN that can act as single-photon sources operating at room temperature [10, 11]. A further modification, which is demonstrated to modify the properties of 2D materials, is to reduce the lateral dimensions to nanometric scales. For example, nanostructures of graphene have been investigated extensively. Fabrication of quantum dots (QDs) [12–14], nanoporous [15], and nanoribbons [16–18] of graphene for different purposes have been reported. A distinct feature of these nanostructures, in comparison to graphene, is opening of a bandgap due to quantum confinement in the plane of the graphene lattice. Opening a bandgap is attractive for optical applications. Interestingly, the bandgap is dimension and edge-profile dependent, meaning that it can be tuned for the desired application. As an example, Fig. 1.1c shows schematic of selected graphene nanoribbons, which are sorted according to their bandgap (see section 2.1.2).

Graphene nanoribbons are a fast growing family of graphene nanostructures with promising properties. The GNRs have traditionally been fabricated using dry or wet etching of graphene, chemical techniques, or unzipping of carbon nanotubes (CNTs) (further explained in section 2.1.1). In 2010 first GNRs were synthesized via polymerization of precursor molecules on gold substrate [19]. This was the first attempt to introduce a novel fabrication method to make these class of carbon-based materials with atomically control over the whole structure. On-surface grown GNRs, also known as atomically precise GNRs, are the central materials investigated in this thesis.

The work presented in this thesis includes the results of our experiments, which provide a better understanding about the optical properties of semiconducting atomically precise armchair GNRs with 7–atom width (7–AGNRs). The results are explained in chapters 3 and 4. For this purpose, spatially resolved Raman, fluorescence, and transmission spectroscopy were performed. One of the key findings of the spectroscopic studies was the observation of high absorption of 7-AGNRs in the visible spectral range. This was the motivation for exploring photodetection using 7-AGNRs. These experiments are discussed in chapter 5.

In chapter 2, a detailed but non-exhaustive review of the scientific background relevant to the thesis is presented. This chapter begins with a brief introduction on different GNR fabrication methods, followed by a discussion about the general properties of GNRs. Due to the high degree of confinement, many-body effects are significant. Both self-energy and excitonic phenomena, as examples of such effects, are described. The next topic is the basics about light-matter interaction and Raman scattering processes in GNRs. Demonstrated nanoscale electronic and optoelectronic devices are the final section in this chapter. Here the most developed devices based on 2D materials such as field-effect transistors and optical detectors are discussed in more detail.

The experimental results of the optical characterization of the GNRs are summarized in chapters 3 and 4. Chapter 3 presents the investigations on photoluminescence emission in GNRs. The results show that the emission from pristine GNRs is low. I explain how we can activate a reaction process under laser exposure in which defects are formed into the GNRs, and as a consequence, the ribbons evolve to be bright emitters. The effect of defects is probed in the extinction spectra of GNRs. This topic is summarized in chapter 4. Further characterizations of defects induction, i.e. wavelength dependence, reaction rates, and the role of environment is also explored.

Chapter 5 presents the demonstration and characterization of the first photodetector based on atomically precise GNRs. Wavelength and polarization selectivities, and low dark current are the key advantages of the developed photodetector in comparison to graphene-based devices. I explain that the mechanism of photodetection is mainly photoconductive for which an external bias voltage provides collection of photocarriers generated in the GNRs. In addition to photoconductive mechanism, absorption of light at the metallic electrodes contributes to photodetection. I show how we can resolve the contribution of individual effects through polarization-resolved experiments. This project paves the way to exploit GNRs in integrated photonic devices on chip. Furthermore, operating the devices with channels longer than the length of GNRs represents a complex platform of carrier transport including several electrical transport mechanisms, that is a fascinating field for theorists and further fundamental investigations.

CHAPTER 2

Scientific background

2.1 Atomically precise graphene nanoribbons (GNRs)

2.1.1 Nanostructuring of graphene

As discussed in chapter 1, graphene is a semiconductor in which conduction and valence bands converge at the Dirac points, i.e. a semiconductor with zero bandgap. It is possible to induce a bandgap in graphene by means of quantum confinement through structuring the graphene sheet. Graphene nanoribbons (GNRs) and graphene quantum dots (GQDs) are examples of such structures [12–14]. In GNRs, the energy structure is significantly modified upon confinement in their width direction with respect to the graphene sheet. It was shown that the GNRs with the width below 10 nm exhibit opening of a bandgap in their energy structure [20]. The results are in agreement with theoretical calculations, which suggest that the band opening is a result of both quantum confinement and edge effects (see section 2.1.2) [20–22]. In general, the techniques to fabricate GNRs can be classified into two groups: top-down and bottom-up approaches [16, 23–25]. In the top-down approach, the fabrication is based on cutting a continuous graphene sheet into smaller structures. In this approach, the methods can be additionally employed to prepare alternative nanostructured forms of graphene [26–29]. In the bottom-up approach, the fabrication process consists of assembling small precursor molecules to form desired GNRs. These approaches are discussed in the following.

Top-down approach

Etch-patterned GNRs. GNRs with nanometer-scale dimensions can be prepared using electron beam lithography (EBL). Here, graphene is covered with an EBL resist with desired patterns, which have been obtained by patterning in an EBL writer. The material is then exposed to oxygen plasma. The covered parts of graphene remain after etching with oxygen, resulting in graphene nanostructures in the form of the exposed pattern in the resist. The minimum width of the GNRs fabricated with this method is limited to 10 nm [30, 31], and therefore fabrication of few atoms wide GNRs is not achievable via this method.

Additionally, local probes such as scanning tunneling microscope (STM), transmission electron microscopy (TEM), and atomic force microscopy (AFM) have been used to etch graphene and produce GNRs. The STM probe has been employed to produce below 10 nm wide stripes in highly-oriented pyrolitic graphite (HOPG). Fabrication of GNRs with TEM was demonstrated using high energy electron beam exposure to pattern sub-nanometric (0.7 nm) GNRs [32]. These techniques facilitate extremely high spatial control to produce GNRs. Nevertheless, control over the edge profile of produced GNRs with atomic precision is not possible in this way.

Sonochemical-synthesized GNRs. This is another route that is developed to fabricates GNRs. Li *et al.* used chemically-exfoliated graphite as the base material to produce well-defined zigzag or armchair GNRs with sub-10 nm width [20]. In this method, exfoliated graphite undergoes a sonochemical reaction to produce dispersed GNRs in solution. Although the fabricated GNRs have well-defined edge profile, production of identical GNRs with the same edge and width remains challenging. Furthermore, the produced GNRs are not isolated and they are in network phase and aggregated together.

Unzipping of CNTs. Unzipping of single-walled CNTs (SWCNTs) or multi-walled CNTs (MWCNTs) is a chemical method to prepare GNRs. We note that this method can be viewed as a combination of both bottom-up and top-down approaches. In fact, the CNTs are fabricated via bottom-up approach using individual molecules. This provides the advantages that CNTs with a variety of chiralities and diameters can be produced and are available. The dispersion of CNTs in oxidative solution leads to unzipping of their walls [33]. Additionally, unzipping of SWCNTs has been reported on SiO_2/Si substrates. In this method, SWCNTs were exposed to zinc by sputtering and then dissolved in HCl aqueous solution [34]. These processes form GNRs with the width depending on the used CNTs. Similar to the etch-patterned method, the fabricated GNRs do not possess well-defined edge profiles.

Bottom-up approach

Generally speaking, the core idea in this approach is to produce larger structures out of small precursor molecules. The reactions between the precursor molecules can take place in solution or on surfaces. These are the two routes.

Solution-based GNRs. Production of GNRs in large quantities with well-defined widths is possible through chemical reactions. These reactions can be activated in proper solutions in which pre-synthesized molecular monomers link together to form polymers and finally produce GNRs. The ribbon width can be as narrow as 1 nm with the lengths >100 nm [18, 35]. Nevertheless, similar to the sonochemical method, the produced GNRs are synthesized in the form of network with random orientations.

On-surface grown GNRs. Polymerization of precursor molecules on catalytic surfaces is an alternative approach. The process facilitates fabrication of GNRs with different widths from tens of nanometers down to few atoms wide. There is a full control over the structure of the GNRs in atomic scales [36–42]. This results in fabrication of GNRs with the same width and edge profile. Fabrication of GNRs with various width down to narrowest possible GNRs (3-atom wide) have been reported [16, 25, 38–45]. Additionally, GNRs growth can be controlled to produce isolated [46] or network of GNRs in the wafer scale [17, 47]. Even GNRs can be fabricated with specific orientation using proper growth substrate e.g., Au(788), with which the GNRs are grown parallel with respect to each other (see chapter 3 for further details).

In this method, the fabrication process starts by sublimating of precursor monomers on top of metallic substrates like Ag, Cu, or Au [19]. The synthesize steps are schematically illustrated in Fig. 2.1a. In this figure, the growth process is shown for seven-atom wide armchair GNRs (7-AGNRs). These ribbons are obtained using 10,10'-dibromo-9,9'-bianthryl known as DBBA monomers. Initially,

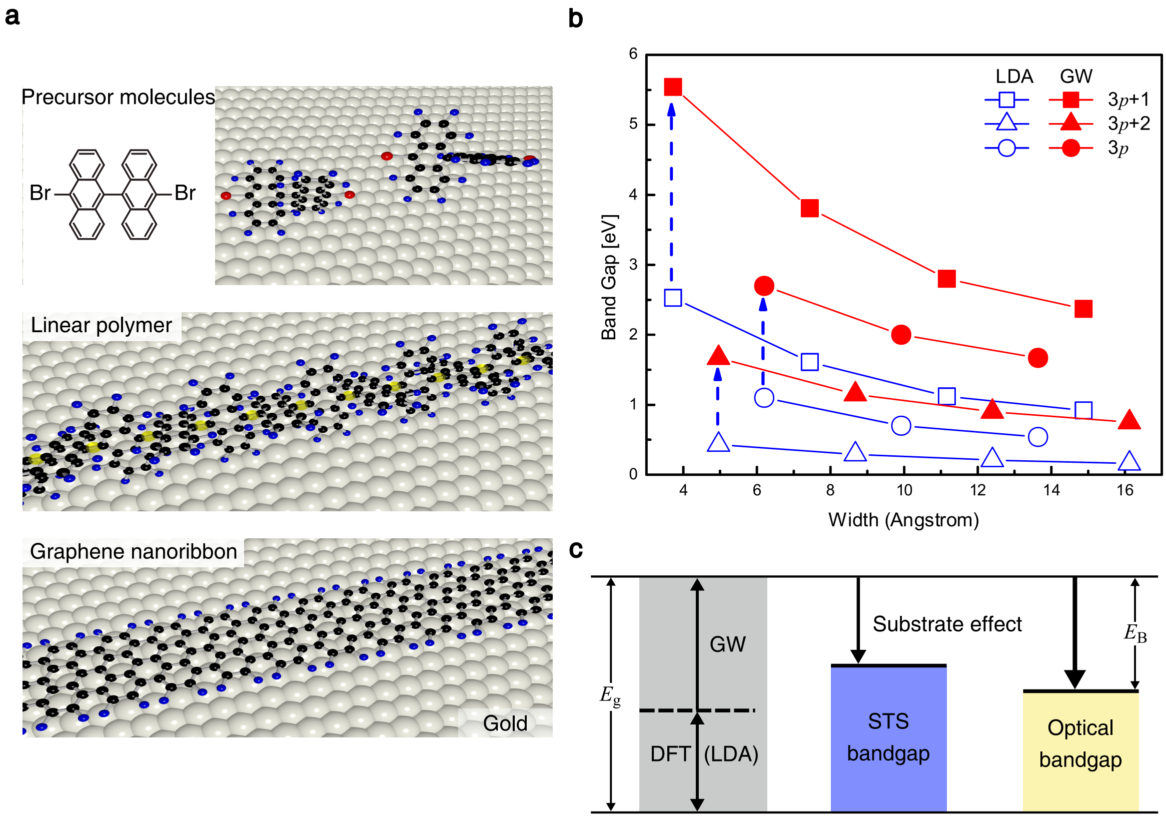

Figure 2.1: **a** Fabrication process of 7–AGNRs on gold substrate. Here carbon, hydrogen, and halogens are shown with black, blue, and red spheres, respectively. The process starts with evaporation of precursor molecules on Au (top). After dehalogenation on the surface, molecules interlink to form linear polymers (middle). Cyclodehydrogenation is the last step to make GNRs (down). **b** Energy bandgap as a function of ribbon width for three families of AGNRs. DFT calculations in LDA approximation (blue) show the bandgaps increase for narrower GNRs for all the families. Including many-particle interactions in GW framework results in an increase in the bandgaps (red) as a result of band renormalization (taken from [48]). **c** Summary of the relation between electronic bandgap for 7–AGNR, calculated with DFT and GW approximation, the reduced bandgap due to substrate screening effect, and their optical bandgap. The electronic bandgap in STS is measured on a metallic substrate, and thus it is inherently lowered. The optical bandgap is smaller than electronic bandgap with the amount of E_B.

the monomers are sputtered on catalytic metal, i.e. Au(111) (Fig. 2.1a: top panel). The pre-heated substrate (200 °C) leads sublimantation of the monomers. This results in removing of their halogen substituents, which is a prerequisite step to produce polymer chains (Fig. 2.1a: middle panel). The process continues with dehydrogenation of polymer chains with further heating (400 °C), resulting in formation of 7–AGNRs (Fig. 2.1a: lower panel).

2.1.2 Properties of GNRs

The properties of the GNRs are determined by their edge topology and width [24, 36, 37, 42, 49–51]. Both can be controlled by the direction of polymerization and selecting the proper precursors [19]. Depending on the edge profile, the GNRs are classified into two main types, namely armchair or zigzag (as shown in Fig. 1.1b).

The band structure of GNRs have been investigated in many theoretical works. The results obtained with tight-binding (TB) model, density functional theory (DFT) within the local density approximation (LDA) [21], and many-body perturbation theory [48, 49, 52] are in qualitative agreement. The theoretical works show that the GNRs with armchair edge can be sorted into three different families depending on their width, N. Here, N is the number of carbon atoms along the GNR width. Accordingly, AGNRs belong to the families with

- small bandgap when $N = 3p - 1$
- medium bandgap when $N = 3p$
- large bandgap when $N = 3p + 1$

Here, p is an integer. Figure 2.1b shows the bandgaps of AGNRs as a function of width calculated with both DFT (in LDA approximation) and GW frameworks (further explained in section 2.1.3). We note that in this figure, the family with small bandgap is indicated with $N = 3p + 2$. The bandgap monotonically increases by decreasing the width of AGNRs for each family. Nevertheless, decreasing or increasing individual atoms corresponds to change the family, resulting in a significant change in the bandgap. These predictions are in agreement with experimental results for AGNRs with different widths. The DFT and GW calculated bandgaps and experimentally determined values using scanning tunneling spectroscopy (STS) are summarized in table 2.1.

Unlike AGNRs, the bandgap in ZGNRs does not show family dependence, and it slightly increases with decreasing the GNRs width. The bandgap is significantly smaller for ZGNRs compared to AGNRs with the same width. In fact, in GNRs with zigzag edge, it is found that there exist spin-polarized states at the edge of the ribbons. The DFT calculations, including spin polarization for ZGNRs, reveal a band splitting as a result of antiferromagnetic ordering of these states [21, 48, 53, 54]. These calculations predict a small bandgap. More precise calculations, including quasiparticle corrections, predict a bigger bandgap for ZGNRs. The results show that there is a critical width of 3 nm below which the energy splitting, arising from edge states, significantly increases (1.6 eV for 1.1 nm-wide ZGNRs). This is a result of strong electron-electron interactions. Above 3 nm widths, the splitting stays constant around 0.39 eV. Additional corrections, however, revealed that this energy splitting exhibits width dependence (above 3 nm) [54].

The main focus of the present thesis is on GNRs with armchair profile and later on GNRs refers to AGNRs unless otherwise indicated. Of the families of AGNRs, $N = 3p+1$ ribbons are semiconducting with large bandgap. Thus they are appealing for optical applications. In this thesis, we will focus on seven-atom wide AGNRs (7–AGNRs).

2.1.3 Electronic and optical bandgaps

In a solid state picture, the electronic bandgap of GNRs is defined as the energy difference between highest occupied (valence) band and lowest unoccupied (conduction) band. Many-body effects in such a 1D system with high level of localization significantly modify this energy difference. Here electron-electron (e-e) and electron-hole (e-h) interactions are important and cannot be ignored. The DFT calculations provide reliable information about the band structure of GNRs, but the predicted bandgap may be improperly estimated. A more accurate model is GW approximation in many-body

GNR width	E_g [eV] DFT	E_g [eV] DFT + GW	E_g [eV] Experimental (STS)	Reference
$N = 5$	≈ 0.5	1.7	–	[48]
$N = 7$	1.6	3.7	2.3	[55, 56]
$N = 9$	–	2.1	1.4	[57]
$N = 13$	≈ 1	2.4	1.4	[58]
$N = 14$	0.22	–	0.3	[59]

Table 2.1: The electronic bandgaps for isolated GNRs are calculated in DFT (LDA) and GW frameworks. The GW bandgap is higher due to inclusion of the Coulomb interactions. The calculations are compared with the measurements in scanning tunneling spectroscopy (STS). The measured bandgap is smaller as a result of the metallic substrate screening effect.

perturbation theory (with G and W standing for Greens function and screened interaction, respectively) in which e-e and e-h interactions are included (see Fig. 2.1b). Thus predicted bandgap is in good agreement with experimental measurements [53, 56]. Including the Coulomb interactions in the calculations can be understood by means of the energy diagram shown in Fig. 2.1c. The repulsion of identical charges, known as self-energy, results in an overall increase of the bandgap with respect to the one-particle bandgap ($E_{g,DFT}$, also known as free-particle bandgap). This effect is also known as bandgap renormalization [4, 49, 52].

Nevertheless, the theoretical predictions of the electronic bandgap for isolated GNRs could significantly differ from the measured values. In fact, the experimental results are strongly affected by the substrate. Scanning tunneling spectroscopy (STS) of 7-AGNRs on Au(111) is an example of such effect, where the measured electronic bandgap (2.3−2.4 eV) shows around 1.4 eV smaller value compared to the theoretical prediction (3.7 eV in GW approximation) for isolated 7-AGNRs [55]. The STS results, shown in table 2.1 for different GNRs, also involve this energy reduction. This measured bandgap is also known as transport bandgap (Fig. 2.1c). To compensate the substrate effect in the calculations, image corrections can be included (IC) [56]. Indeed, this phenomenon is a direct result of the screening effect of metallic surface on the band structure of GNRs, hinting of the extreme sensitivity of the electronic bandgap of GNRs to the environment. This effect is well-known and studied for low-dimensional systems [60]. Interestingly, it was shown that in such systems as well as GNRs, the screening effect has a minor influence on the optical bandgap [17, 56].

The optical bandgap corresponds to the lowest photon energy required for optical excitation of an electron from an initial state (in valence band) to a final state (in conduction band), and leaving a hole in valence band. In typical bulk semiconductors, the energy for this excitation is the same as the electronic bandgap. In GNRs, due to extreme confinement, the generated e-h are strongly bound together, consequently forming an exciton. In general, this effect is enhanced in media with high degree of confinement, e.g., 2D materials [4]. Thus their optical properties are dominated by excitonic effects. The difference between electronic and optical bandgap (e.g., for an isolated ribbon) is equivalent to the exciton binding energy E_B (see Fig. 2.1c) [56]. For single layer TMDs, this energy is typically in the range of 0.5 eV [4]. It is also high in 1D systems such as CNTs (from few tens of meV to 1 eV) [61] and AGNRs (e.g., 1.8 eV for 7-AGNRs) [56]. Since the excitons substantially alter the optical features of GNRs, in the next section a brief review about them is presented.

2.1.4 Excitons

In semiconductors, absorption of a photon promotes an electron to conduction band and leaves a hole in valence band. The Coulomb force between generated electron and hole may lead to formation of a bound system known as exciton. This quasiparticle is electrically neutral and can transport energy in the material while having no net charge. The attractive Coulomb force suggests that the excitonic states have lower energy than the energy band for free particles. The strength of interaction between electron and hole determines the spatial delocalization of exciton as well as its binding energy. If the attractive force is strong, e.g., in ionic crystals, the electron and hole are strongly bound together and localized on the scale of the lattice unit cell. Such excitons are known as Frenkel excitons. This is not commonly the case in bulk semiconductors, since the screening by electrons in valence band reduces the attraction between hole and electron. In this case, the excitons are known as Wannier-Mott excitons [62].

Under the assumption of weak Coulomb interaction between electron and hole, the effective mass approximation is valid, and the exciton wavefunction can be expressed as a linear product of electron and hole wavefunctions. For an exciton with wavefunction ϕ_{exc}, the Schrödinger equation is written as [63]

$$\left[\frac{p_{\mathrm{e}}^2}{2m_{\mathrm{e}}^*} + \frac{p_{\mathrm{h}}^2}{2m_{\mathrm{h}}^*} - \frac{e^2}{\epsilon|\mathbf{r}|}\right]\phi_{\mathrm{exc}} = E_{\mathrm{exc}}\phi_{\mathrm{exc}} \,. \tag{2.1}$$

Here $p_{\mathrm{e,h}}$ and $m_{\mathrm{e,h}}^*$ are momentum and effective mass of electron and hole, respectively, and ϵ corresponds to the dielectric constant, and $\mathbf{r} = \mathbf{r}_{\mathrm{e}} - \mathbf{r}_{\mathrm{h}}$ is a vector connecting the position of the hole and electron. In order to solve Eq. 2.1, the motion can be separated into the relative motion of electron and hole, and the motion of the center of mass (CM). Solving the equation for CM coordinate gives the kinetic energy of the exciton

$$E_{\mathrm{kinetic}} = \frac{\hbar^2 k^2}{2(m_{\mathrm{e}}^* + m_{\mathrm{h}}^*)} \,, \tag{2.2}$$

with k as the wavenumber of the exciton. The part of the Schrödinger equation for the relative motion of electron and hole is similar to that for the hydrogen atom. The corresponding eigenvalues (energy levels) are

$$E_{\mathrm{r}}(n) = E_{\mathrm{g}} - \frac{R^*}{n^2} \,, \tag{2.3}$$

where $R^* = (1/m_{\mathrm{e}}^*\epsilon^2) \times 13.6$ eV is the exciton Rydberg constant, and n is the quantum number [62]. Thus the total exciton energy is given as

$$E_n = E_{\mathrm{g}} + \frac{\hbar^2 k^2}{2(m_{\mathrm{e}}^* + m_{\mathrm{h}}^*)} - \frac{R^*}{n^2} \,. \tag{2.4}$$

Equation. 2.4 represents the energy as a series of excitonic states below the bandgap with quantum number $n = 1, 2, \ldots$, and parabolic dispersion. This interpretation can be extended to 2D semiconductors. Optical absorption for a 2D semiconductor including excitonic and renormalization effects is presented in Fig. 2.2a. The excitonic states located below the FP bandgap in a series with different quantum numbers. The lowest excitonic state determines the optical bandgap [4].

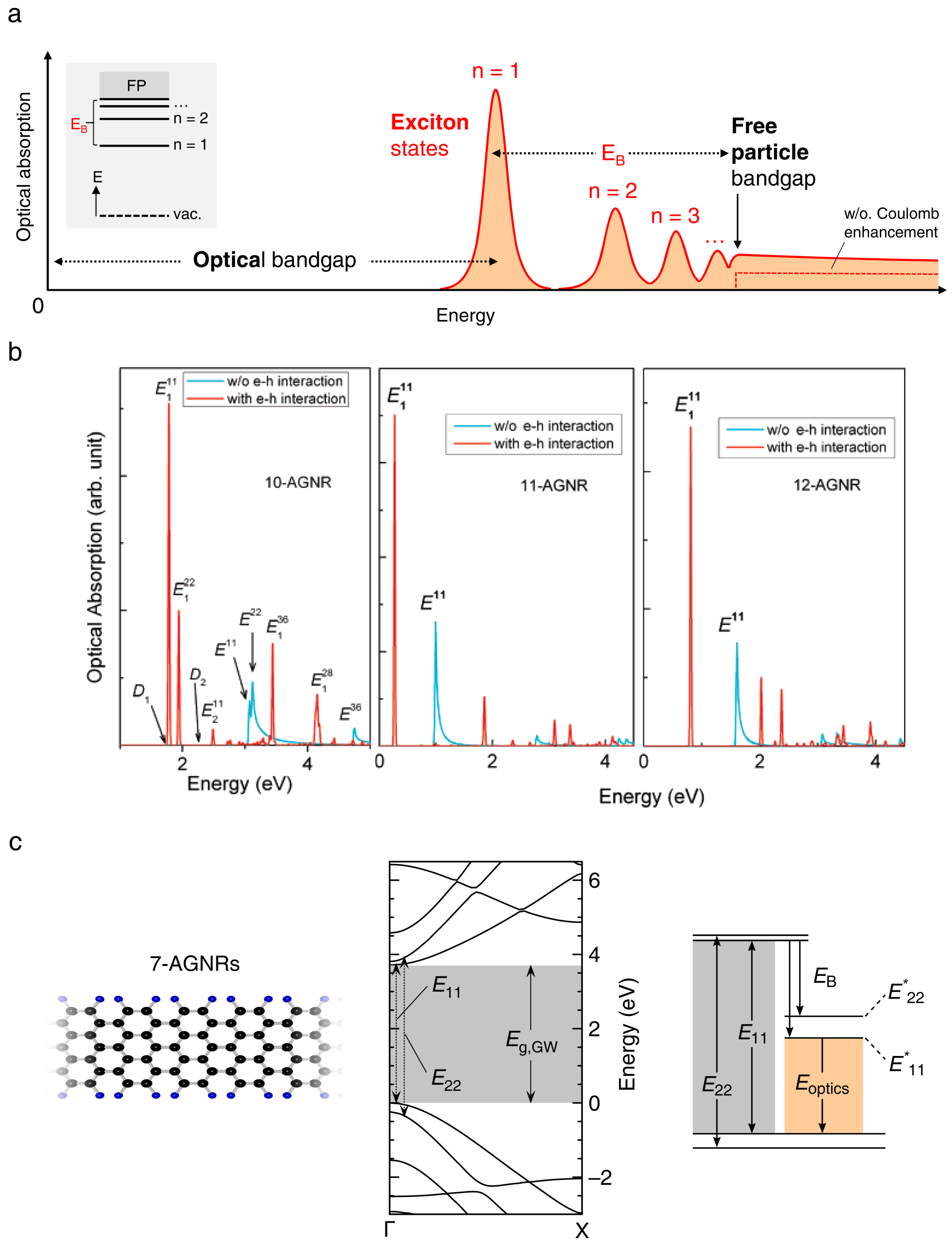

Figure 2.2: **a** Schematic of the absorption spectrum for a 2D semiconductor. Excitonic states are below the free particle (FP) bandgap designated with their quantum number ($n = 1, 2, \ldots$). The first excitonic state corresponds to optical bandgap with a red-shift equal to exciton binding energy (E_B) with respect to FP bandgap. Considering strong Coulomb interactions enhances the absorption above E_g. Inset illustrates the atomic-like presentation of energy diagram with excitonic states below the FP bandgap (taken from [4]). **b** Optical absorption as a function of photon energy with (red) and without (blue) e-h interactions for 10–, 11–, and 12–AGNRs. The transitions from lower excited states (E^{ii}) is red-shifted to E_1^{ii} with $i = 1, 2$ due to e-h interactions. For 10–AGNRs, D_1 and D_2 are predicted dark states (taken from [49]). **c** Schematic view of a hydrogen-terminated 7–AGNRs. Here, carbon and hydrogen atoms are shown with black and blue spheres, respectively. The middle panel shows the Calculated band structure including self-energy effects in GW approximation (taken from [56]). Including excitonic effects introduce two exciton states E_{ii}^* far below E_{ii} excitations as a result of high binding energies (E_B = 1.8 and 1.4 eV for i = 1 and 2, respectively.)

Exciton in GNRs

The binding energies for excitons in bulk semiconductors are typically few tens of meV [62]. Thus the effects involving the excitonic states are more pronounced at low temperatures. In low dimensional system, however, excitons are more important as the binding energy increases due to quantum confinement. The excitons in GNRs are of Wannier-Mott type. They are fully delocalized over the width and extend along the length, depending on the interaction strength [56]. As an example, Yang *et al.* calculated the optical transitions for AGNRs including self-energy (bandgap renormalization) and excitonic effects [49]. Figure 2.2b summarizes the obtained results for AGNRs with $N = 10$, 11, and 12, as examples of the three AGNR families (see section 2.1.2). In this figure, E^{ii} denotes the transition from the ith valence band to the corresponding conduction band when the e-h interactions are excluded (w/o e-h). This is the notation commonly in use to express the energy bands in CNTs and GNRs. Including the excitonic effects in the calculations leads to a noticeable red-shift (E_i^{ii}) with respect to transitions without e-h interactions, as a consequence of high binding energies of the excitons (E_B) in GNRs. The calculations show that for 10–, 11–, and 12–AGNRs, with width of ≈1.2 nm, the exciton binding energies are 1.4, 0.4, and 0.8 eV, respectively. The exciton binding energies are sensitive to the bandgap, and are in accordance with the corresponding AGNR family [49]. In 7-AGNRs, the exciton binding energies are even higher than the values shown in Fig. 2.2b. Figure 2.2c shows the energy band diagram for 7-AGNRs calculated using many-body perturbation theory including self-energy effects. Including e-h interactions reveals the contribution of two low-energy excitons (E_{11}^* and E_{22}^*) with binding energies of 1.8 and 1.4 eV. These features originate from transitions between E_{11} and E_{22} energy bands, respectively (see schematic in Fig. 2.2c) [56].

Dark excitons

When an exciton is generated by absorption of a single photon, it is called a bright exciton. This exciton may undergo scattering events induced by impurities, phonons, electrons, or other excitons, which can lead to spin flip and change in exciton momentum. Such events are pronounced in confined systems. Additionally, various excitons can be formed through more complex processes such as non-resonant optical excitation or by electrical means (see section 2.2.2). Nevertheless, not all of them decay through optically allowed transitions. These transitions can be dipole or spin-forbidden, and in this case, the corresponding excitons are known as dark excitons. Unlike bright excitons, which decay radiatively, these excitons decay through non-radiative channels [4]. For example, in SWCNTs, most of the excitonic states are optically forbidden. These states dramatically contribute to relaxation processes and are the origin of the low quantum efficiency in SWCNTs [64–67]. A more detailed explanation about such states is presented in section 2.2.2, where the origin of low photoluminescence emission in the GNRs is discussed.

2.2 Light-matter interaction

2.2.1 Optical transition

In order to simplify the quantum interpretation of light-matter interaction, first order time-dependent perturbation theory is often employed to explain the optical transition between an initial state ψ_i to a final state ψ_f. This can, for example, be an interband transition between valence (ψ_v) and conduction band (ψ_c). In perturbation theory, the rate of this transition is determined with Fermi golden rule [68]

$$W_{if} = \frac{2\pi}{\hbar}\rho_{\mathrm{j}}(E)\left|\langle\psi_f|\, H\, |\psi_i\rangle\right|^2 \,, \tag{2.5}$$

where $\rho_{\mathrm{j}}(E)$ denotes the joint density of states (JDOS), and H is the Hamiltonian, which represents the perturbation induced by an electromagnetic field to the system. It is convenient to deal with Eq. 2.5 in semi-classical picture in which the matter is described using quantum mechanics but the light is treated classically. Considering dipole transitions, $H = -\boldsymbol{p} \cdot \boldsymbol{E}$. Here $\boldsymbol{p}$ is the electric dipole operator, and $\boldsymbol{E}$ is the electric field of the incident light. Considering that electrons are involved in transition, then $\boldsymbol{p} = -e\boldsymbol{r}$. This is known as electric dipole approximation, with the resulting transition called electric dipole transition. In this approximation, due to momentum conservation, the wavevector of electron in the initial ($\boldsymbol{k}_i$) and final ($\boldsymbol{k}_f$) states does not change ($\boldsymbol{k}_i = \boldsymbol{k}_f$). The corresponding transitions are known as direct or vertical transitions. The factor $\langle\psi_f|\, H\, |\psi_i\rangle$ in Eq .2.5 can be expressed as

$$\langle\psi_f|\, H\, |\psi_i\rangle = e\int \psi_f^*(\boldsymbol{r})\, \boldsymbol{r} \cdot \boldsymbol{E}\, \psi_i(\boldsymbol{r})\, \mathrm{d}^3\boldsymbol{r} \,, \tag{2.6}$$

where $\psi_i(\boldsymbol{r})$ and $\psi_f(\boldsymbol{r})$ are wavefunctions of initial and final states, respectively. Equation 2.6 is known as the transition matrix element. In the case of interaction with a small particle (e.g., molecules), we can assume that $\boldsymbol{E}$ is constant across the particle and write

$$\langle\psi_f|\, H\, |\psi_i\rangle = e\left(\int \psi_f^*(\boldsymbol{r})\, \boldsymbol{r}\, \psi_i(\boldsymbol{r})\, \mathrm{d}^3\boldsymbol{r}\right) \cdot \boldsymbol{E} \,, \tag{2.7}$$

and define the transition dipole moment μ_{if} as

$$\mu_{if} = e\int \psi_f^*(\boldsymbol{r})\, \boldsymbol{r}\, \psi_i(\boldsymbol{r})\, \mathrm{d}^3\boldsymbol{r} \,. \tag{2.8}$$

The dipole moment is a key quantity, which determines the optical response, e.g., in absorption or emission processes. The contribution of specific transition to optical processes is characterized by the oscillator strength of that transition. The oscillator strength f_{if} is given by

$$f_{if} = \frac{2m\omega_{if}}{3\hbar}\left|\mu_{if}\right|^2 \,, \tag{2.9}$$

where ω_{if} is the frequency of the transition from i to f.

Equation 2.6 imposes restrictions on the transitions and defines the selection rules. Since the dipole moment operator has odd parity the dipole transition only occurs if the initial and final states have opposite parities. The selection rules for dipole transitions in AGNRs are similar to SWCNTs [69, 70]. For the incident light polarized along (perpendicular to) the AGNRs, the transitions of E_{11} and E_{22} are allowed (forbidden), while the transitions of E_{12} and E_{21} are forbidden (allowed). Theoretical calculations have shown that the mixture of these two transitions (E_{12} and E_{21}) gives rise to a dark exciton (D_1 in Fig. 2.2b) for the incident light polarized along the AGNRs, which affects the emission of the AGNRs (see section 2.2.2) [49].

2.2.2 Photoluminescence in GNRs

In luminescence, the system decays from an excited state by emitting a photon. This can take place spontaneously resulting in spontaneous emission, or via stimulation by external light fields leading to stimulated emission. To study luminescence, the excitation can be achieved, for example, with optical, electrical, or even thermal means. These processes are known as photoluminescence (PL), electroluminescence (EL), and thermoluminescence, respectively. Chong *et al.* have reported first observation of EL from individual 7–AGNRs [71]. In this work, single 7–AGNRs were suspended between an STM tip and Au(111) surface. By applying a voltage (< 2 V), the GNRs could be excited and consequently emitting light with three narrow (FWHM ≈ 40 meV) emission lines between 1.3 to 1.6 eV.

In PL process, absorption of a photon in a semiconductor promotes an electron from valence band to conduction band, leaving a hole in the corresponding valence band. The excited electron (hole) may undergo a series of low-energy intraband transitions to reach the lowest (highest) state in the conduction (valence) band. This involves interactions such as electron-phonon or electron-traps (see schematic in Fig. 2.3a). This is reminiscent of Kasha's rule for organic molecules, in which radiative decay occurs from the lowest excited state, through recombination of e-h [72]. In GNRs, this corresponds to annihilation of an exciton arising from E_{11} (see Fig. 2.3b). In such PL process, the emitted photon has no phase correlation with the absorbed one and it does not remember the information of exciting photon [62]. This is in contrast with other light-matter interaction processes like resonance fluorescence or Raman scattering (e.g., in molecules), which are coherent processes with strong correlation between absorbed and emitted photons (see section 2.2.4). The radiative rate of the transition for an electron from conduction band to valence band is expressed as

$$\gamma_{\mathrm{cv}} = A_{\mathrm{cv}} f_{\mathrm{e}} (1 - f_{\mathrm{h}}) \,, \tag{2.10}$$

where A_{cv} is the Einstein coefficient for spontaneous emission and f_{c} (f_{v}) is the quasi-equilibrium distribution function in conduction (valence) band. If we assume that the excitation intensity is low, then f_{e} and f_{h} can be considered as Boltzmann distributions. With this assumption, the PL spectra for a band-to-band transition is [62]

$$I_{\mathrm{pl}}(E) \propto \sqrt{E - E_{\mathrm{g}}}\, e^{-\frac{E - E_{\mathrm{g}}}{k_{\mathrm{B}} T}} \,, \tag{2.11}$$

Here $\sqrt{E - E_{\mathrm{g}}}$ is due to the proportionality of emission intensity to the joint density of states in valence and conduction bands. Figure 2.3a represents the asymmetric lineshape of Eq. 2.11 where the spectrum shows a steep slope at the energy position of the bandgap (E_{g}). This simple model fails to explain the experimental results, where transitions from bound, impurity, and excitonic states are involved. In the presence of excitons, for instance in GNRs, the emission of a photon corresponds to annihilation of an exciton with the energy expressed in Eq. 2.4. The lineshape for the emission from exciton considering natural broadening results in Lorentzian peak at photon energies below the bandgap (Fig. 2.3b).

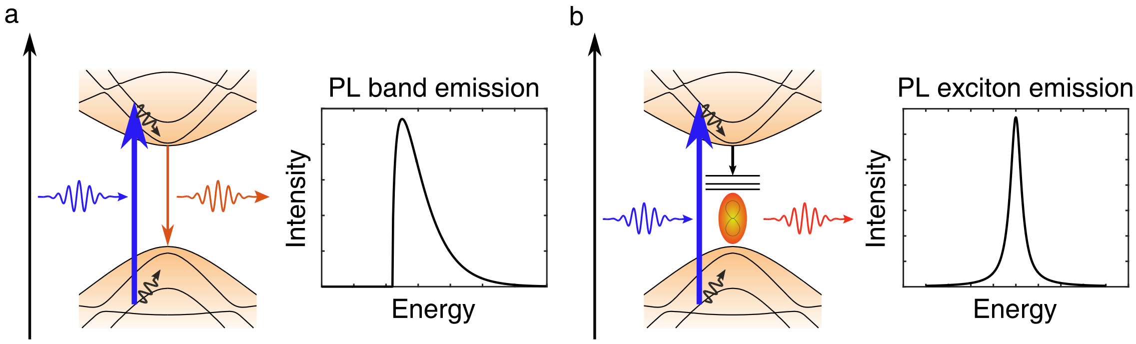

Figure 2.3: **a** The blue arrow shows the process of absorption of excitation photon followed by creation of e-h pair in higher subbands of valence and conduction bands. The created e-h pairs undergo a chain of fast intraband transitions in which electron (hole) relaxes to bottom (top) of conduction (valence) band, and consequently radiatively decays. The band emission spectrum has a sharp edge at the bandgap. **b** In the presence of excitonic states, the radiative transition occurs from the lowest bright exciton at the energy with E_B lower than the fundamental bandgap. The bands are the energy structure of 7–AGNRs calculated in Ref. [56].

Radiative and non-radiative decays

So far, radiative decay as a relaxation channel for the excited states has been discussed. The relaxation processes are complicated by non-radiative processes. Thus, in order to evaluate the dynamics of the excited states, both radiative and non-radiative decays must be considered. Every excited state has a lifetime, which is determined by the rate of both radiative γ_r and non-radiative γ_{nr} transitions. The lifetime of an excited state is given by

$$\tau = \frac{1}{\gamma_r + \gamma_{nr}} . \tag{2.12}$$

The excited state dynamics can be investigated, e.g., in time-resolved PL spectroscopy. Another parameter which reflects the radiative and non-radiative interplay in the relaxation of the excited states is the quantum efficiency η_{QE}. The quantum efficiency is defined as the ratio between the number of emitted photons to the total number of absorbed photons in a unit of time. It can be formulated using the radiative and non-radiative rates as

$$\eta_{QE} = \frac{\gamma_r}{\gamma_r + \gamma_{nr}} . \tag{2.13}$$

It is evident that the limitation for the η_{QE} is dictated by the non-radiative decay rate γ_{nr}. In general, the energy of the excited state in non-radiative decay is dissipated as heat through phonons in semiconductors. Processes like Auger (exciton-exciton recombination), charge-exciton, and free carrier-exciton interactions as well as traps and dark states are more examples leading to non-radiative processes.

Origin of low Photoluminescence in GNRs

Although the optical properties of GNRs have been theoretically studied before [49, 52], it took several years until the first experimental probe of PL was reported [1]. The critical step that made the exploration possible was the technique employed to transfer GNRs from the metallic growth

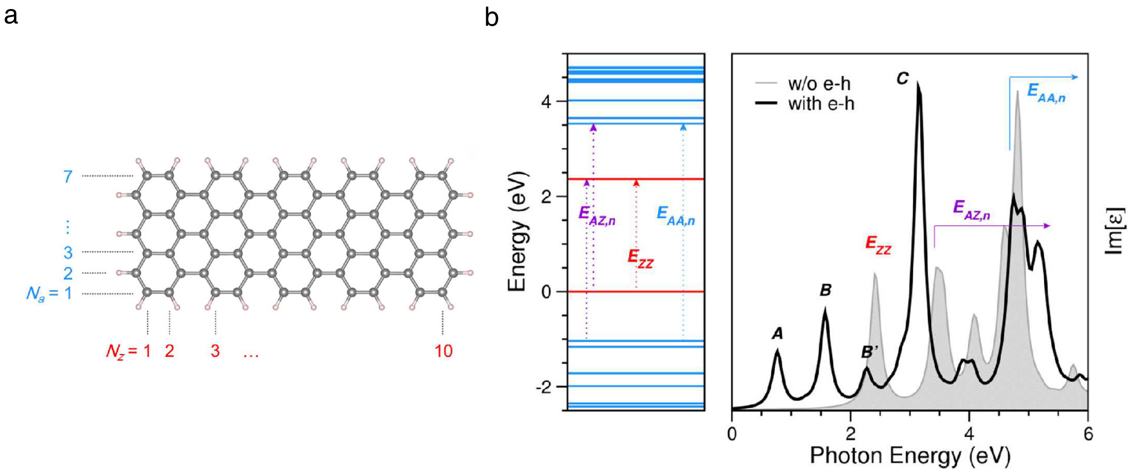

Figure 2.4: **a** A finite 7–AGNRs with the length of 2 nm. The localized (Tamm) states arise from the presence of zigzag edge at termini of the finite GNRs. **b** First principle calculations, considering self-energy effects (GW approximation), show that Tamm states have smaller transition energies (red) than bulk states (blue). Arrows show corresponding transitions between Tamm-Tamm (E_{ZZ}), Tamm-bulk ($E_{\mathrm{AZ,n}}$), and bulk-bulk ($E_{\mathrm{AA,n}}$) states. The right panel shows the absorption spectrum for the same 7–AGNRs with (solid black line) and without (gray area) e-h interactions. Transitions between Tamm states are significantly red-shifted due to high exciton binding energies (peaks A, B, and B') [73].

substrates to insulating substrates (see chapter 3). Emission from GNRs on metal substrates is completely quenched by the metal, requiring the transfer. Nevertheless, η_{QE} for on-surface grown GNRs has not been reported to date. Instead, for a solution-based GNRs, Huang *et al.* have reported near-infrared emission with $\eta_{\mathrm{QE}} \approx 9.1\%$ [74]. They investigated 1.7 nm wide GNRs with an average length of 58 nm in liquid phase.

Similar to SWCNTs, the PL emission in on-surface grown ($N = 7$) GNRs is significantly limited by non-radiative decays. For comparison, in SWCNTs, the reported η_{QE} is in the range $2 - 7\%$ [75]. There, the non-radiative relaxation events are proposed based on two major processes: The first one is phonon-assisted indirect ionization process (PAIEI), which is a typical effect in p-doped SWCNTs [76, 77]. In this process, the exciton decays initially by emitting a single phonon. This is then followed by creation of an intraband e-h pair in the valence band, which provides the conservation of energy and momentum. Eventually, e-h pair undergoes low-energy intraband transitions. The second process is known as multi-phonon decay (MPD) in which the exciton energy dissipates via a chain of phonon scatterings. The MPD process, however, is negligible for the mobile excitons compared to the PAIEI and more pronounced for the localized excitons [76].

In the GNRs, a theory to explain the non-radiative relaxation processes is lacking. Prezzi *et al.* pointed out that the presence of the low-energy dark excitons significantly influences the PL emission of the GNRs for the family of $N = 3p + 1$ [52]. These dark excitons arise from the mixing of dipole-forbidden transitions in the same energy band. In this family ($N = 3p + 1$), the dark excitons are energetically very close to bright excitonic states and hinder the PL emission. This is supported by independent calculations for a member of this family, 10–AGNRs (D_1 and D_2 show the energy position of dark excitons in Fig. 2.2b) [49]. The results show that the presence of low-energy dark excitons in GNRs is strongly family dependent, in contrast to SWCNTs in which this is a common feature [52]. This is consistent with the results presented in chapter 3 about the PL emission from 7–AGNRs (in the family of $N = 3p + 1$) in which the emission is very weak for pristine GNRs [1]. Further extinction spectroscopy of 7–AGNRs revealed the existence of a low-energy feature with the spectral position of 1.77 eV in the extinction spectra [2]. We attributed this peak to originate from a quenching state(s), which contribute to hindering the PL emission in 7–AGNRs. This is discussed further in chapter 4.

On the other hand, in finite-length AGNRs, theoretical calculations predict localized Tamm states in addition to the delocalized bulk states [71, 73]. In this context, the bulk states are characteristic for infinite AGNRs, and Tamm states refer to localized states at termini of AGNRs, as schematically illustrated in Fig. 2.4a for a 7-AGNRs with 2 nm length and 0.7 nm width. Cardoso *et al.* calculated the band structure and absorption spectrum for finite 7-AGNRs as shown in Fig. 2.4b [73]. Apart from transitions between bulk states (shown as $E_{AA,n}$ in Fig. 2.4b), the presence of localized states results in low-energy transitions between Tamm states (E_{ZZ}) and from Tamm (bulk) to bulk (Tamm) states with the energy of $E_{\mathrm{AZ,n}}$. These transitions without excitonic effects are shown in absorption spectra (Fig. 2.4b) in gray, where the lowest transition energy is $E_{\mathrm{ZZ}} = 2.37$ eV. Considering that the excitonic effects (black curve) significantly red-shifts the transition energies (A, B, and B' peaks), reflecting the high exciton binding energies in GNRs. Dramatically, there is a dark state below peak A (absent in absorption spectrum) at the energy of 0.64 eV, which is assigned to be another origin of non-radiative recombination route in the finite (and even long) GNRs.

2.2.3 Scattering of light

The process of light scattering involves interaction of an incident photon with the frequency of ω_{in} with a system (e.g., a molecule) in an initial energy level E_i followed by scattering of a photon with the frequency of ω_{sc} and leaving the system in final energy level E_f [78]

$$\hbar\omega_{\mathrm{in}} + S(E_i) \longrightarrow \hbar\omega_{\mathrm{sc}} + S^*(E_f)\,. \tag{2.14}$$

The scattering might involve transitions between vibrational, rotational, or electronic states. This interaction can be described in classical view by means of a dipole moment $\mathbf{p}$ representing the scattering object. In the presence of incident light with electrical field $\boldsymbol{E} = \boldsymbol{E}_0 \cos(\omega_{\mathrm{in}} t)$,

$$\mathbf{p} = \boldsymbol{\mu} + \mathcal{P}\boldsymbol{E}\,, \tag{2.15}$$

where $\boldsymbol{\mu}$ is the possible permanent dipole moment (explained in Sec. 2.2). The second term in Eq. 2.15 represents the light-induced dipole moment, and $\mathcal{P}$ is the polarizability tensor ($\mathcal{P}_{ij}$), which is determined by the molecular structure. The polarizability and thus dipole moment depend on the coordinates of nuclei and electrons. For the sake of simplicity, we consider the case with no permanent dipole moment $\boldsymbol{\mu} = 0$. If the incident frequency is far from the resonance of vibrational transitions, then the induced displacement of nuclei upon illumination is small. Therefore, the polarizability can be expanded in a Taylor series in normal coordinates of the nuclear displacements q_n around the equilibrium positions

$$\mathcal{P}_{ij} = \mathcal{P}_{ij}(0) + \sum_{n=1}^{Q} \left(\frac{\partial \mathcal{P}_{ij}}{\partial q_n}\right)_0 q_n + \cdots\,, \tag{2.16}$$

where $\mathcal{P}_{ij}(0)$ is polarizability in the equilibrium coordinates in which $q_n = 0$. For a molecule with N_{nuc} nuclei, $Q = 3N_{\text{nuc}} - 6$ is the number of normal modes. If the vibrational magnitude is small, then the displacement for nth mode with frequency of $\omega_{\text{vib},n}$ can be expressed as

$$q_n(t) = A_n \cos(\omega_{\text{vib},n} t) \,, \tag{2.17}$$

where A_n is the amplitude of displacement. Substituting Eqs. 2.16 and 2.17 into 2.15 gives

$$\mathbf{p} = \mathcal{P}_{ij}(0)\boldsymbol{E}_0 \cos(\omega_{\text{in}} t) + \frac{1}{2}\boldsymbol{E}_0 \sum_{n=1}^{Q} \left(\frac{\partial \mathcal{P}_{ij}}{\partial q_n}\right)_0 A_n \left[\cos\{(\omega_{\text{in}} + \omega_{\text{vib},n})t\} + \cos\{(\omega_{\text{in}} - \omega_{\text{vib},n})t\}\right] \,. \tag{2.18}$$

Equation 2.18 represents an oscillating dipole moment, which radiates. In this equation, the first term corresponds to an elastic scattering process with the same frequency as the incident light ω_{in}. This is known as Rayleigh scattering. The second term describes inelastic scatterings consisting of frequency components with the frequencies $\omega_{\text{in}} + \omega_{\text{vib},n}$ and $\omega_{\text{in}} - \omega_{\text{vib},n}$. These correspond to Stokes and Anti-Stokes Raman scattering, respectively. The vibrational modes have quantized energy states, and thus the Raman scattered photons have specific energy shifts. Raman scattering is the topic of the next section and it is further explained.

2.2.4 Raman scattering processes

Raman spectroscopy is a powerful experimental technique that is extensively used to characterize the properties of the materials. Unlike photoluminescence, Raman is a coherent process (e.g., in molecules), i.e. the scattered photon is correlated with the incoming photon [79]. In this process, the scattered photons provide information about the intrinsic properties of the material. These consist of insights about vibrational and electrical properties, phase transitions, elastic properties under strain, and external pressure and temperature variations.

Raman scattering can be understood as presented in Fig. 2.5a. The process consists of a transition from an initial (ground) vibrational state i to a final vibrational state f via an intermediate excited state. This excited state does not need necessary to be a real but can instead be viewed as a virtual state v. This is in contrast with PL processes in which the transitions only occur between real states. If the virtual state energetically coincides with a real state e, the corresponding Raman scattering is known as resonant Raman scattering.

As pointed out in the previous section, the difference in the energy of scattered and absorbed photons is equal to the energy of difference between vibrational levels in molecules. In the view of solid state, these vibrational states are explained by phonons which arising from collective vibrations of the atoms in the lattice structure. Form now on, we use phonon to describe the Raman scattering. The Raman scattering, consisting of creation or annihilation of one phonon is known as single phonon-assisted Raman. Raman scattering can also take place with two phonons, including two annihilation, two emission, or one annihilation and one emission processes. The momentum and energy must be conserved in Raman scattering. Considering the single phonon scattering, this requires

$$\hbar\omega_{\text{in}} - \hbar\omega_{\text{sc}} = \pm\hbar\omega_{\text{ph}} \,, \quad \mathbf{k}_{\text{in}} - \mathbf{k}_{\text{sc}} = \pm\mathbf{q} \,, \tag{2.19}$$

here $\hbar\omega_{\text{ph}}$ is the energy, and $\mathbf{q}$ is the wavevector of the phonon taking part in the scattering process. The plus sign corresponds to creation of a phonon, and thus the energy of the scattered photon is

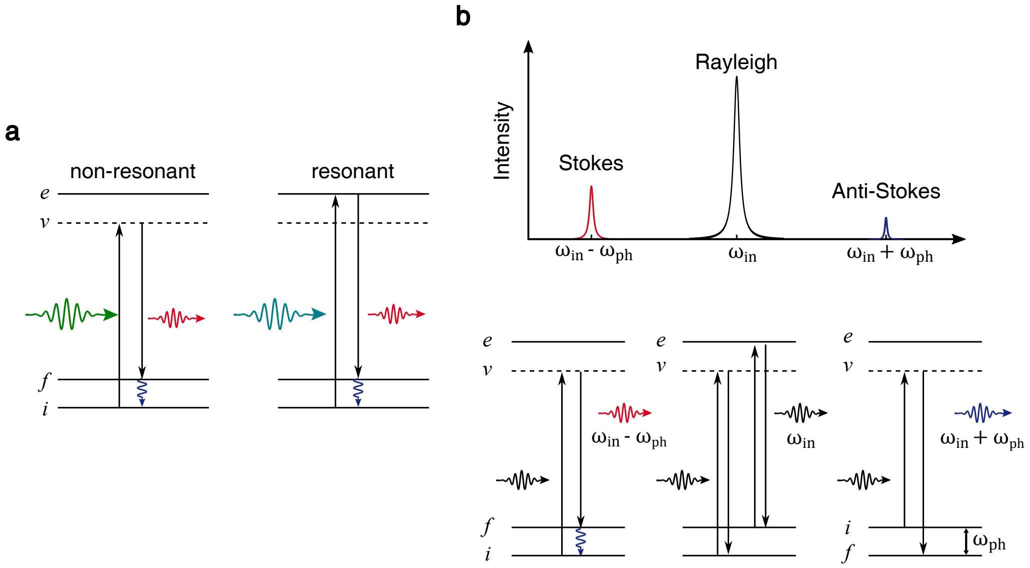

Figure 2.5: **a** The energy diagram represents Raman scattering processes from an initial state i to a final state f. The transition is via an excited state. This excited state can be virtual (v) or an eigenstate (e) of the system. When the incident photon energy matches the excitation energy to e, the corresponding Raman scattering is resonant. **b** Scattering of the incident light with the frequency ω_{in} results in Raman scattering with lower (Stokes) and higher (Anti-Stokes) frequency components, $\omega_{\text{in}} - \omega_{\text{ph}}$ and $\omega_{\text{in}} + \omega_{\text{ph}}$, respectively. The difference between energies of the scattered and incident photons is quantized and equal to phonon energy $\hbar\omega_{\text{ph}}$ (in a semiconductor). Rayleigh scattering is the elastic component with the same frequency ω_{in} as that of the incident light.

lowered. The minus sign refers to annihilation of a phonon. In the scattering spectrum, there appear a blue-shifted (anti-Stokes) and a red-shifted (Stokes) sidebands. Schematic view of these processes is illustrated in Fig. 2.5b. Although the classical approach explains both scattering peaks with the correct frequency shifts, it fails to predict the difference in the peak intensities. For this the quantum nature of the vibrational excitations (phonons) has to be considered. In fact, the population of phonons with state n_{ph} determines the probability of Stokes and Anti-Stokes scatterings. The population of phonons with the energy of $\hbar\omega_{\text{ph}}$ in thermal equilibrium follows the Bose-Einstein distribution [80, 81]

$$n_{\text{ph}} = \frac{1}{\exp\left(\hbar\omega_{\text{ph}}/k_{\text{B}}T\right) - 1} . \tag{2.20}$$

Creation of a scattered photon in Stokes Raman scattering is in accordance with one increase in the population of phonons $n_{\text{ph}} \rightarrow n_{\text{ph}} + 1$. In Anti-Stokes Raman scattering, it corresponds to one reduction in phonon population $n_{\text{ph}} + 1 \rightarrow n_{\text{ph}}$. This means that for anti-Stokes Raman scattering, the system is initially in a thermal excitation. Thus, at low temperatures, the probability of this scattering is low. Comparison of Stokes and anti-Stokes intensities is a means to probe the temperature of the sample. The ratio of the intensities for Stokes and anti-Stokes Raman scattering fulfills the following equation

$$\frac{I_{\text{Stokes}}}{I_{\text{anti-Stokes}}} \propto \frac{n_{\text{ph}} + 1}{n_{\text{ph}}} = \exp\left(\frac{\hbar\omega_{\text{ph}}}{k_{\text{B}}T}\right) . \tag{2.21}$$

This ratio is very large at room temperature, hinting that the Stokes Raman scattering is more convenient to implement the Raman scattering process. Finally, it is common to present the spectra as a function of Raman shift in the units of cm^{-1}. The Raman shift ν_R is

$$\nu_\mathrm{R} = \frac{1}{\lambda_\mathrm{in}} - \frac{1}{\lambda_\mathrm{sc}} . \tag{2.22}$$

The Raman shift is related to the phonon energy as $E_\mathrm{ph} = hc\nu_\mathrm{R}$. In Eq. 2.22 λ_in and λ_sc are the wavelengths of incident light and measured Raman scattered light, respectively.

2.2.5 Raman scattering in graphene and GNRs

Raman spectroscopy is the most commonly used technique to probe the properties of graphene, CNTs, and GNRs. In graphene, Raman scattering, e.g., is used to determine the number of layers as well as the density of imperfections and defects [80, 82–86]. The most important Raman mode in graphene is a single phonon mode known as G band lying around 1588 cm^{-1}. This mode is also present in CNTs and GNRs [1, 2, 85, 87]. Figure 2.6a shows a typical Raman spectrum for a single layer of graphene, displaying several scattering modes. Most prominent of these are the 2D mode – an overtone of G peak – at 2684 cm^{-1} and G+2D at 4268 cm^{-1}. The Raman spectrum of a single layer of 7–AGNRs on quartz substrate is presented in Fig. 2.6b. Compared to the spectrum for graphene (Fig. 2.6a), the band labeled D appears near the G band. Furthermore, there is a low frequency peak called radial breathing like mode (RBLM) at 396 cm^{-1}, which is a characteristic mode for 7–AGNRs. In the following the important Raman modes in the GNRs are discussed.

G band

The G band appears in Raman spectrum as a result of a transition involving a single optical phonon. This, in fact, originates from the in-plane vibration of carbon atoms. The movement of the neighboring atoms is in the opposite direction. Additionally, the carbon atoms can have out of plane vibrations. Such vibrations do not contribute to the Raman scattering and are known as inactive Raman vibrations [86].

The lattice vibrations leading to the G band in 7–AGNRs are schematically illustrated in Fig. 2.6d. The G mode in 7–AGNRs appears at 1608 cm^{-1} and similar to SWCNTs shows a small shift and broadening with respect to graphene [89]. The spectral position and broadening of the G peak are important parameters in order to gain information about the induced external effects. For example, changing the level of charge carriers, e.g., by applying an electric field, can shift or broaden the G peak [90, 91].

Additionally, the ratio between the intensity of the G and 2D bands is commonly employed to determine the number of graphene layers (e.g., for a single layer $I_\mathrm{G}/I_\mathrm{2D} \approx 1/2$) [82–85, 92]. The G band does not show dispersion relation as a function of excitation photon energy (unlike the D band) [1, 85, 93], and its intensity is significantly higher compared to the RBLM in GNRs. Its intensity can be used to probe the electronic energy levels of the material. When the excitation photon energy matches the transition from the ground state to an excited state and the Raman scattering process becomes resonant, the intensity of the G band is significantly enhanced. We measured the excitation photon energy dependence of the G mode to resolve the excitonic features in 7–AGNRs (see Chapter 3).

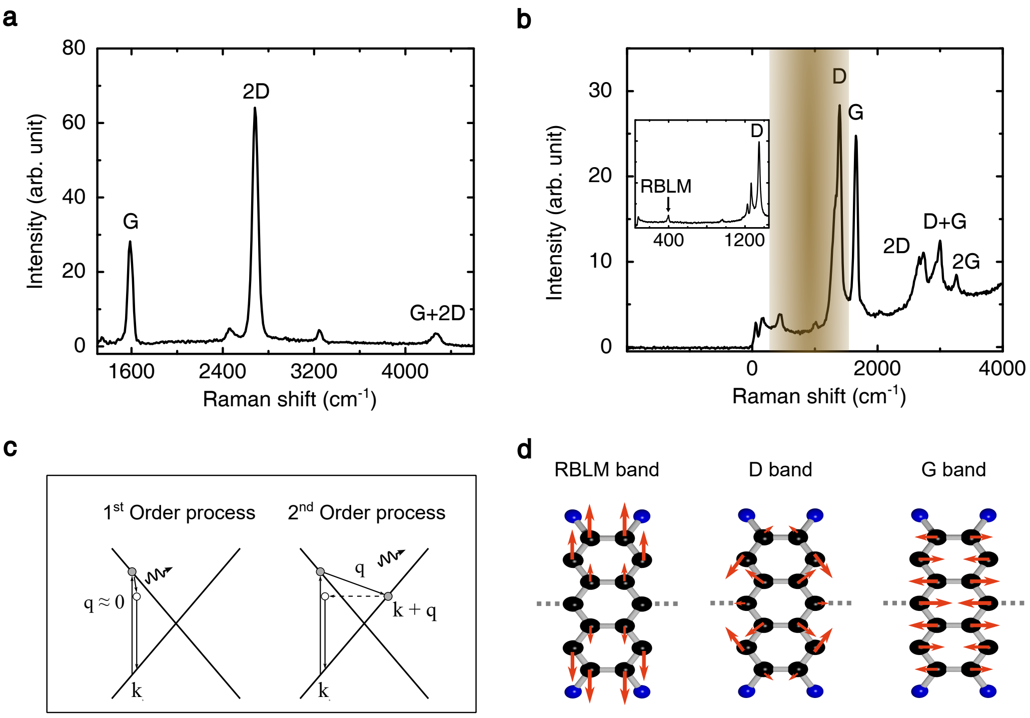

Figure 2.6: **a** The Raman spectrum for a single layer of graphene on SiO_2/Si substrate with the most common Raman modes. **b** Raman spectrum of 7–AGNRs. Unlike graphene, the D band has high intensity compared to the G mode. The characteristic Raman mode (RBLM) of the GNRs is visible at 396 cm^{-1}. This peak is displayed in the inset with higher resolution. **c** Schematic view of the Raman scattering in graphene for 1^{st} and 2^{nd} order processes. In 2^{nd} order process (e.g., the D mode) the momentum is preserved by inter-valley scattering from a defect point in the lattice. **d** Planar vibrations of carbon atoms (black) corresponding to the RBLM, D, and G modes in 7–AGNRs. Carbon atoms are passivated by hydrogen atoms (blue) at the edges (Inspired by [88]).

D band

The presence of defects and disorder in graphene is reflected in the Raman spectrum by a peak at around 1350 cm^{-1} known as the D band. The origin of this band is a defect-mediated second order Raman scattering process. This was realized due to the dispersion of the D band as a function of excitation photon energy (50 cm^{-1} per 1 eV), which was puzzling scientists for over 20 years [93].

For graphene and in general semiconductors, the Raman scattering processes are explained in a microscopic theory involving three steps. In the first step, the incident photon promotes the graphene into an intermediate state by virtually creating an e-h pair. The second step consists of scattering of the e-h pair to a new state by emitting a phonon. Eventually, the e-h pair radiatively recombines by emitting the scattered photon. The process is illustrated for the first (left) and second order (right) Raman scatterings in Fig. 2.6c. In first order Raman scattering, the conservation of momentum only allows contributions from phonons with $\mathbf{q} \approx 0$. This condition may relax in the presence of defects, thus allowing phonons with larger $\mathbf{q}$ to be involved in Raman scattering in a second order scattering process. The second order process leading to the D band consists of inelastic scattering of the electron by emitting a phonon with $q \neq 0$. This results in inter-valley transition of the electron within the Dirac cone. The electron is then scattered back from a defect point. This scattering is elastic and provides conservation of the momentum [93].

Any type of deformation, vacancy, or sp^3 defect [84] as well as deformation caused by strain, bending, or twisting, which modify the crystalline structure of graphene contribute to the D band scattering. The D band can additionally raise from edges of graphene [94, 95]. The D band in GNRs and SWCNTs has high intensity compared to the graphene even in the absence of defects. Figure 2.6d visualizes the motion of carbon atoms in the lattice of 7–AGNRs for the D band. This band is located at approximately 1344 cm^{-1}. The origin of the D band in GNRs is still under debate and is attributed to both first and second order processes [87, 88]. Verzhbitskiy *et al.* attributed the D band in GNRs originating from a defect-free first order Raman scattering [89]. Therefore, the D band is expected to exhibit no dispersion similar to the G band [87]. Surprisingly, they observed noticeable Raman shift (35 cm^{-1} per eV) for the laser excitation with photon energy larger than 1.8 eV. The dispersive character was then ascribed to the disorder-related scattering arising from the edge functionalizations and defects [87].

RBLM band

The radial breathing like mode is an intrinsic Raman mode of GNRs, which is analogous to the radial breathing mode (RBM) in SWCNTs and which is absent in graphene [80]. The RBLM in GNRs, like the RBM in SWCNTs, appears at low Raman shift [89, 96, 97]. This is the reason why they have similar names, although it has a different origin in GNRs. The RBLM is a result of relative movements of the carbon atoms in width direction of the GNRs. It is schematically illustrated in Fig. 2.6d, where the upper (lower) atoms move upwards (downwards) such that motion is largest for the atoms at the edges. For the RBLM band, the GNRs can thus be viewed as a 1D oscillator and this directly implies a relation between the RBLM shift (ν_{RBLM}) and the width (w) of GNRs. This relation is written as [96]

$$\nu_{\mathrm{RBLM}} = \mathrm{a}\frac{1}{\sqrt{w}} + \mathrm{b}\,. \tag{2.23}$$

Here a and b are the fitting parameters. From the DFT calculations, a = 1632.5cm^{-1} and b = −202.5cm^{-1} [98]. Noticeably, there are several tens of cm^{-1} difference in the reported values of a and b [19, 96]. This relation is a fruitful tool to examine the width of GNRs [89, 97]. Besides the RBLM mode, further distinctive Raman modes have been anticipated in the GNRs. For example, a Raman mode is activated in the GNRs as a result of vibration of atoms at the edge of GNRs and known as localized mode. In the GNRs with armchair edges, this appears at 2000 cm^{-1}, which shifts to 3000 cm^{-1} for hydrogen-terminated AGNRs [96]. Such mode does not exist in CNTs. Nevertheless, it cannot be resolved in Fig. 2.6b, since it energetically coincides with the higher order Raman peaks. Thus, the RBLM is the most prominent characteristic Raman mode for GNRs, which is commonly used to determine the width of GNRs.

2.3 2D material-based Electronics and optoelectronics devices

One particular aspect leading to improvement in performance of electronic and optoelectronic devices is miniaturization, which results in higher speed and lower energy consumption. Miniaturization, however, is limited by fundamental restrictions. For example, operation of conventional transistor is

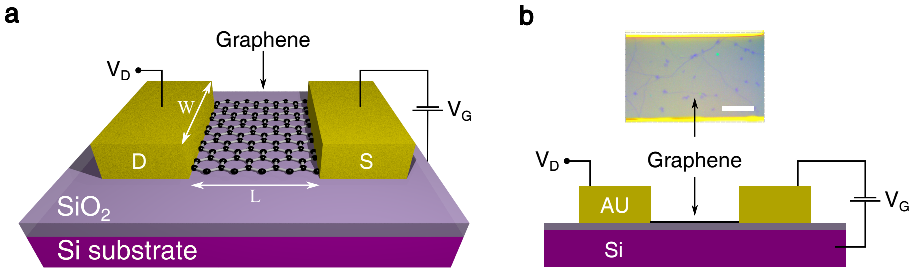

Figure 2.7: **a** Illustration of a typical back-gated graphene based field-effect transistor (G-FET). The V_{D} drives a current I_{D} between drain-source (D-S). Imposing an electric field between S and gate (G) modifies the charge carrier densities and consequently changes the I_{D}. **b** Top: Top view of a device consisting of a single layer of graphene between drain and source electrodes with a separation of 50 μm. Scale bar is 20μm. Bottom: schematic side view of the same device.

significantly influenced in low dimension by current leakage, low mobility and short channel effects [8, 99]. These limitations together with exploration of novel materials have triggered the research progresses in device production, leading to fabrication of devices with novel structures and different working principles.

The recently discovered low-dimensional materials are a particularly interesting group of novel materials by offering atomic thickness, transparency, and flexibility. So far, a variety of 1D and 2D materials such as graphene, SWCNTs, and TMDs have been used to fabricate field-effect transistors (FETs) [8, 99, 100]. In a FET, the transport of carriers is switched on or off by applying an electric field across the active material. Such transistors have been developed using 2D materials in the form of lateral and vertical heterostructures. Memories and negative differential resistance (NDR) devices [101] are other components fabricated using 2D materials [8, 102]. In the field of optoelectronics, electroluminescent emitters [8], blackbody radiators [103–107], and optical detectors [8, 108, 109] are some examples of demonstrated devices in which 2D materials have been used as active medium.

So far, on-surface grown GNRs have been used to fabricate FETs. The first FET demonstrated using GNRs is the work by Bennet *et al.* [110]. Later on, several groups have fabricated and developed the FETs using different types of GNRs and with various dimensions [47, 111–114]. Thus far, no optoelectronic devices based on GNRs have been reported. The first GNR-based photodetector (PD) is demonstrated in this work and discussed in chapter 5. At the moment the greatest interest in the application of GNRs is in FETs and photodetectors. Therefore in the following section a review of the basic principles of FETs and optical detectors based on 2D materials is provided.

2.3.1 Field-effect transistors

Electric-field switchable transistors or FETs are a modern generation of transistors with low-energy consumption. The structure of the FETs can be realized as a simple lateral back-gated FET shown in Fig. 2.7. The current transport between the drain (D) and source (S) electrodes is controlled by applying a voltage to the gate (G) electrode that results in an electric field across the active material to manipulate the conductivity in the D-S channel. The active material is a semiconductor. In Fig. 2.7b the micrograph shows a top view of a typical graphene device, consisting of a single layer graphene on top of which 50 nm thick metal electrodes (10 nm Ti and 40 nm Au) with 50 μm separation are fabricated. The substrate is highly p-doped silicon with a 300 nm thermal oxide layer on top (SiO_2/Si).

In such devices the gate voltage modifies the concentration of carriers in graphene and consequently changes the conductivity. There are several parameters to characterize and evaluate the performance of the FETs [8, 115]. The main parameters are listed below.

- On/off current ratio ($I_{\mathrm{on}}/I_{\mathrm{off}}$): The ratio which defines how drain current (I_{D}) can be modulated as a function of the gate voltage (V_{G}). I_{on} and I_{off} are the drain currents in the operational on and off modes, respectively. Ideally $I_{\mathrm{off}} \approx 0$.
- Subthreshold slope ($\mathcal{SS}$): A quantity which determines how fast is the transition between the off and on states in a FET. It is defined as the change in I_{D} as a function of V_{G} and expressed as
$$\mathcal{SS} = \left(\frac{\mathrm{d}\,(\log I_{\mathrm{D}})}{\mathrm{d}V_{\mathrm{G}}}\right)^{-1} . \tag{2.24}$$
It is a measure of the required V_{G} in order to increase the I_{D} by one order of magnitude.
- Channel conductance (g_{ch}): The conductivity of the active material. A quantity, which determines the relation of I_{D} and V_{D} for constant V_{G}. This is related to the sheet resistance R_{sheet}.
$$g_{\mathrm{ch}} = \left.\frac{\partial I_{\mathrm{D}}}{\partial V_{\mathrm{D}}}\right|_{V_{\mathrm{G}}} , \qquad \frac{1}{R_{\mathrm{sheet}}} = g_{\mathrm{ch}} \frac{\mathrm{L}}{\mathrm{W}} . \tag{2.25}$$
Here L and W are length and width of the conductive (D-S) channel, respectively (see Fig. 2.7a).
- Transconductance (g_{tr}): The parameter that characterizes the change in the drain current as a function of the gate voltage for a constant drain voltage
$$g_{\mathrm{tr}} = \left.\frac{\partial I_{\mathrm{D}}}{\partial V_{\mathrm{G}}}\right|_{V_{\mathrm{D}}} . \tag{2.26}$$
- Threshold voltage (V_{TH}): The gate voltage at which the channel conductance starts to increase.
- Turn-on gate voltage ($V_{\mathrm{G,on}}$): The gate voltage at which I_{D} is increased to the current in the operating mode (I_{on}).
- Contact resistances (R_{c}): The electrical connections between the D/S electrodes and the active material involve resistivity that is known as contact resistance. Depending on the materials the contact can be Ohmic or Schottky type. The R_{c} is the limiting factor for the charge injection in particular for the 2D materials.
- Charge carrier mobility (μ_{mob}): An intrinsic parameter of a material which describes how fast a charge carrier is transported for a specific distance under an electric field.

When a material is used in a FET, the charge transport mechanism is modified and the intrinsic carrier mobility (μ_{mob}) does not match to the mobility measured in the device. Thus an effective charge mobility (μ_{eff}) is defined in which the effect of the contact resistance is also included. Often μ_{eff} is known as the field-effect mobility [47, 111]. The mobility is a critical parameter since characteristics of FETs like $\mathcal{SS}$, g_{ch}, and g_{tr} are directly proportional to μ_{eff}. Additionally, the on/off current ratio is of paramount importance and both $I_{\mathrm{on}}/I_{\mathrm{off}}$ and μ_{eff} are commonly used to quantify the performance of FETs.

N–AGNRs	Type	μ_{eff} [cm^2 V^{-1}s^{-1}]	$I_{\text{on}}/I_{\text{off}}$	Reference
$N = 5$	network	2×10^{-2}	5	[47]
$N = 7$	single	3.6×10^{-3}	37	[110]
$N = 7$	single layer	1.22×10^{-3}	87.5	[111]
$N = 9$	network	$\approx 1 \times 10^{-3}$	120	[47]
$N = 9$	single	–	$\approx 10^5$	[113]
$N = 13$	single	–	100	[113]

Table 2.2: List of mobilities and $I_{\text{on}}/I_{\text{off}}$ for the developed FETs using on-surface grown GNRs.

FET based on 2D materials

Charge transport in the 2D materials takes place in the plane of the materials. The transport is limited by scattering processes: electron-phonon scattering including acoustic and optical phonons, electron-electron scattering, and defects or impurity scattering are the main limiting factors of carrier mobility. Among the 2D materials, graphene has high μ_{eff}. A value of 1.8×10^4cm^2 V^{-1}s^{-1} has been reported for the back-gated FETs consisting of single layer of graphene on SiO$_2$/Si substrate [102]. A higher value of 1.4×10^5cm^2 V^{-1}s^{-1} was achieved for the FETs with hBN-encapsulated graphene (hBN/graphene/hBN) [116]. Reduction of the contact resistance and suppression of the carrier scattering are attributed as the reasons for the high mobilities in these devices.

Although the mobilities for the graphene-based FETs are very high, the on/off current ratio, however, is low, being in the range of 50 [116]. This is due to lack of the bandgap in graphene. This hinders the functionality of these FETs, in particular for applications in logic circuits. For this reason, other semiconducting 2D materials like TMDs have been employed as alternatives. Demonstration of the FETs using MoS$_2$ with $I_{\text{on}}/I_{\text{off}} = 10^8$ was reported [117, 118]. In addition, the FETs based on WSe$_2$, ReS$_2$ have been demonstrated with $I_{\text{on}}/I_{\text{off}}$ of 10^8 [119] and 10^7 [120], respectively. Nevertheless, the FETs fabricated using TMDs have lower mobilities than graphene. In MoS$_2$ FETs, μ_{eff} up to 700 cm^2 V^{-1}s^{-1} has been reported. For other similar materials, e.g., WSe$_2$ and ReS$_2$, μ_{eff} does not exceed 300 cm^2 V^{-1}s^{-1}. In such FETs, the presence of Schottky barriers at the metal-2D material interface has been found as the main limiting factor of μ_{eff} [116].

As a class of low-dimensional materials, GNRs appear as an attractive material to develop the low-dimensional FETs. Opening up a bandgap facilitates reaching higher $I_{\text{on}}/I_{\text{off}}$ values with respect to graphene while potentially having high mobility [121]. Earliest GNR FETs were based on single 7-AGNRs on SiO$_2$/Si with $\mu_{\text{eff}} \approx 3.6 \times 10^{-3}$cm^2 V^{-1}s^{-1} and $I_{\text{on}}/I_{\text{off}} = 37$ [110]. Later, the FETs have been demonstrated using 5– [47], 7– [111, 112], 9– and 13–AGNRs [113]. The list of mobilities and $I_{\text{on}}/I_{\text{off}}$ values for these FETs are shown in table 2.2. As can be seen from the table, the goal of the high mobility and $I_{\text{on}}/I_{\text{off}}$ ratio has not been reached experimentally yet.

The so far fabricated GNR FETs can be classified into two groups: FETs based on single GNRs and network films. Since the length of on-surface grown GNRs is limited to a few tens of nanometer, device fabrication is challenging. Llinas *et al.* demonstrated single-GNRs FETs using both 9-AGNRs and 13-AGNRs with the back- and top-gated configurations [113]. They achieved high performance FETs with the promising $I_{\text{on}}/I_{\text{off}} = 10^5$ and $I_{\text{on}} > 1\mu$A (for $V_D = -1$V) using 9–AGNRs. The higher performance obtained for 9-AGNRs than 13-AGNRs is attributed to the smaller bandgap (2.10 eV for $N = 9$ and 2.35 eV for $N = 13$). In fact, semiconducting AGNRs with smaller bandgap are better suited for FETs [121]. For instance, the GNRs with $N = 5$ have a bandgap of 1.7 eV, and an estimated intrinsic mobility (μ_{mob}) of 25−2500 cm^2 V^{-1}s^{-1} [122]. Thus, 5–AGNRs can be ideal GNRs for the single GNR FETs. Since the length of 5–AGNRs is in the range of 10 nm, they have not been used for demonstration of single ribbons FETs to date [113]. Thus far, a network of 5–AGNRs have been used to fabricate FETs [47].

For the FETs, utilizing the networks of GNRs has some advantages in comparison to using the individual ribbons: it is significantly less technically challenging to fabricate, the yield noticeably increases (from $< 10\%$ to $\approx 100\%$), and the short channel effects do not influence the performance of the device [47, 113]. Recently, Richter *et al.* have fabricated FETs in which the networks of 5–AGNRs and 9–AGNRs are the conductive channel [47]. Using GNR networks allows fabricating structures with larger dimensions. In the network based FETs with the drain-source gaps of 5 μm, the short channel effects are completely eliminated. In such devices the values of $I_{\mathrm{on}}/I_{\mathrm{off}} \approx 5$ for 5–AGNRs and $I_{\mathrm{on}}/I_{\mathrm{off}} \approx 120$ for 9–AGNRs were achieved. The low ratio for 5–AGNR devices is attributed to the high charge carriers density as a result of extrinsic dopants. The obtained field-effect mobilities are $\mu_{\mathrm{eff}} \approx 2 \times 10^{-2}$cm^2 V^{-1}s^{-1} and $\mu_{\mathrm{eff}} \approx 1 \times 10^{-3}$cm^2 V^{-1}s^{-1} for $N = 5$ and $N = 9$, respectively. It is evident that the mobilities are noticeably low. The reason is not due to the metal-GNRs carrier injections, since the devices show formation of the low-resistance ohmic contact. The limiting factor for the transport in the GNRs network is the hopping at the interface of GNR-GNR. Since the channel length is much larger than the length of the individual GNRs, the electrical transport is through the carrier hopping between GNRs. The hopping range has been determined to be on the scale of GNR length (≈ 20 nm).

The electrical transport in the single layer of GNRs is similar to that in the network films and dominated by the hopping mechanism. Recently, GNR FETs using the single layer of 7–AGNRs have been demonstrated for the devices with gaps from few tens of nanometers up to 1 μm where hopping dominates the electrical transport [111]. This is analogous to the transport in SWCNT films and conductive polymers in which the electrical transport has been extensively investigated [123, 124]. Since the hopping is the main limitation to demonstrating high performance GNR FETs, it is essential to grow longer GNRs to improve their performance in FETs as well as other electronic and optoelectronic devices.

2.3.2 Photodetection using 2D materials

Photodetectors (PDs) are the platform to convert photons into free carriers and in this way the electromagnetic energy into the electrical signals. These devices are the key elements for many applications and there is an ongoing effort to improve their performance. There exists many parameters to evaluate the performance of PDs. For instance, temporal response, sensitivity, and spectral detection range, as well as flexibility, integration compatibility, and transparency [8, 108]. For practical purposes scalability and production costs are additionally important. Some of the key quantitative parameters for PDs are listed below.

- Detector responsivity (R_{ph}): A factor, which quantifies how sensitive the PD is and is defined as the ratio of photogenerated current I_{ph} or photoinduced voltage V_{ph} to the incident power P_{in}, i.e. $R_{\mathrm{ph}} = I_{\mathrm{ph}}/P_{\mathrm{in}}$ or $R_{\mathrm{ph}} = V_{\mathrm{ph}}/P_{\mathrm{in}}$.

- External and internal quantum efficiency: The external quantum efficiency (EQE) is defined as the ratio of the number of photogenerated e-h pairs per second, producing the photocurrent I_{ph}, to the number of incident photons with a given energy (E_{ph}) per second:

$$\mathrm{EQE} = \frac{I_{\mathrm{ph}} E_{\mathrm{ph}}}{e P_{\mathrm{in}}} . \tag{2.27}$$

Here e is the electron charge. In a similar manner, the internal quantum efficiency (IQE) is defined as:

$$\mathrm{IQE} = \frac{\mathrm{EQE}}{A_{\mathrm{abs}}} = \frac{I_{\mathrm{ph}} E_{\mathrm{ph}}}{e P_{\mathrm{in}} A_{\mathrm{abs}}} , \tag{2.28}$$

in which A_{abs} is the fraction of the absorbed intensity.

- Noise equivalent power (NEP): This quantifies the amount of the optical power for which the signal-to-noise ratio equals unity for half a second integration time. The NEP unit is $\mathrm{W}/\sqrt{\mathrm{Hz}}$. The smaller NEP indicates the more sensitive PD. The minimum detectable optical power P_{min} is given as

  $$P_{\mathrm{min}} = \mathrm{NEP} \times \sqrt{\mathrm{BW}} , \tag{2.29}$$

  where BW is the measurement bandwidth. We note that NEP is a wavelength-dependent parameter.

- Transit (τ_{tr}) and recombination (τ_{R}) times: The former is the time required to carry the photogenerated carriers from, e.g., the illumination spot in the active material to the electrodes and is inversely proportional to the mobility. The τ_{R} is the lifetime of photogenerated carriers. For example, in graphene $\tau_{\mathrm{R}} \approx 1$ps [125, 126]. In presence of the defects and impurities, τ_{R} can be replaced by an effective carrier lifetime τ_{eff} in which the trapping time is also included [127].

- Photoconductive gain (G_{ph}): An important parameter in the photoconductive PDs that corresponds to the number of collected photocarriers per number of the absorbed photons. It is related on the transit and the recombination times as [128]:

  $$G_{\mathrm{ph}} \propto \frac{\tau_{\mathrm{R}}}{\tau_{\mathrm{tr}}} (1 - e^{-\tau_{\mathrm{tr}}/\tau_{\mathrm{R}}}) . \tag{2.30}$$

2D materials have been found as interesting materials to demonstrate high performance photodetectors. Different types of PDs using 2D materials have been developed [8, 102, 129–134]. Among the 2D materials, graphene and other carbon-based materials have been the most used materials as the active medium in PDs [108]. Having high mobility and extremely broad absorption spectrum facilitates ultrafast detection for a variety of spectral ranges from ultraviolet to microwave. Xia *et al.* designed an ultrafast PD using a single layer of graphene with the responsivity of 0.5 mAW^{-1} at 1550 nm wavelength. They measured the PD bandwidth up to 40 GHz and predicted it to be > 500 GHz [135]. Alternatively, the semiconducting TMDs have been used to produce PDs. For example, single layer of MoS_2 with 10% absorbance is an attractive material for photodetection [136]. Previously, PDs consisting of single layer MoS_2 have been demonstrated with the high responsivity of 880 AW^{-1} [137]. These PDs, however, are not fast (with 9 s response time). Additionally, WS_2, WSe_2, ReSe_2, and heterostructures of these 2D materials have been used to fabricate PDs [102].

The origin of the detection in 2D-based PDs have been extensively investigated. It has been realized that there are several different mechanisms contributing to the detection of photons in such PDs. These mechanisms include photovoltaic (PV), photoconductive (PC), photo-thermoelectric (PTE), Bolometric, and photogating (PG) effects [108]. In the following, the basics of these mechanisms are introduced.

Photovoltaic and photoconductive effects

Pairs of e-h are created upon absorption of photons in the active medium. In the presence of an intrinsic electric field, e.g., at usually: pn-junction or in the regions with different doping levels, the photogenerated e-h pairs can be separated and consequently contribute into the detection process. This mechanism is known as PV effect. In graphene the charge separation often occurs due to the formation of a built-in potential usually at the interface of metal and graphene, where graphene under the metal has different doping than next to the metal. This phenomenon is also known as the band bending [125, 138–140]. A schematic view is illustrated in Fig. 2.8a.

Alternatively, the charge separation can be accomplished using an external electric field by applying a bias voltage, similar as in the typical conventional semiconductor-based PDs. Figure 2.8b illustrates the separation of e-h pair in a biased graphene PDs. Such detectors are also known as photoconductive (PC) PDs [141]. In the semiconducting PC PDs, the generated photocurrent is a result of increase in the conductivity $\Delta\sigma$ due to increase in the number of free carriers in the active material (see Fig. 2.8c). The produced photocurrent is proportional to the external bias voltage as [127, 142]

$$I_{\mathrm{ph}}^{\mathrm{PC}} = \frac{\mathrm{W}}{\mathrm{L}}\Delta\sigma V_{\mathrm{B}}\ . \tag{2.31}$$

Here W and L are the width and the length of the active medium under illumination, respectively. Among the 2D materials, graphene as a semimetal is not a good choice for PC PDs. Applying a small bias voltage results in a huge dark current. For example, a 1 V biased graphene PD produces a dark current $\approx 10^4$ times higher than photocurrent (at $V_{\mathrm{G}} = 0$), which severely influences the performance of the PD [143]. This issue does not exist for semiconducting 2D materials such as $\mathrm{MoS_2}$ where the presence of the bandgap suppresses the dark current. Applying an external bias facilitates the lateral band alignment and makes the photocarrier collection more efficient. Noticeably, the PV or PC effects in semiconducting 2D materials and even in graphene-based PDs are dominantly present [108]. The PC effect, in the first demonstrated GNR PDs, is recognized as the main detection mechanism. Further details are provided in chapter 5.

Photo-thermoelectric effect

Beside the PV (PC) effect in which conversion of photons to e-h pairs directly results in the detection process, absorption of the incident light can also lead to the local heating. If the heating is located at the interface of the two regions with different seebeck coefficients S_1 and S_2, it can generate a thermal voltage which is given by [108]

$$\Delta V_{\mathrm{PTE}} = (S_2 - S_1)\Delta T\ . \tag{2.32}$$

Here ΔT is the temperature difference produced upon absorption of the light. Similar to the schematic shown in Fig. 2.8d, the PTE effect can happen inside the active material, for example in the graphene

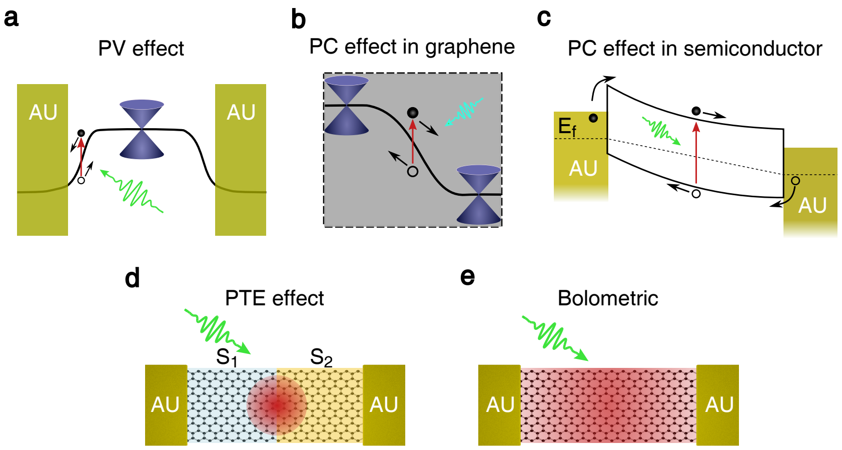

Figure 2.8: **a** Band profile of graphene is modified at metal-graphene interface as a result of different dopant levels (at zero bias voltage), and under external bias voltage in **b**. **c** In photoconductive PDs, photogenerated e-h upon absorption of light in a semiconducting 2D material can be collected when a bias voltage is applied. **d** PTE effect: generated heating upon light absorption at the interface of active material with different Seebeck coefficients (S_1 and S_2) can be detected. **e** In bolometers absorption of light heats up the active material leading to modification in the conductivity. The changes can be detected under application of a bias voltage.

with differently doped regions (e.g., n and p), or at the interface of metal and 2D material [144–146]. For the metals typical seeback coefficients are around 1 μV/K while for the semiconducting 2D materials the coefficients are in the range from few to thousands of μV/K [8]. The coefficient is strongly dependent on the conductivity of the material and is expressed by Mott Formula [126]

$$S = \frac{\pi^2 k_B^2 T}{3e} \frac{1}{\sigma} \frac{d\sigma}{dE} . \tag{2.33}$$

Here σ is the conductivity of the active material, k_B is the Boltzmann constant, $d\sigma/dE$ is the derivative of conductivity with respect to energy at the level of Fermi energy E_F. We note that this relation is valid only for low temperatures ($k_B T << E_F$). In the typical graphene-based PDs, a part from the PV effect, the PTE effect plays a noticeable role in the detection. In general, it is not trivial to separate the contribution of these effects from each other. Dependence on the gate voltage, polarization and wavelength of the incident beam can be used to resolve the contribution of each effect.

Bolometric effect

Absorption of the incident light and consequently generation of heat may directly change the conductivity of the active material. Sensing of this change is the mechanism of photodetection in bolometers [147]. Unlike the PTE effect, in the bolometric effect, the heating spot does not need necessary to be in a non-uniform region of the active material. Changes in the conductance can take place in the active materials with uniform properties (see Fig. 2.8e). In these PDs, the changes in the conductance upon absorption of the light originate from two effects [108]:

- The absorption of light produces heating and thus changes the carrier mobility of the active material.

- The number of charge carriers increases upon illumination and consequently changes the conductivity. One should note that this effect coincides with the PC effect in the biased PDs.

Operation of the bolometers requires an external bias voltage to track the changes in the current transport in the dark and under the illumination. A bolometric PD based on double-layer graphene has been reported by Yan *et al.* [148]. Similar detectors have been demonstrated using the network of SWCNTs in which upon illumination of the light, the resistance of the conductive channel increases and subsequently the current transport is decreased [149].

Photogating effects

The photogating effect is commonly investigated and used in phototransistors [150, 151]. Upon illumination, the threshold voltage V_{TH} in the dark shifts to $V_{\mathrm{TH}} - \Delta V_{\mathrm{TH}}$. As a consequence, the current transport changes from I_{D} to $I_{\mathrm{D}} + \Delta I_{\mathrm{D}}$. The difference of the current under the illumination and in the dark is equivalent to the photocurrent and is expressed as

$$I_{\mathrm{ph}}^{\mathrm{PG}} = I_{\mathrm{D}}\left(V_{\mathrm{G}} - V_{\mathrm{TH}} + \Delta V_{\mathrm{TH}}\right) - I_{\mathrm{D}}\left(V_{\mathrm{G}} - V_{\mathrm{TH}}\right) \rightarrow I_{\mathrm{ph}}^{\mathrm{PG}} \approx g_{\mathrm{tr}} \Delta V_{\mathrm{TH}} \,. \tag{2.34}$$

Here $g_{\mathrm{tr}} = \mathrm{d}I_{\mathrm{D}}/\mathrm{d}V_{\mathrm{G}}$ is the transconductance of the phototransistor (explained in section 2.3.1). So far, fabrication of the phototransistors using 2D materials has been reported [151–155]. Phototransistor based on thin film of $\mathrm{MoS_2}$ is an example in which both the PC and PG dominantly are present in the response of the PDs. The PC signal shows significantly high responsibility ($10^3\,\mathrm{AW}^{-1}$) but slow response time of $\approx$ 2s, while the PG contribution is noticeably lower (up to 4.1 AW^{-1}) with $\approx 33\mu$s response time. Thus, only the PG mechanism is satisfying for the fast detection [127].

CHAPTER 3

Defect-induced brightening of graphene nanoribbons

3.1 Introduction

On-surface grown graphene nanoribbons (GNRs) are synthesized on metallic substrates, e.g., Au (see section 2.1.1). The metallic substrate thus significantly modifies the properties of the GNRs, for example, due to screening effects (section 2.1.3), and consequently hinders the attempts to explore the optical properties of the GNRs on top of the growth substrates. This restriction is eliminated upon transferring of the GNRs to insulating substrates. This transfer technique is explained in the next section. In this chapter, the optical properties of a single layer of aligned 7–AGNRs, which is transferred from Au(788) to quartz, have been investigated. Photoluminescence (PL) and Raman spectroscopy are the main methods used for the optical characterization. We observe that pristine 7–AGNRs have weak PL emission. This is examined in the 1.9−3 eV ($\approx 400-650$ nm) range for the photon energy of the excitation light. The origin of low emission in the GNRs is attributed to non-radiative transitions arising from quenching or dark state(s) (see section 2.2.2).

We show that the PL emission can be enhanced by inducing defects into the lattice of 7–AGNRs. Induction of the defects in low-dimensional semiconductors is a hot topic in particular to obtain stable single-photon sources [156]. These defects significantly modify the dynamics of the excited carriers and exhibit exotic optical properties with respect to the parent material. For example, defect points in hBN have been realized as robust quantum emitters operating at room temperature [10, 11]. Pristine semiconducting SWCNTs do not fulfill the requirement for single photon emission (SPE), which requires a quasi-two level system. However, localization of excitons by means of trapping the mobile excitons with deep potential traps (typical depth $\geqslant 100$ meV), can provide the condition for room temperature SPE. This results in red-shifted emission (100−300 meV below E_{11}) from defect states, and enhances the quantum efficiency to 10−30%. This localization can be achieved by localized covalent functional defects, for example, by implanting aryl sp^3 functional groups, induced via ozonation or diazonium chemical reactions [10, 157]. Such benign defects analogously can be induced in the GNRs. Here, we demonstrate the formation of defects by means of a photo-induced reaction. In order to induce the defects, the pristine 7–AGNRs are exposed to laser light with the photon energy of 2.8 eV for several minutes under ambient conditions. Upon formation of the defects, the emission increases with a distinct feature in the PL spectrum at 1.8 eV. The enhanced emission upon formation of the defects has the same polarization anisotropy as the Raman spectra. This indicates that the structure of the GNRs after the laser exposure is preserved. The induced defects have sp^3 character. This is supported by the results obtained in the experiment in which by exposing hydrogen atoms to the GNRs in ultra-high vacuum conditions, the same modifications in PL emission were observed.

3.2 Making Graphene Nanoribbons Photoluminescent

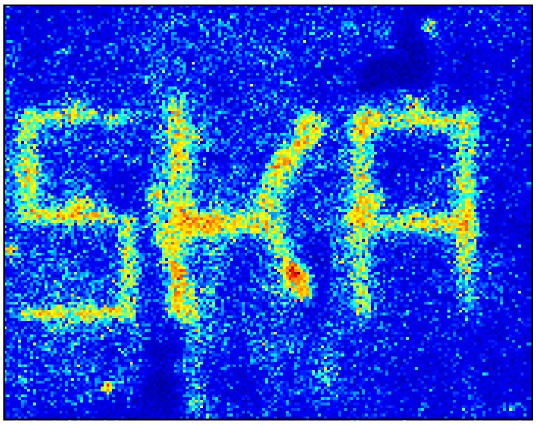

Integrated PL emission: GNRs are rendered bright in the form of "SKA" letters.

Note: The following section of this chapter is a reprint of a publication with the same title as of the section. The permission is granted by the American Chemical Society (ACS). The full citation is: B. V. Senkovskiy, M. Pfeiffer, S. K. Alavi, A. Bliesener, J. Zhu, S. Michel, A. V. Fedorov, R. German, D. Hertel, D. Haberer, L. Petaccia, F. R. Fischer, K. Meerholz, P. H. M. van Loosdrecht, K. Lindfors, and A. Grüneis, *Making Graphene Nanoribbons Photoluminescent*, Nano Letters **17**, 4029–4037 (2017) [1].

NANO LETTERS
Letter
pubs.acs.org/NanoLett

Making Graphene Nanoribbons Photoluminescent

B. V. Senkovskiy,[*,†] M. Pfeiffer,[‡] S. K. Alavi,[‡,§] A. Bliesener,[†] J. Zhu,[†] S. Michel,[†] A. V. Fedorov,[†,∥,⊥] R. German,[†] D. Hertel,[‡] D. Haberer,[#] L. Petaccia,[∇] F. R. Fischer,[#] K. Meerholz,[‡] P. H. M. van Loosdrecht,[†] K. Lindfors,[*,‡] and A. Grüneis[*,†]

[†]II. Physikalisches Institut, Universität zu Köln, Zülpicher Strasse 77, 50937 Köln, Germany
[‡]Department für Chemie, Universität zu Köln, Luxemburger Strasse 116, 50939 Köln, Germany
[§]Institut für Angewandte Physik der Universität Bonn, Wegeler Strasse 8, 53115 Bonn, Germany
[∥]St. Petersburg State University, Ulianovskaya 1, St. Petersburg 198504, Russia
[⊥]IFW Dresden, P.O. Box 270116, Dresden D-01171, Germany
[#]Department of Chemistry, University of California at Berkeley, Tan Hall 680, Berkeley, California 94720, United States
[∇]Elettra Sincrotrone Trieste, Strada Statale 14 km 163.5, 34149 Trieste, Italy

Supporting Information

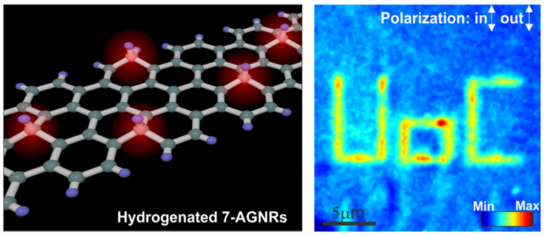

ABSTRACT: We demonstrate the alignment-preserving transfer of parallel graphene nanoribbons (GNRs) onto insulating substrates. The photophysics of such samples is characterized by polarized Raman and photoluminescence (PL) spectroscopies. The Raman scattered light and the PL are polarized along the GNR axis. The Raman cross section as a function of excitation energy has distinct excitonic peaks associated with transitions between the one-dimensional parabolic subbands. We find that the PL of GNRs is intrinsically low but can be strongly enhanced by blue laser irradiation in ambient conditions or hydrogenation in ultrahigh vacuum. These functionalization routes cause the formation of sp^3 defects in GNRs. We demonstrate the laser writing of luminescent patterns in GNR films for maskless lithography by the controlled generation of defects. Our findings set the stage for further exploration of the optical properties of GNRs on insulating substrates and in device geometries.

KEYWORDS: *Graphene, nanoribbons, hydrogenation, photoluminescence, Raman, defects*

One-dimensional (1D) graphene nanoribbons (GNRs) are ideal candidates for materials in the inevitable postsilicon electronics era which will require subnanometer structuring. The large versatility in electronic properties makes it possible to use them as an active element in devices[1−4] with a tunable band gap[5−8] or for metallic interconnects that could outperform copper contacts with a similar dimension.[9] Atomically precise engineering of GNRs is possible thanks to the bottom-up fabrication approach.[10−13] This technique also allows to produce intermolecular junctions between GNRs of different widths[14] and substitutional doping of GNRs.[15,16] Semiconducting armchair GNRs with $N = 7$ carbon atoms width (7-AGNRs) can be grown on vicinal surfaces of Au(788) and have a long-range parallel alignment over the whole single-crystal substrate.[17,18] For an aligned GNR film, the 1D nature is evident in a strong polarization dependent absorption of light. Optical reflectance anisotropy measurements of 7-AGNRs on Au(788) have yielded a lowest peak in the absorption at E_{11} = 2.1 eV which is excitonic in nature.[19] Here E_{11} is the energy of the optical transition between the highest valence to the lowest conduction band. The energetically higher transitions between the i-th valence and conduction band are denoted E_{ii}. The observed anisotropy is common for 1D materials such as carbon nanotubes[20,21] and rooted in depolarization effects, that is the suppression of an applied external electromagnetic field perpendicular to the long axis.[22] Moreover, the dipole selection rules for optical transitions depend on the light polarization and state that, for GNRs, optical transitions between van Hove singularities of symmetric sub-bands are allowed only for light polarized along the GNR axis.[23] Previous studies of GNRs on metallic substrates did not report photoluminescence (PL) because the metallic substrates typically quench PL.[24] PL was observed from GNRs encapsulated inside carbon nanotubes.[25,26] The width of these nanoribbons is determined by the nanotube diameter distribution. Since chirality pure carbon nanotube samples are still challenging, the nanoribbons obtained in this way have nonuniform widths.[25] Moreover, such samples are not aligned and cannot be contacted electrically.

Received: January 11, 2017
Revised: March 29, 2017
Published: March 30, 2017

DOI: 10.1021/acs.nanolett.7b00147
Nano Lett. 2017, 17, 4029−4037

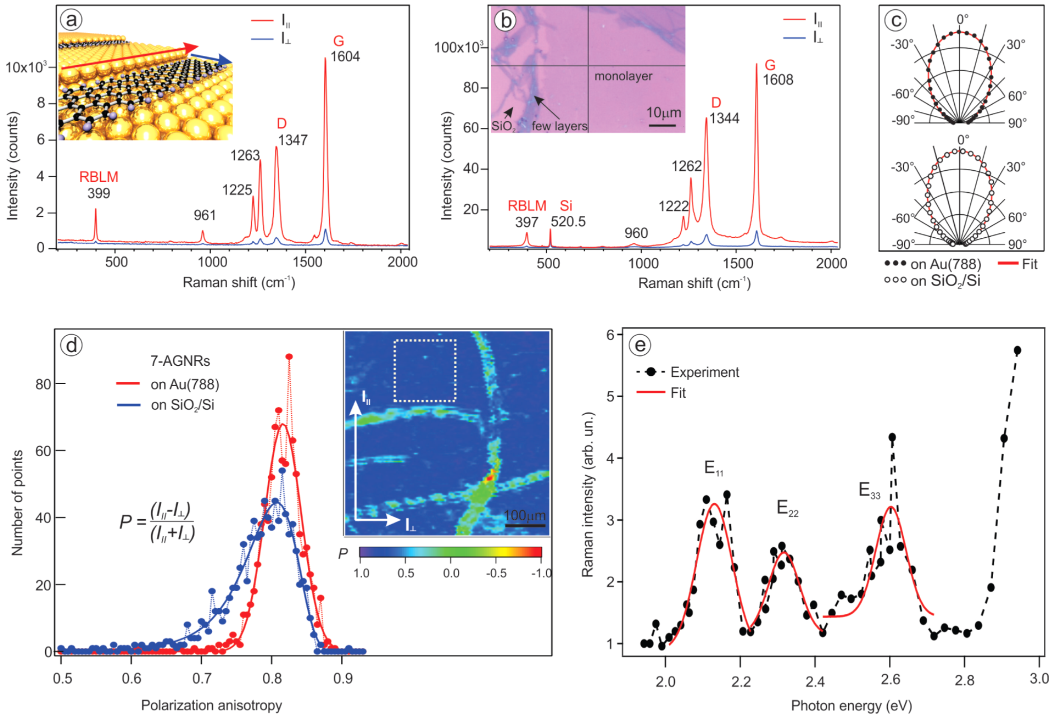

Figure 1. Polarized Raman spectra of 7-AGNRs (a) before and (b) after the transfer from Au(788) onto SiO$_2$, measured inside a UHV Raman system with a 532 nm wavelength laser with two polarizations: along ($I_{\parallel}$) and perpendicular ($I_{\perp}$) to the alignment direction. The inset in panel a shows a sketch of aligned 7-AGNRs on Au(788) and the inset in panel b an optical micrograph of transferred ribbons onto SiO$_2$. (c) Polar diagrams of the Raman intensity of the G mode for 7-AGNRs/Au(788) (top) and on SiO$_2$ (bottom). The fit of the polar diagram using eq 1 is also shown. (d) Histogram plots of Raman polarization anisotropy P for 7-AGNRs on Au(788) and on SiO$_2$ measured over the 150 × 150 μm^2 area (points represent the data, and the solid lines are guides to the eye). The inset shows the spatial distribution of P for 7-AGNRs/SiO$_2$. The area marked by the dashed line was used for the histogram plot. (e) The Raman excitation profile for 7-AGNRs on quartz as a function of photon energy. The peaks in the Raman intensity at exciton energies E_{ii} are indicated. Gaussian fits of the individual peaks in the resonance Raman profile are shown.

From a device perspective, the alignment of GNRs is equally important. For example, in a field effect transistor, one desires to have the GNR orientation along the source−drain direction to have charge transport along the GNR axis, and in optoelectronic devices the absorption and emission of light is most efficient for polarization along the GNR axis. Hence, in order to fully exploit the potential of GNRs for nanoelectronics and optoelectronics, an alignment-preserving transfer method onto insulating surfaces is needed. Very recently, the transfer of chevron type GNRs by etching away the Au(111)/mica substrate has been demonstrated.[27] This procedure involves dissolving the Au substrate in acid. Hence, this method does not work for transferring aligned GNRs from the vicinal surfaces of single-crystal substrates.

The present manuscript addresses these issues. An important point regarding PL of GNRs is that theory predicts that the $N = 3p + 1$ family (where p is an integer) has an optically forbidden (dark) excitonic state with an energy close to E_{11}.[28,29] Therefore, the technologically important 7-AGNRs which have an electron energy band gap in the visible spectral range are not expected to have bright PL in their intrinsic state. This situation is similar to carbon nanotubes,[30−32] where the generation of defects at an energy level below the dark exciton results in a stronger PL.[33] Also graphene can be made luminescent using defects.[34,35] The present work establishes the techniques and the physics for obtaining PL brightening in GNRs.

This manuscript is organized as follows. We first describe a procedure how to transfer aligned 7-AGNRs from Au(788) to insulating substrates (SiO$_2$/Si and quartz wafers). We then characterize the transferred samples using Raman and PL regarding their optical transition energies and their alignment. We subsequently induce PL using blue light illumination in ambient conditions and by in situ hydrogenation in ultrahigh vacuum (UHV). In the context of blue light illumination we also show an application how to write PL active defect patterns.

Let us start by the description of the transfer of large area (cm^2) monolayers of aligned 7-AGNRs from Au(788) onto insulating substrates. Prior to the transfer we characterized samples by a combination of angle-resolved photoemission spectroscopy, scanning-tunneling microscopy, and low energy electron diffraction (see Supporting Information, SI, Figure S1). The Raman measurements of 7-AGNRs on Au(788) using linearly polarized light yield a highly anisotropic signal, as shown in Figure 1a. We have used the 532 nm laser line which is close to the E_{22} transition for 7-AGNRs/Au(788).[19] The most pronounced Raman active modes are the G mode, corresponding to the carbon−carbon bonds stretching along the ribbon, the D mode which can be related to defects or the edges of GNRs,[36] the radial breathing like mode (RBLM)

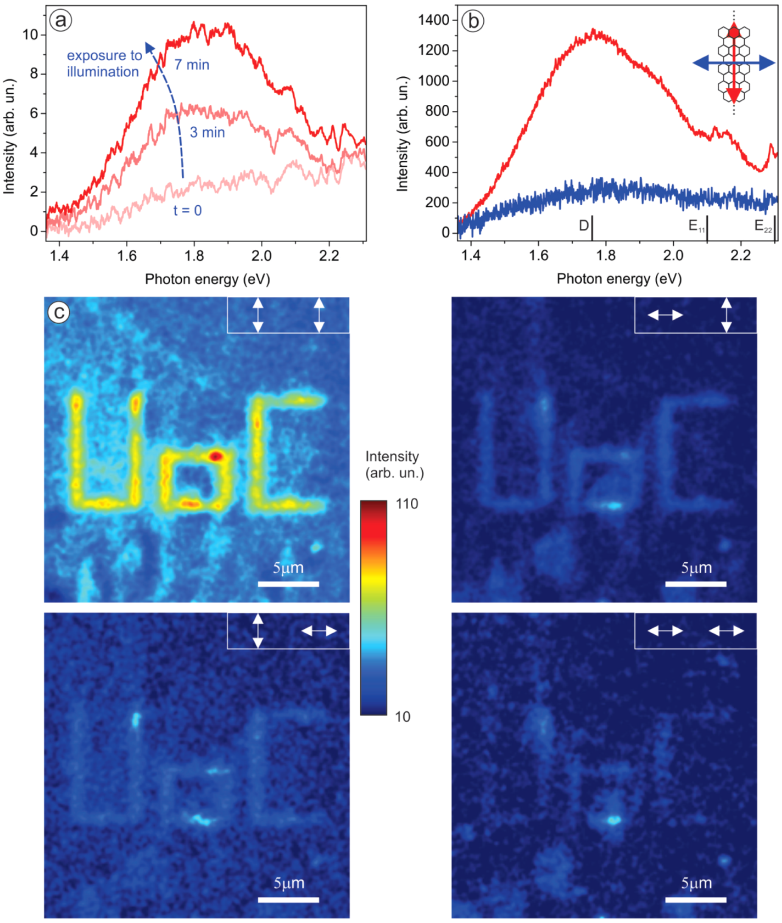

Figure 2. (a) The PL of 7-AGNRs on quartz (peak at ∼1.8 eV) brightens when the sample is exposed to blue light (440 nm). (b) The PL is partially polarized along the GNR axis demonstrating its origin in the GNR. Here the spectra for polarizer and analyzer both parallel to the ribbon axis (red solid line) and both perpendicular to the ribbon axis (blue solid line) are shown. The emission peaks are at a significantly lower photon energy (marked with D) than the excitons E_{11} and E_{22}. (c) Scanning a 440 nm laser focus allows the writing of luminescent patterns on GNR monolayers. Here the letters "UoC" have been rendered bright. The four panels correspond to the four possible orientations of polarizer and analyzer with respect to the GNR axis and are indicated by arrows. The first (second) arrow denotes the polarization of the exciting (analyzed) light. The vertical direction corresponds to light polarization along the GNR axis according to the sketch of a GNR in the inset to b.

related to the ribbon width expansion, and confinement-derived vibration modes[37] at 1225 and 1263 cm^{-1}, respectively. In Figure 1a, $I_{\parallel}$ and $I_{\perp}$ denote the Raman spectra measured for the incident and scattered light polarized along and perpendicular to the step edges of Au(788) with a ratio $I(G)_{\parallel}/I(G)_{\perp} = 11.4$ (peak value of the G band intensity). The observed anisotropy $I_{\parallel}/I_{\perp}$ is a measure of how well the alignment is preserved after transfer. Such a quick and nondestructive way to check the alignment is, e.g., important for device fabrication from GNRs which requires knowledge of the orientation.

We applied the so-called bubbling transfer method which was developed for CVD grown graphene.[38,39] As we will show, the advantage of this technique is that it retains the GNR parallel alignment over hundreds of microns. Furthermore, it does not affect the single crystalline surface of the substrate.[40] Figure 1b depicts the Raman spectra of GNRs after bubbling transfer onto a Si wafer with 300 nm SiO$_2$ for polarization parallel and perpendicular to the GNRs. The inset to Figure 1b depicts an optical micrograph of the transferred sample. The GNR coverage is visible as a slightly darker area in the middle of the micrograph. The optical contrast of a GNR monolayer is similar to graphene.[41,42] The darker regions in some areas close to the corners of the micrograph correspond to multiple 7-AGNRs layers due to wrinkles. After transfer we have $I(G)_{\parallel}/I(G)_{\perp} = 11.1$ for a measurement at a single point. Therefore, we conclude that the GNR alignment is preserved in this sample spot. The transfer process causes a small increase in the D/G band intensity ratio which is a measure of disorder[43] due to remains from the transfer procedure and defects.[44] The D/G ratio is equal to 0.54 (0.71) before (after) the transfer. Interestingly, the intensity of the Raman spectra for 7-AGNRs/SiO$_2$ is increased by a factor ∼9 relative to the spectrum taken on 7-AGNRs/Au(788). This effect can be ascribed to the change in optical environment because the GNRs/SiO$_2$/Si interface causes multiple reflections and interference effects.[45,46] We also find that the G mode is blue-shifted by 4 cm^{-1} on

SiO_2/Si relative to the sample on Au(788). Interestingly, a similar observation (blue-shifts up to 12 cm^{-1}) has been made for graphene on SiO_2/Si compared to metals.[47] For graphene on a substrate with many defects, the blue-shift of the G mode was explained by the presence of charged impurities.[47] Indeed, charged impurities in the SiO_2 substrate are known to be a dominant source of scattering in graphene.[48,49] We believe that the same is true for 7-AGNRs/SiO_2.

Figure 1c shows the polar diagrams of the Raman G mode intensity for 7-AGNRs on Au and on SiO_2 as a function of angle between the electric field vector and the alignment direction. From electromagnetic theory for a point-like Hertz dipole and experiments on carbon nanotubes, we expect a $\cos^4\phi$ law for the Raman intensity.[20,21] Here ϕ is the angle between the laser polarization and the GNR axes. We model the alignment of GNRs by a Gaussian distribution of angles of the GNR axis to the orientation of the Au(788) terraces. This enables us to extract the average misalignment before and after the transfer from the width of the Gaussian distribution. To that end we fit the polar dependence of the Raman signal $I(\theta)$. Here θ is the angle with respect to the terraces. The $I(\theta)$ is given by

$$I(\theta) = \frac{A}{\sigma\sqrt{2\pi}} \int_{-\pi}^{\pi} \cos^4(\phi' - \theta) \exp\left(-\frac{(\phi' - \theta)^2}{2\sigma^2}\right) d\phi' \qquad (1)$$

As a relevant fit result, we obtain σ, the value of the width of the GNR alignment distribution (see eq 1). We find equal values of $\sigma = 9°$ for the GNR alignment distribution before and after the transfer. This indicates that the alignment of the GNRs film is not deteriorating within the area of a randomly chosen laser spot (1 μm^2) after the bubbling transfer. The polar diagrams for the other Raman active phonons are shown in the SI (Figure S1).

Let us now turn to the investigation of the GNR alignment over larger areas. For a quantitative description of the alignment, we define the Raman polarization anisotropy P for all Raman active modes as $P = (I_\parallel - I_\perp)/(I_\parallel + I_\perp)$. For perfect GNR alignment parallel (perpendicular) to the step edges, we have $P = 1$ ($P = -1$), and for a completely random alignment, we have $P = 0$. Histogram plots of P for a 150 × 150 μm^2 area of 7-AGNRs before and after the transfer are shown in Figure 1d (this area is not identical with the area of the photograph in Figure 1b). For 7-AGNRs/Au(788) the histogram has a symmetric shape with the center at $P = 0.82$. After the transfer the histogram acquires an asymmetric shape with the maximum shifted to $P = 0.81$. As a result the distribution peak intensity is reduced by a factor of 1.5. It is clear that the asymmetry in the distribution of P comes from the fact that the alignment of a fraction of the GNRs deteriorates during the transfer process. The inset of Figure 1d shows the spatial distribution of P for 7-AGNRs/SiO_2 with the marked rectangle from which the histogram was computed. It can be seen that large areas have $P \sim 0.8$ which proves the GNR alignment over hundreds of micrometer distances. There are elongated and bent regions, which feature $P = 0$. We ascribe them to multiple folds that can appear during the transfer process. We can conclude that, using the bubbling transfer approach, it is possible to obtain large areas parallel aligned GNRs on an arbitrary substrate.

Having demonstrated the successful transfer of aligned GNRs to insulating substrates, we next study the electronic states of the material. For this purpose we measure resonance Raman spectra for different photon energies of the incident light, which is polarized along the GNRs (see methods for details on the experiments). Figure 1e shows the resonance Raman signal of the G band phonon as a function of the photon energy of the incident light (the raw spectra are shown in Figure S2 of the SI). The Raman excitation spectrum displays peaks at certain energies, which we associate with the excitons E_{ii} in the GNRs.[50] We determine the positions as $E_{11} = 2.1$ eV, $E_{22} = 2.3$ eV, and $E_{33} = 2.6$ eV. The rise of the Raman cross section at energies higher than E_{33} is ascribed to a combination of absorption of light at higher E_{ii} transitions and at the saddle point singularity which appears in all sp^2 carbon materials. For graphene, this transition occurs at 4.62 eV.[51]

Let us now turn to the photoluminescence of GNRs. When GNRs are illuminated with focused 440 nm wavelength light in a laser scanning confocal microscope under ambient conditions, we observe weak emission without distinct spectral features as illustrated by the PL spectrum shown in Figure 2a (see methods for details on the PL experiments). For a defect-free sample, the PL is expected to be dark. Surprisingly, when the sample is continuously exposed to 440 nm radiation, the emission brightens after 1 min, and a peak at approximately 1.8 eV emerges in the spectrum. Regarding the kinetics of defect generation, we find that, for an incident intensity at the microscope focus of approximately 100 kW/cm^2, it takes approximately 5 min for the brightening to saturate depending on the wavelength. We attribute the increased emission to the generation of defects in GNRs via a photochemical reaction. The initially very weak fluorescence before exposure to 440 nm light is a signature of the existence of dark excitons energetically either degenerate with the lowest lying optically active exciton E_{11} or positioned below this bright transition as predicted in theoretical studies.[28,29,52,53] The weak but not completely absent PL emission before exposure to blue light is ascribed to the presence of defects, which were generated either during sample growth or transfer, or which formed in laboratory conditions after the sample was removed from UHV. Sample transfer as the cause of the defects is supported by the fact that we observed an increase in the D/G Raman ratio (see Figure 1) although we remark that not all defects are expected to result in brightening of luminescence.

It is important to distinguish between the wavelengths of the light needed to efficiently generate defects and the light used to excite PL. We find that, for defect generation, the sample must be exposed to light with wavelengths shorter than approximately 510 nm. For longer wavelengths the PL remains dim independent of the photon energy used to excite PL. Once we have generated defects, we can probe the dependence of the PL spectrum on the exciting light wavelength. To that end we have performed PL measurements (data not shown here) varying the excitation wavelength from 420 to 590 nm and observe a similar emission spectrum for all excitation wavelengths. This demonstrates that the observed emission originates from an energetically well-defined transition.

Figure 2b shows that the PL displays a significant polarization anisotropy across the spectral range of the emission. The emission is the maximum for polarization along the ribbons. The fact that the emission is polarized definitively proves that the emission originates from the ribbons. Figure S5 in the SI depicts a quantitative characterization of the degree of polarization. The linearly polarized PL emission is typical for 1D objects. The observed brightening of the PL is similar to that observed in carbon nanotubes.[33,54,55]

DOI: 10.1021/acs.nanolett.7b00147
Nano Lett. 2017, 17, 4029−4037

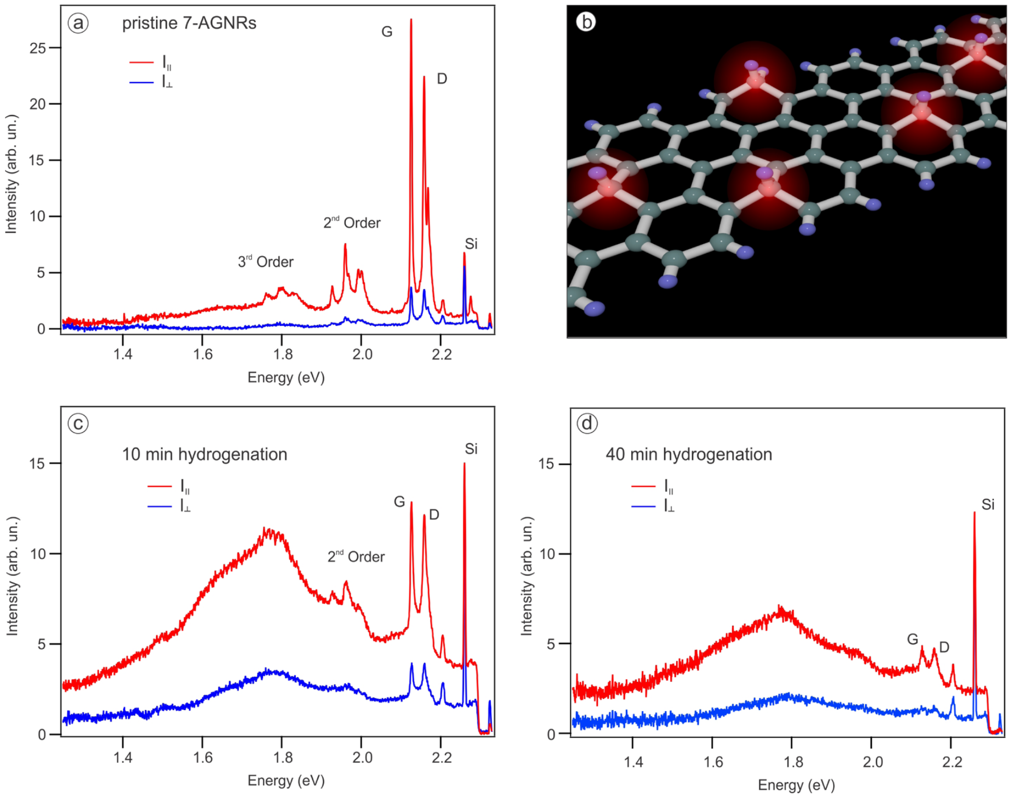

Figure 3. (a) PL and Raman spectra of transferred 7-AGNRs/SiO_2 measured inside a UHV chamber after annealing at 300 °C. Red and blue lines indicate the spectrum recorded along ($I_{\|}$) and perpendicular ($I_{\perp}$) to the alignment direction, respectively. (b) Sketch of the hydrogenated ribbons. (c, d) PL and Raman spectra of the system after 10 min and after 40 min of atomic hydrogen exposure. A polarized PL peak is induced by sp^3 hydrogen defects.

For unperturbed nanotubes fluorescence is very weak due to dark excitons at the energetic position of the optically active transition. Photochemically inducing defects into the nanotubes modifies the energy level structure resulting in a significant increase in fluorescence. In the present case, the photochemical reaction between 7-AGNRs and oxygen and moisture of ambient air but also a photoinduced reaction of 7-AGNRs with the SiO_2 surface[56] are thought to be key for the generation of defects that lead to PL. This is suggested by the observation that the rate of the photoinduced modification is suppressed if blue laser illumination is performed under high-vacuum conditions (data not shown here). The reaction of oxygen with graphene can form more than one type of sp^3 defect in the basal plane (e.g., ether, epoxide, ketone) but also edge defects.[35,57,58] This is also known from graphene oxide which is formed by the oxidation of graphene using strong acids in ambient conditions.[35] The PL of graphene oxide occurs at a very similar energy (maximum PL at 1.8−1.9 eV)[34,35] than observed here for GNRs.

We have compared the Raman spectrum before and after inducing defects photochemically. We observe no change in the position of the *D* and *G* Raman modes but a 25% decrease in the intensities of both lines (see SI Figure S3b). The decrease eventually saturates in similar fashion as the PL signal increases. This further demonstrates that the photochemical modification does not result in major degradation of the GNR structure. Regarding the time constants, we note that PL decay is equal to the instrument response function and faster than 500 ps. This points to a fluorescence process instead of slow phosphorescence and toward a significant nonradiative rate, possibly due to the dark exciton at E_{11} (see SI Figure S4a). Another important point is whether PL bleaches after certain durations of excitation. To that end we collected PL over longer time frames and can confirm the absence of bleaching (see SI Figure S4b).

Due to the ambient conditions of the experiment, a direct proof of the sp^3 nature of the defect by X-ray photoemission (XPS) and near-edge X-ray absorption (NEXAFS) spectroscopies is not possible as this would require in situ functionalization in UHV conditions. At the end of the description of the results we present in situ studies of hydrogenated 7-AGNRs which allow for a combined PL, XPS, and NEXAFS investigation of the chemical nature and luminescent properties of hydrogen defects.

We next demonstrate an application of the laser-induced PL brightening. By scanning the laser focus, we can write luminescent patterns in the GNR film. Figure 2c shows spectrally integrated fluorescence micrographs of a region of the sample where we have exposed the pattern in the form of the letters “UoC” using a 440 nm wavelength light. The PL has been measured using 532 nm light. The emission is significantly brighter in the regions exposed to the blue light. However, the surrounding region is not completely dark and demonstrates that a small number of defects are present as discussed in the preceding section. The emission process is polarization-dependent in both the excitation and emission as a consequence of the high level of alignment of the ribbons. The four panels show the fluorescence under the four possible combinations of excitation and emission light polarized parallel and perpendicular to the GNR axis. The two arrows in each panel denote the light polarization for excitation (left arrow) and emission (right arrow). Here, a vertical arrow denotes light polarization along the GNRs, and a horizontal arrow denotes light polarization perpendicular to the GNRs. It can be seen that the brightest PL pattern appears for both excitation and emission light polarized along the GNR (upper left panel of Figure 2c). If either excitation or emission are polarized perpendicular to the GNR, we obtain a medium intensity PL pattern. This situation corresponds to the upper-right and lower-left panels of Figure 2c. Finally, the weakest PL pattern is observed, if both the polarization of excitation and emission are perpendicular to the GNR axis. This situation is depicted in the bottom-right panel of Figure 2c. Both the bright, photochemically modified regions (the letters "UoC") and the surrounding areas show the same polarization dependence over the spectral range covering the PL emission. This indicates that light exposure does not destroy the ribbons (see SI Figure S5). Thus, the writing of luminescent patterns could be useful in situations where small structures are needed. Maskless lithography is an important tool in nanotechnology and has previously been performed, e.g., by aqueous electro-oxidation of diamond-like carbon films using an atomic force microscope.[59] The present approach does not require a local probe and is therefore faster and easier to perform.

Blue laser illumination in ambient conditions is a viable route to write bright photoluminescent patterns. However, controlled experiments in an UHV environment are needed to correlate the atomic structure of the defect to the appearance of PL. In order to investigate the PL from a defined defect other routes for defect generation are needed. Here we show how to induce sp^3 defects in 7-AGNR samples by hydrogenation in UHV conditions.

Hydrogen sp^3 defects in graphene based carbon materials can be readily induced by exposure to a beam of atomic hydrogen which form C−H bonds in the basal plane of graphene and perpendicular to the nanotube walls.[60−64] The hydrogenation of transferred GNRs on SiO_2/Si and the PL experiments were performed inside a home-built UHV PL system (see methods) without exposing the sample to air after hydrogenation. In such a well-defined experiment, the PL can be definitely ascribed to sp^3 defects formed by C−H bonds. The sp^3 character of these defects can be confirmed by XPS and NEXAFS spectroscopies (see SI, Figure S6). Figure 3a depicts the PL spectra of the sample inside UHV before hydrogenation measured with a 532 nm laser with light polarized parallel and perpendicular to the GNRs. The spectra exhibit strong Raman modes and their higher orders. It is seen that intrinsically PL from 7-AGNRs is very weak. The exposure to a beam of atomic hydrogen[63,64] induces defects where additional hydrogen-carbon bonds are formed, as illustrated in Figure 3b. It can be seen from Figure 3c that the hydrogenation (10 min exposure) leads to a strong polarized PL peak with a maximum at around 1.8 eV. At the same time, the Raman signal from ribbons becomes weaker. We believe that this is due to the fact that the number of resonant sp^2 bonds is reduced. We also observe disorder induced broadening of the Raman lines. This is presumably due to the random nature of chemisorbed H atoms. The longer exposure (40 min) to atomic hydrogen corresponds to the maximum amount of hydrogen that can be chemisorbed to 7-AGNRs. A quantitative analysis of the PL of hydrogenated GNRs yields an increase by a factor of 5 for 10 min hydrogenation (see SI, Figure S7 and Table S1). Note that the PL intensity (as well as the Raman intensity) can be affected by interference effects and thus the obtained values for the PL intensity enhancement depend on the SiO_2 thickness. XPS allows us to estimate the amount of hydrogenated C atoms for the 40 min exposure. We obtain a maximum value of ∼25% (see SI Figure S6). This is identical to the maximum hydrogen coverage observed for epitaxial single-layer graphene.[64] The PL spectrum in Figure 3d displays further reduction of the Raman peaks and an increase of the PL intensity relative to the Raman signal. However, the absolute intensity of PL is decreased when compared to the 10 min exposure. This is due to the fact that the PL intensity depends upon the absorption of incident light. We speculate that this absorption is becoming less effective as more and more sp^2 bonds are broken. Thus, to observe the maximum PL signal from 7-AGNRs, there is a compromise between the luminescence and absorption efficiency.

Finally we discuss the similarity of the PL spectra of defective 7-AGNRs using the two routes for engineering defects (blue laser illumination and hydrogenation). The fact that the peak positions of the PL for both kinds of defects are very similar to each other is not surprising because the electronic structure of these sp^3 defects is similar. This is supported by a work on PL from defective nanotubes using nine different functional groups that bond in an sp^3 manner.[54] The emission energies of these nine sp^3 defects were within an energy window of 40 meV. We also wish to point out that a more detail comparison of the PL of different defects would require a dedicated study using identical excitation energies and substrates. In particular, it is well-known that the thin SiO_2 layer on top of the Si wafer acts as a cavity and can enhance/suppress the emission of certain wavelengths.

In conclusion, we have performed a full photophysical characterization using polarized Raman and luminescence measurements of 7-AGNRs on insulating substrates. To that end we have adapted the bubbling transfer method to transfer monolayers of 7-AGNRs from Au(788) keeping their parallel alignment. We have demonstrated that polarized Raman spectroscopy is a quick and simple tool to analyze the GNR alignment before and after the transfer. The Raman excitation profile as a function of exciting laser energy shows a series of distict peaks which we identified with the E_{11}, E_{22}, and E_{33} excitons. Optical excitation with an energy equal to one of the E_{ii} energies enhances the Raman or PL signal.

7-AGNRs in the pristine state are only weakly photoluminescent. This is evidence in favor of dark excitonic states arising from the optically forbidden E_{12} and E_{21} transition.[23] These dark excitons are expected to be in the vicinity of the lowest bright state in $N = 3p + 1$ AGNRs and are the channels for nonradiative relaxation.[28,29] We have demonstrated two ways of inducing photoluminescence with light emission at about 1.8 eV polarized along the GNR axis. The first is by blue laser illumination in ambient conditions and the second by UHV hydrogenation. The laser writing of photoluminescent patterns in GNR monolayers has been demonstrated and could find technological applications as a cheap and quick maskless lithographic method for structuring GNR films.

DOI: 10.1021/acs.nanolett.7b00147
Nano Lett. 2017, 17, 4029−4037

Regarding future research avenues, it would be interesting to transfer and spectroscopically characterize other GNR chiralities using PL. This is especially true for the GNRs belonging to the $N = 3p$ family for which theory predicts the absence of the dark excitons lower in energy than E_{11}[28,29] such as the $N = 9$ GNR which has only recently been synthesized and characterized.[65] Moreover, the energy and the intensity of the PL for different defects such as vacancies and sp^3 carbon impurities (diamond-like defects) could be investigated. These defects may be formed by ion bombardement or the evaporation of C atoms onto a GNR sample. Recently it was shown that atomically precise doping by heteroatoms such as boron can be performed in GNRs.[15] We believe that the investigation of PL in boron doped bottom-up fabricated GNRs could be interesting as the boron atoms modify the electronic structure and therefore may affect the PL. The boron site in these ribbons is also believed to be chemically active and might act as a chemical anchor for adsorption of molecules or atoms. This could be used as a template for atomically precise functionalization by luminescent molecules. Another interesting research direction would be to build optically active heterostructures out of GNRs of different chiralities and orientations or between GNRs and 2D materials. In such devices, one could observe exciton transfer between the layers. Finally, it could be interesting to employ the presented UHV-PL system for the investigation of trions in alkali doped 7-AGNRs.[66]

Methods. *Growth.* 7-AGNRs were synthesized by surface polymerization of 10,10-dibromo-9,9-bianthryl (DBBA) molecules[11] on Au(111) and Au(788) surfaces. The gold substrates were cleaned by three cycles of Ar^+ sputtering (800 V) and subsequent annealing at 500 °C. DBBA molecules were evaporated from a quartz crucible using a home-built evaporator with a thermocouple attached to the molecule reservoir. The deposition rate was controlled using a quartz microbalance. About 8 Å of precursor molecules (using the graphite density and Z-factor) were evaporated onto the Au surface which was kept at room-temperature. Hereafter, a two-step polymerization reaction was performed: a 200 °C annealing step followed by a 400 °C annealing step, which induce debromization and cyclodehydrogenation reactions, respectively. The annealing was carried out using a computer-controlled ramp that increased temperature over several hours.

STM. STM measurements were performed using an Omicron LT-STM with the samples held at 4.5 K in UHV. A tungsten tip was used for topography and spectroscopic measurements. Topographic images were acquired in constant current mode. dI/dV spectra were obtained using the lock-in technique where the tip bias was modulated by a 457 Hz, 10 mV (rms) sinusoidal voltage under open-feedback conditions. All STM images were processed with WSxM.[67]

XPS, NEXAFS, and ARPES. XPS and NEXAFS experiments were performed at the German-Russian beamline (RGBL) of the HZB BESSY II synchrotron radiation facility (Berlin, Germany). XPS spectra were measured with photon energy of 490 eV and pass energy of 10 eV in the normal emission geometry. NEXAFS data were obtained in total electron yield mode with an energy resolution of 50 meV close to the C K-edge. ARPES was carried out at the BaDElPh beamline of the Elettra synchrotron radiation facility (Trieste, Italy) using a SPECS Phoibos 150 hemispherical electron analyzer. The ARPES spectra were measured using a photon energy of 27 eV in the second BZ of the GNRs and shifted back by application of the reciprocal lattice vector to the first BZ. The samples for XPS, NEXAFS, and ARPES measurements were synthesized and checked in the UHV Raman chamber and then transferred under UHV conditions into a special container which was filled then to a slight overpressure (1.1 bar) by high-purity Ar gas. Samples in UHV tight vacuum suitcases filled with argon gas were transported to the load-lock chamber of the beamline endstation and later gently annealed (at 200 °C) under UHV conditions. This method allowed us to achieve reproducible experimental results.

Raman. The polarization-dependent scanning Raman was performed in backscattering geometry using a commercial Raman system (Renishaw) integrated in a home-built optical UHV chamber where the exciting and Raman scattered light were coupled into the vacuum using a long-working distance microscope objective with an NA of ~0.4. The laser power on the sample was kept below 1 mW. Raman spectra were calibrated using Si peak at 520.5 cm^{-1}. A half-wave plate was used to rotate the polarization of the laser beam. To collect a certain polarization of the Raman light, a polarizer and a half-wave plate were inserted before the detector. All Raman spectra and the map in Figure 1 have been measured inside a UHV chamber. The Raman spectra have been normalized to the laser power, integration time, and system response. Raman spectra as a function of the energy of the incident photons were acquired using an in-house developed laser-scanning confocal microscope. A supercontinuum laser (NKT SuperK EXTREME) and a variable bandpass filter (NKT SuperK VARIA) provides bright tunable radiation. To narrow the spectral bandwidth of the excitation light, we additionally use a tunable grating filter. A second similar tunable filter was used in the detection to remove the incident laser light. The incident light is focused on the sample using a microscope objective with numerical aperture 0.8 (Olympus MPLFLN). Finally, the spectra were acquired with a grating spectrometer (Princeton Instruments IsoPlane) equipped with a deep-cooled back-illuminated CCD. The strength of the Raman signals was extracted from Lorentzian fits to the Raman G-mode. The spectra were corrected using the wavelength-dependent sensitivity of the setup. The power in the experiments was kept below 200 μW for a diffraction limited spot.

Photoluminescence. Photoluminescence was measured in a sample-scanning laser scanning confocal microscope. The polarization-sensitive measurements were performed with an achromatic half-wave plate and a polarizer in the excitation path. In the detection path we used an optical long-pass filter. We further place a polarizer to act as an analyzer behind the long-pass filter. This is followed by an achromatic quarter-wave plate oriented at 45° with respect to the analyzer polarization axis. This results in polarization-independent propagation of the luminescence light through the optical train to the detector. All spectra were normalized with the power of the incident light and corrected for the polarization dependencies of the optical train before the analyzer. The power in the experiments was kept below 150 μW for a diffraction limited spot. The PL of hydrogenated 7-AGNRs was measured in situ using the UHV Raman setup (see above). For PL measurements, a filter with a larger bandwidth than in the Raman experiments has been used.

Hydrogenation of Graphene Nanoribbons. To clean the surface prior to hydrogenation the aligned 7-AGNRs/SiO_2 were annealed in the UHV chamber (base pressure was 2×10^{-10} mbar) at 300 °C for 12 h. The hydrogenation of GNRs was performed by cracking H_2 molecules in a tungsten capillary which was heated to temperatures above 1800−2000 K. The hydrogen flux was controlled by a needle valve. A pressure of 10^{-6} mbar was applied during hydrogenation.

Bubbling Transfer. To transfer 7-AGNRs from Au(788) onto insulating substrates (300 nm SiO_2/Si or quartz), we used the bubbling transfer technique based on the electrochemical delamination process.[38,39] The 7-AGNRs/Au(788) sample was coated with poly(methyl methacrylate) (PMMA) with a molecular weight of 180 kDa and placed in an electrochemical cell with an NaOH aqueous solution (1 mol/L). A reference mark on the Au(788) crystal shows the direction of (111) terraces. At the negatively charged cathode, the PMMA/7-AGNRs layer was detached from the Au(788) substrate by the emerging H_2 gas bubbles due to the reduction of water. The floating PMMA/7-AGNRs layer was then cleaned in distilled water and placed onto the substrate. To remove PMMA and clean the sample surface, we employed acetic acid (96% in H_2O) and methanol. This treatment removes residual PMMA contaminants efficiently.[68]

■ ASSOCIATED CONTENT

Ⓢ Supporting Information

The Supporting Information is available free of charge on the ACS Publications website at DOI: 10.1021/acs.nanolett.7b00147.

> STM, ARPES, and LEED measurements of the aligned 7-AGNRs on Au(788). Sketch of the bubbling transfer setup. Polar diagram of the Raman intensities of the RBLM and D modes, respectively. Photograph of the transferred 7-AGNR film. Raw energy dependent Raman data. Raman and photoluminescence spectra before and after defect generation. Time-resolved fluorescence and instrument response function. Absence of bleaching of photoluminescence from GNRs. Polarization anisotropy for the excitation and emission of GNRs/quartz. XPS and NEXAFS of hydrogenated 7-AGNRs on Au(111). Quantification of photoluminescence increase after hydrogenation (PDF)

■ AUTHOR INFORMATION

Corresponding Authors

*E-mail: senkovskiy@ph2.uni-koeln.de.
*E-mail: klas.lindfors@uni-koeln.de.
*E-mail: grueneis@ph2.uni-koeln.de.

ORCID

M. Pfeiffer: 0000-0002-1402-0374
F. R. Fischer: 0000-0003-4723-3111
A. Grüneis: 0000-0003-2448-6060

Author Contributions

B.V.S., M.P., and S.K.A. contributed equally to this work.

Notes

The authors declare no competing financial interest.

■ ACKNOWLEDGMENTS

B.S., S.M., A.F., and A.G. acknowledge the ERC grant no. 648589 "SUPER-2D", funding from DFG projects CRC 1238 (project A1) and GR 3708/2-1. Research supported by the U.S. Department of Energy (DOE), Office of Science, Basic Energy Sciences (BES), under Award No. DE-SC0010409 (design, synthesis, and characterization of molecular building blocks) and the Center for Energy Efficient Electronics Science NSF Award 0939514 (SPM imaging and spectroscopy). The research leading to these results has received funding from the European Community's Seventh Framework Programme (FP7/2007-2013) under grant agreement no. 312284 (CALIPSO). We thank Elettra for the allocation of synchrotron radiation beamtimes. The stay at the Elettra synchrotron has been supported by the CERIC−ERIC consortium. The authors thank HZB BESSY II and the Russian-German Laboratory (RGBL) for the beamtime allocation. S.K.A. thanks the Bonn-Cologne Graduate School for Physics and Astronomy and DAAD for financial support. J.Z., R.G., and P.L. acknowledge DFG project CRC1238 (project B03). This work has been supported by the University of Cologne through the Institutional Strategy of the University of Cologne within the German Excellence Initiative.

■ REFERENCES

(1) Chen, Z.; Lin, Y.-M.; Rooks, M. J.; Avouris, P. *Phys. E* **2007**, *40*, 228−232. International Symposium on Nanometer-Scale Quantum Physics.

(2) Wang, X.; Ouyang, Y.; Li, X.; Wang, H.; Guo, J.; Dai, H. *Phys. Rev. Lett.* **2008**, *100*, 206803.

(3) Kim, W. Y.; Kim, K. S. *Nat. Nanotechnol.* **2008**, *3*, 408−412.

(4) Bennett, P. B.; Pedramrazi, Z.; Madani, A.; Chen, Y.-C.; de Oteyza, D. G.; Chen, C.; Fischer, F. R.; Crommie, M. F.; Bokor, J. *Appl. Phys. Lett.* **2013**, *103*, 253114.

(5) Nakada, K.; Fujita, M.; Dresselhaus, G.; Dresselhaus, M. S. *Phys. Rev. B: Condens. Matter Mater. Phys.* **1996**, *54*, 17954−17961.

(6) Yang, L.; Park, C.-H.; Son, Y.-W.; Cohen, M. L.; Louie, S. G. *Phys. Rev. Lett.* **2007**, *99*, 186801.

(7) Barone, V.; Hod, O.; Scuseria, G. E. *Nano Lett.* **2006**, *6*, 2748−2754. PMID: 17163699.

(8) Chen, Y.-C.; de Oteyza, D. G.; Pedramrazi, Z.; Chen, C.; Fischer, F. R.; Crommie, M. F. *ACS Nano* **2013**, *7*, 6123−6128.

(9) Naeemi, A.; Meindl, J. D. *IEEE Electron Device Lett.* **2007**, *28*, 428−431.

(10) Grill, L.; Dyer, M.; Lafferentz, L.; Persson, M.; Peters, M. V.; Hecht, S. *Nat. Nanotechnol.* **2007**, *2*, 687−691.

(11) Cai, J.; Ruffieux, P.; Jaafar, R.; Bieri, M.; Braun, T.; Blankenburg, S.; Muoth, M.; Seitsonen, A. P.; Saleh, M.; Feng, X.; Müllen, K.; Fasel, R. *Nature* **2010**, *466*, 470−473.

(12) Ruffieux, P.; Wang, S.; Yang, B.; Sànchez-Sànchez, C.; Liu, J.; Dienel, T.; Talirz, L.; Shinde, P.; Pignedoli, C. A.; Passerone, D.; Dumslaff, T.; Feng, X.; Müllen, K.; Fasel, R. *Nature* **2016**, *531*, 489.

(13) Talirz, L.; Ruffieux, P.; Fasel, R. *Adv. Mater.* **2016**, *28*, 6222−6231.

(14) Chen, Y.-C.; Cao, T.; Chen, C.; Pedramrazi, Z.; Haberer, D.; de Oteyza, D.; Fischer, F.; Louie, S.; Crommie, M. *Nat. Nanotechnol.* **2015**, *10*, 156.

(15) Cloke, R. R.; Marangoni, T.; Nguyen, G. D.; Joshi, T.; Rizzo, D. J.; Bronner, C.; Cao, T.; Louie, S. G.; Crommie, M. F.; Fischer, F. R. *J. Am. Chem. Soc.* **2015**, *137*, 8872−8875. PMID: 26153349.

(16) Kawai, S.; Saito, S.; Osumi, S.; Yamaguchi, S.; Foster, A. S.; Spijker, P.; Meyer, E. *Nat. Commun.* **2015**, *6*, 8098.

(17) Linden, S.; Zhong, D.; Timmer, A.; Aghdassi, N.; Franke, J. H.; Zhang, H.; Feng, X.; Müllen, K.; Fuchs, H.; Chi, L.; Zacharias, H. *Phys. Rev. Lett.* **2012**, *108*, 216801.

(18) Ruffieux, P.; Cai, J.; Plumb, N. C.; Patthey, L.; Prezzi, D.; Ferretti, A.; Molinari, E.; Feng, X.; Müllen, K.; Pignedoli, C. A.; Fasel, R. *ACS Nano* **2012**, *6*, 6930−6935. PMID: 22853456.

(19) Denk, R.; Hohage, M.; Zeppenfeld, P.; Cai, J.; Pignedoli, C. A.; Söde, H.; Fasel, R.; Feng, X.; Müllen, K.; Wang, S.; Prezzi, D.; Ferretti, A.; Ruini, A.; Molinari, E.; Ruffieux, P. *Nat. Commun.* **2014**, *5*, 4253.

(20) Duesberg, G. S.; Loa, I.; Burghard, M.; Syassen, K.; Roth, S. *Phys. Rev. Lett.* **2000**, *85*, 5436−5439.

(21) Ichida, M.; Mizuno, S.; Kataura, H.; Achiba, Y.; Nakamura, A. *Appl. Phys. A: Mater. Sci. Process.* **2004**, *78*, 1117−1120.

(22) Ajiki, H.; Ando, T. *Phys. B* **1994**, *201*, 349−352.

(23) Sasaki, K.; Kato, K.; Tokura, Y.; Oguri, K.; Sogawa, T. *Phys. Rev. B: Condens. Matter Mater. Phys.* **2011**, *84*, 085458.

(24) Johansson, P.; Xu, H.; Käll, M. *Phys. Rev. B: Condens. Matter Mater. Phys.* **2005**, *72*, 035427.

(25) Chernov, A. I.; Fedotov, P. V.; Talyzin, A. V.; Suarez Lopez, I.; Anoshkin, I. V.; Nasibulin, A. G.; Kauppinen, E. I.; Obraztsova, E. D. *ACS Nano* **2013**, *7*, 6346−6353. PMID: 23795665.

(26) Lim, H. E.; Miyata, Y.; Fujihara, M.; Okada, S.; Liu, Z.; Arifin; Sato, K.; Omachi, H.; Kitaura, R.; Irle, S.; Suenaga, K.; Shinohara, H. *ACS Nano* **2015**, *9*, 5034−5040. PMID: 25868574.

(27) Chen, Z.; et al. *J. Am. Chem. Soc.* **2016**, *138*, 15488−15496. PMID: 27933922

(28) Yang, L.; Cohen, M. L.; Louie, S. G. *Nano Lett.* **2007**, *7*, 3112−3115. PMID: 17824720.

(29) Prezzi, D.; Varsano, D.; Ruini, A.; Marini, A.; Molinari, E. *Phys. Rev. B: Condens. Matter Mater. Phys.* **2008**, *77*, 041404.

(30) Wang, F.; Dukovic, G.; Brus, L. E.; Heinz, T. F. *Science* **2005**, *308*, 838−841.

(31) Maultzsch, J.; Pomraenke, R.; Reich, S.; Chang, E.; Prezzi, D.; Ruini, A.; Molinari, E.; Strano, M. S.; Thomsen, C.; Lienau, C. *Phys. Rev. B: Condens. Matter Mater. Phys.* **2005**, *72*, 241402.

(32) Srivastava, A.; Htoon, H.; Klimov, V. I.; Kono, J. *Phys. Rev. Lett.* **2008**, *101*, 087402.

(33) Miyauchi, Y.; Iwamura, M.; Mouri, S.; Kawazoe, T.; Ohtsu, M.; Matsuda, K. *Nat. Photonics* **2013**, *7*, 715−719.

(34) Gokus, T.; Nair, R. R.; Bonetti, A.; Böhmler, M.; Lombardo, A.; Novoselov, K. S.; Geim, A. K.; Ferrari, A. C.; Hartschuh, A. *ACS Nano* **2009**, *3*, 3963−3968.

(35) Loh, K. P.; Bao, Q.; Eda, G.; Chhowalla, M. *Nat. Chem.* **2010**, *2*, 1015−1024.

(36) Sasaki, K.-i.; Kato, K.; Tokura, Y.; Suzuki, S.; Sogawa, T. *Phys. Rev. B: Condens. Matter Mater. Phys.* **2012**, *85*, 075437.

(37) Vandescuren, M.; Hermet, P.; Meunier, V.; Henrard, L.; Lambin, P. *Phys. Rev. B: Condens. Matter Mater. Phys.* **2008**, *78*, 195401.

(38) Gao, L.; Ren, W.; Xu, H.; Jin, L.; Wang, Z.; Ma, T.; Ma, L.-P.; Zhang, Z.; Fu, Q.; Peng, L.-M.; Bao, X.; Cheng, H.-M. *Nat. Commun.* **2012**, *3*, 699.

(39) Wang, Y.; Zheng, Y.; Xu, X.; Dubuisson, E.; Bao, Q.; Lu, J.; Loh, K. P. *ACS Nano* **2011**, *5*, 9927−9933. PMID: 22034835.

(40) Rakic, I. S.; Capeta, D.; Plodinec, M.; Kralj, M. *Carbon* **2016**, *96*, 243−249.

(41) Blake, P.; Hill, E. W.; Castro Neto, A. H.; Novoselov, K. S.; Jiang, D.; Yang, R.; Booth, T. J.; Geim, A. K. *Appl. Phys. Lett.* **2007**, *91*, 6.

(42) Yoon, D.; Moon, H.; Son, Y.-W.; Choi, J. S.; Park, B. H.; Cha, Y. H.; Kim, Y. D.; Cheong, H. *Phys. Rev. B: Condens. Matter Mater. Phys.* **2009**, *80*, 125422.

(43) Venezuela, P.; Lazzeri, M.; Mauri, F. *Phys. Rev. B: Condens. Matter Mater. Phys.* **2011**, *84*, 035433.

(44) Cancado, L. G.; Takai, K.; Enoki, T.; Endo, M.; Kim, Y.; Mizusaki, H.; Jorio, A.; Coelho, L. N.; Magalhaes-Paniago, R.; Pimenta, M. A. *Appl. Phys. Lett.* **2006**, *88*, 163106.

(45) Liu, C.; Ma, Y.; Li, W.; Dai, L. *Appl. Phys. Lett.* **2013**, *103*, 213103.

(46) Wang, Y. Y.; Ni, Z. H.; Shen, Z. X.; Wang, H. M.; Wu, Y. H. *Appl. Phys. Lett.* **2008**, *92*, 043121.

(47) Das, A.; Chakraborty, B.; Sood, A. K. *Bull. Mater. Sci.* **2008**, *31*, 579−584.

(48) Rossi, E.; Das Sarma, S. *Phys. Rev. Lett.* **2008**, *101*, 166803.

(49) Burson, K. M.; Cullen, W. G.; Adam, S.; Dean, C. R.; Watanabe, K.; Taniguchi, T.; Kim, P.; Fuhrer, M. S. *Nano Lett.* **2013**, *13*, 3576−3580. PMID: 23879288.

(50) Thomsen, C.; Reich, S. In *Light Scattering Solids IX*; Cardona, M., Ed.; Springer-Verlag: Berlin, 2007; Vol. *108*, pp 115−235.

(51) Mak, K. F.; Shan, J.; Heinz, T. F. *Phys. Rev. Lett.* **2011**, *106*, 046401.

(52) Dutta, S.; Lakshmi, S.; Pati, S. K. *Phys. Rev. B: Condens. Matter Mater. Phys.* **2008**, *77*, 073412.

(53) Alfonsi, J.; Meneghetti, M. *New J. Phys.* **2012**, *14*, 053047.

(54) Piao, Y.; Meany, B.; Powell, L. R.; Valley, N.; Kwon, H.; Schatz, G. C.; Wang, Y. *Nat. Chem.* **2013**, *5*, 840−845.

(55) Ghosh, S.; Bachilo, S. M.; Simonette, R. A.; Beckingham, K. M.; Weisman, R. B. *Science* **2010**, *330*, 1656−1659.

(56) Imamura, G.; Saiki, K. *ACS Appl. Mater. Interfaces* **2015**, *7*, 2439−2443. PMID: 25569142.

(57) Vinogradov, N. A.; Schulte, K.; Ng, M. L.; Mikkelsen, A.; Lundgren, E.; Martensson, N.; Preobrajenski, A. B. *J. Phys. Chem. C* **2011**, *115*, 9568−9577.

(58) Larciprete, R.; Fabris, S.; Sun, T.; Lacovig, P.; Baraldi, A.; Lizzit, S. *J. Am. Chem. Soc.* **2011**, *133*, 17315−17321. PMID: 21846143.

(59) Mühl, T.; Myhra, S. *Nanotechnology* **2007**, *18*, 155304.

(60) Nikitin, A.; Ogasawara, H.; Mann, D.; Denecke, R.; Zhang, Z.; Dai, H.; Cho, K.; Nilsson, A. *Phys. Rev. Lett.* **2005**, *95*, 225507.

(61) Elias, D. C.; Nair, R. R.; Mohiuddin, T. M. G.; Morozov, S. V.; Blake, P.; Halsall, M. P.; Ferrari, A. C.; Boukhvalov, D. W.; Katsnelson, M. I.; Geim, A. K.; Novoselov, K. S. *Science* **2009**, *323*, 610−613.

(62) Balog, R.; et al. *Nat. Mater.* **2010**, *9*, 315−319.

(63) Haberer, D.; Vyalikh, D. V.; Taioli, S.; Dora, B.; Farjam, M.; Fink, J.; Marchenko, D.; Pichler, T.; Ziegler, K.; Simonucci, S.; Dresselhaus, M. S.; Knupfer, M.; Büchner, B.; Grüneis, A. *Nano Lett.* **2010**, *10*, 3360−3366. PMID: 20695447.

(64) Haberer, D.; et al. *Adv. Mater.* **2011**, *23*, 4497.

(65) Talirz, L.; et al. *ACS Nano* **2017**, *11*, 1380−1388.

(66) Senkovskiy, B. V.; et al. *Advanced Electronic Materials* **2017**, 1600490.

(67) Horcas, I.; Fernandez, R.; Gomez-Rodriguez, J.; Colchero, J.; Gomez-Herrero, J.; Baro, A. *Rev. Sci. Instrum.* **2007**, *78*, 013705.

(68) Her, M.; Beams, R.; Novotny, L. *Phys. Lett. A* **2013**, *377*, 1455−1458.

■ NOTE ADDED AFTER ASAP PUBLICATION

This paper was published on the Web on April 3, 2017, with minor text errors in the first paragraph of the paper. The corrected version was reposted on April 4, 2017.

3.3 Summary

In this Chapter, optical characterization of 7–AGNRs has been initiated with the focus on photoluminescence emission and Raman spectroscopy. This was possible with the development of a technique to transfer GNRs from the growth (gold) to the target (quartz) substrates. The GNRs are aligned, and the degree of their alignment before and after the transfer has been evaluated using polarization-resolved Raman spectroscopy. The results show that the alignment of the GNRs is preserved after the transfer process. Furthermore, the dependence of the Raman intensity (G mode) on the excitation photon energy has been employed to resolve the excitonic features in the GNRs (see section 2.2.5 for further details). The results show that there are three distinct excitonic peaks at 2.1, 2.3, and 2.6 eV (arising from E_{ii} with $i = 1, 2, 3$, respectively).

Our results on PL spectroscopy reveal that the pristine GNRs intrinsically have weak PL emission. The origin of low emission in the GNRs is attributed to the low-lying dark states. Further investigations have shown that the presence of a quenching state, and low–energy excitations raised from the localized states can be alternative reasons for weak emission in GNRs (see chapter 4 and section 2.2.2). We showed that the PL emission could be increased via formation of laser-induced defects in the GNRs. The defects are formed through exposing the GNRs with blue laser under ambient conditions. The modification in the PL is evident by an emerging peak in the emission spectrum centered at 1.8 eV. The same change is observed in the emission of hydrogen-exposed GNRs in ultra-high vacuum environment. This reveals that both hydrogen and laser-driven defects have sp^3 nature.

CHAPTER 4

Extinction spectroscopy of graphene nanoribbons

4.1 Introduction

Extinction spectroscopy gives direct information about the intrinsic electronic structure and photophysical properties. For GNRs, and in general, for nanostructures, extinction is usually identical to absorption [2, 158]. This is the main topic of this chapter in which the extinction spectroscopy of a single layer of aligned 7–AGNRs is presented. Single-atom thickness of the GNR layer implies that a high sensitivity is required. In a collinear geometry, two microscope objectives have been used to focus a white light source from the backside of a quartz substrate on top of which a single layer of aligned GNRs has been transferred. Via lateral displacement of the sample, transmission through areas with and without GNRs is collected, and thus the modulation caused by the GNRs is resolved. The results show that the optical response of the GNRs is dominated by the two excitonic features: a broad high-energy peak at ≈ 2.39 eV, and a low-energy bump at 1.77 eV. The extinction shows strong polarization anisotropy in accordance with the Raman and PL spectra (see also the previous chapter). As explained in chapter 3, exposing the GNRs to blue laser under ambient conditions results in formation of the defects in the lattice of the GNRs. Consequently, the PL emission increases with a distinct peak at 1.8 eV in the emission spectrum. Here we probe the modification induced by the defects in the extinction. The polarization anisotropy of the extinction after induction of the defects in the GNRs is preserved. This is a solid indication of non-destructive effect of the light exposure. The low-energy peak energetically coincides with the PL feature. Upon defect formation, this peak vanishes while the high-energy peak remains almost unmodified. This trend suggests that this peak arises from a quenching state below E_{11} in 7–AGNRs. This peak has not been observed in reflection anisotropy spectroscopy (RAS) for long 7–AGNRs (average length ≈ 20 *nm*) [56]. Recent calculations, however, propose that for short GNRs, there are several low-energy length-dependent excitonic features in the absorption spectrum [71, 73]. Such features arise from low-energy excitations of the localized states at termini of the GNRs (see further details in section 2.2.2). The peak at 1.77 eV in extinction spectra could have the same origin.

We additionally report the investigation on inducing laser-driven defects in GNRs. The defect formation has been investigated with photon energies in the range 2.38−2.95 eV (≈ 420−520 nm). The formation of defects is more efficient for higher photon energies. The rate of the PL growth is higher for the photons with higher energies than lower energies with a factor ≈ 5. Finally, we measure the dependence of the PL emission on the excitation photon energy. This experiment is carried out for the excitation photon energy range of 1.9−3 eV (≈ 410−650 nm) in which no significant spectral shift in the PL feature (at 1.8 eV) was observed.

4.2 Probing the origin of photoluminescence brightening in graphene nanoribbons

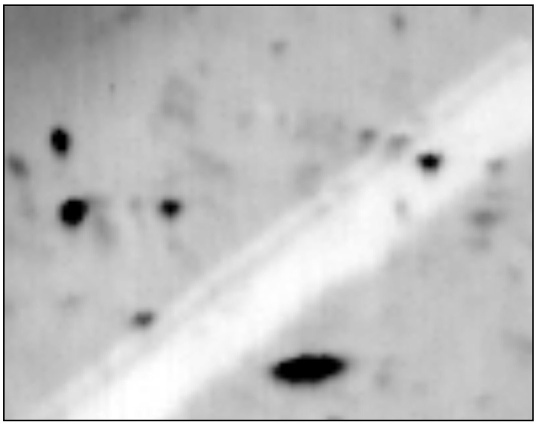

Transmission of light through a single layer of GNRs on top of quartz. The area without GNRs is brighter.

Note: The following section of this chapter is a reprint of a publication with the same title as of the section. The permission is granted by Institute of Physics (IOP) Publishing group. The full citation is: S. K. Alavi, B. V. Senkovskiy, M. Pfeiffer, D. Haberer, F. R. Fischer, A. Grüneis and K. Lindfors, *Probing the origin of photoluminescence brightening in graphene nanoribbons*, 2D Materials, **6**, 035009 (2019) [2].

IOP Publishing 2D Mater. 6 (2019) 035009 https://doi.org/10.1088/2053-1583/ab1116

2D Materials

CrossMark

RECEIVED
14 January 2019

REVISED
25 February 2019

ACCEPTED FOR PUBLICATION
19 March 2019

PUBLISHED
9 April 2019

PAPER

Probing the origin of photoluminescence brightening in graphene nanoribbons

Seyed Khalil Alavi[1,2], Boris V Senkovskiy[3], Markus Pfeiffer[1], Danny Haberer[4], Felix R Fischer[4,5,6], Alexander Grüneis[3] and Klas Lindfors[1]

[1] Department für Chemie, Universität zu Köln, Luxemburger Strasse 116, 50939 Köln, Germany
[2] Institut für Angewandte Physik der Universität Bonn, Wegeler Strasse 8, 53115 Bonn, Germany
[3] II. Physikalisches Institut, Universität zu Köln, Zülpicher Strasse 77, 50937 Köln, Germany
[4] Department of Chemistry, University of California at Berkeley, Tan Hall, Berkeley, CA 94720, United States of America
[5] Materials Sciences Division, Lawrence Berkeley National Laboratory, Berkeley, CA 94720, United States of America
[6] Kavli Energy NanoSciences Institute at the University of California Berkeley and the Lawrence Berkeley National Laboratory, Berkeley, CA 94720, United States of America

E-mail: klas.lindfors@uni-koeln.de

Keywords: graphene nanoribbons, extinction spectroscopy, defects, fluorescence excitation spectroscopy

Supplementary material for this article is available online

Abstract

We measure the absolute absorbance of a single layer of seven atom wide armchair graphene nanoribbons and study the influence of laser-induced defects on the absorption spectrum of the ribbons. We find that the absorption spectrum shows a broad peak at approximately 2.4 eV that is attributed to excitonic transitions and a smaller peak at 1.77 eV. The low-energy peak is diminished when we induce defects in the material. Simultaneously the photoluminescence is significantly enhanced. We thus attribute the 1.77 eV spectral feature in the absorption spectrum to a quenching state, which energetically coincides with the emission. Our results clearly demonstrate the significance of this state in photoluminescence processes in the ribbons. We additionally measure the dependence of the generation of defects on the energy of the incident photons and the photoluminescence excitation spectrum. The photoluminescence excitation efficiency peaks at a higher photon energy than the maximum absorption, hinting at an efficient decay from higher energetic states to the emissive state.

1. Introduction

Patterning graphene into graphene nanoribbons (GNRs) with armchair edges results in the opening of a bandgap due to lateral quantum confinement [1]. Graphene nanoribbons can be synthesized with atomic precision by a bottom–up approach on a large scale [1–4] and even uniformly aligned [5, 6]. The properties of GNRs are strongly influenced by ribbon width and their edge geometry [7–10], which can be used to tailor the material properties. Additional control over the properties of ribbons is enabled by substitutional doping [11, 12]. The possibility to tune the properties of GNRs makes them an attractive active material in electronic devices [13–16]. Even heterojunctions between GNRs of different width have been demonstrated [17]. Very recently topological band engineering of graphene nanoribbons was reported [18, 19].

Semiconducting armchair-edge graphene nanoribbons (AGNRs) have a direct bandgap. Both photo- [20, 21] and electroluminescence [22] in GNRs has been observed. Emitters based on graphene nanostructures are interesting for applications in nano and quantum optics. For example, photon antibunching of the emission from single carbon nanotubes [23] and tunable single-photon emission in the telecommunications wavelength range [24] and an electrically driven carbon nanotube source [25] have recently been demonstrated. Single-photon emission from graphene quantum dots at room temperature was also reported [26]. Graphene nanoribbons may find similar applications in optoelectronics. For example, we have recently observed single quantum emitter characteristics in the emission from GNRs [27]. The properties of GNRs can be engineered by doping and structuring, the materials are stable and can be prepared on wafer scale, and the emitters can potentially be excited electrically. One of the challenges in applying AGNRs is that for the ribbons studied thus far, the intrinsic quantum yield appears to be low. Based on theoretical models, this observation is due to the presence of dark or quenching states degenerate with bright excitonic states [21, 28, 29]. Recently it was shown that seven-atom wide AGNRs (7-AGNRs) can be rendered emissive by exposing them to a blue laser light or by hydrogenation [21]. This induces sp^3 defects in the lattice of GNRs. The induced defects lead to a strong enhancement in photoluminescence (PL). This is presumably due to the lifting of the degeneracy between quenching and emissive states or to the vanishing of the quenching state altogether. At the moment the exact role of the defects on the brightening of the PL from AGNRs is not clear. Here we report the extinction spectrum of a single layer of 7-AGNRs, which allows us to determine the absolute absorbance of the ribbons. We further describe the changes in the extinction spectrum of a single layer of 7-AGNRs following the introduction of defects and highlight the correlation between the spectral modification and enhanced photoluminescence.

2. Results and discussion

2.1. Extinction spectroscopy

In our previous work we showed that the enhancement of PL emission in AGNRs is evidenced by the emerging peak at ≈1.8 eV due to the formation of defects [21]. The defects are induced by exposing the pristine GNRs to a blue laser for several minutes. Herein pristine refers to ribbons that have not been exposed to laser light, although, even these ribbons contain defects due to, e.g. the transfer process and exposure to ambient conditions. We remark that it has been found that GNRs are in general stable under ambient conditions [30]. The enhanced emission is highly polarization sensitive. The polarization anisotropy is the same for pristine and defected ribbons [21], suggesting that the emission from defected GNRs originates from the extended ribbon and not from zero-dimensional emissive states, unlike the case in defected carbon nanotubes [31, 32].

The extinction spectrum allows direct access to the excitonic features in the spectrum and allows us to obtain information about the origin of the PL brightening that can be attributed to defects. To obtain the extinction spectrum, we performed transmission and reflection microspectroscopy. In the experiment, a spectrally broad light source was coupled from the back side of the sample and transmitted light was collected with a microscope objective and imaged to an imaging spectrometer as schematically illustrated in figure 1(a). A polarizer (POL) was used to control the polarization of the light. A quarter-wave plate ($\lambda/4$) oriented at 45° to the polarizer (POL) was used to convert the linear polarization of the transmitted light to circular to eliminate the polarization-dependent transmission of the spectrometer. The layer of GNRs contains holes (labeled 'empty' in figure 1(b)) so that we are able to collect a reflection or transmission spectrum from areas with and without ribbons, which are used as signal and reference, respectively. The holes in the GNR layer are characterized by the absence of characteristic Raman features, which originate from nanoribbons, in these areas.

The spectra of the light transmitted through the ribbon-covered and empty areas are shown in figure S2 in the supplementary material (stacks.iop.org/TDM/6/035009/mmedia). Taking the ratio of the signal and reference spectra, the optical response of the substrate is canceled. Figure 1(b) shows reflection and transmission microscopy images of a typical region of the sample. The upper panel shows that the ribbons (brighter regions) reflect more than the substrate. In fact, the reflected light from these areas is a contribution of both ribbons and substrate reflections (see supplementary material for further details). The transmission micrograph in the lower panel of figure 1(b) shows the expected absorption by the ribbons (dimmer regions).

Figure 1(c) shows typical extinction spectrum for pristine ribbons. Extinction is here defined as $1 - T$, where T is the transmission. The reflectivity of the GNRs in the spectral range of figure 1(c) is approximately two orders of magnitude smaller than the extinction (see figure S3(a) in supplementary material). Therefore, the extinction is mainly due to absorption. Similar to recent reflection anisotropy spectroscopy (RAS) measurements [33], the spectrum shows strong polarization anisotropy confirming the GNRs as the origin of the observed features. The extinction shown in figure 1(c) is maximized for light polarized along the ribbons (red) and reduced when the polarization is turned by 45 degrees (orange) or 90 degrees (blue).

The absolute absorbance of 7-AGNRs can be extracted from the present results. From scanning tunneling microscopy (STM) measurements on similar samples than those used in the present study, we estimate a 1 nm lateral distance between the ribbons, resulting in a coverage of the layer of approximately 0.5 [34]. Thus the absolute measured absorption at the peak marked B in figure 1(c) is approximately 6.8%. This value is in excellent agreement with the DFT calculated absorbance of about 8% (for coverage of 0.8) [33]. In fact the actual coverage of the ribbons is at most 50% due to loss of ribbons during the transfer process. However, we estimate these losses to be low as the bubbling transfer method is commonly used to transfer large areas of graphene with good quality [35, 36]. The measured peak absorbance varies between 6.0% and 7.6% for different points on the sample in our experiments indicating that the density of GNRs fluctuates from point to point. The extinction spectrum consists of two peaks marked as A and B in figure 1(c). The peaks are well fitted with Lorentz and Voigt profiles for peaks A and B, respectively. The spectral positions

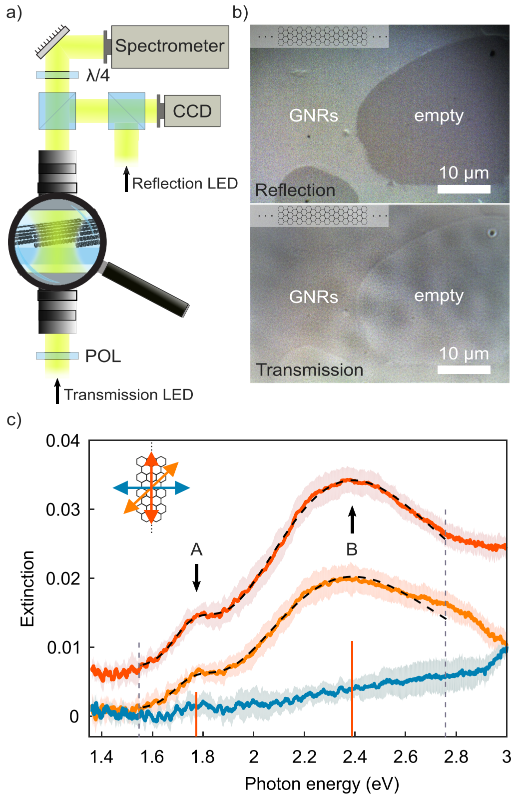

Figure 1. (a) Schematic representation of the optical setup used to measure the extinction of single layer of aligned AGNRs. (b) Optical micrographs of a single layer of 7-AGNRs on quartz substrate. In the upper panel the GNR layer is visible as brighter areas due to increased reflection from ribbons with respect to the substrate. In the lower panel the ribbon covered areas appear dim due to absorption. (c) Extinction spectra of pristine 7-AGNRs. Incident light is linearly polarized with an angle of zero (red), 45° (orange) and 90° (blue) with respect to the ribbon axis. The spectra are fitted with a Lorentz (peak A) and Voigt (peak B) profile for the case of zero and 45° angle with respect to the ribbon for the spectral range indicated with the dashed lines. The fits are shown with black dashed lines. Error bars are indicated as semi-transparent filled areas.

obtained from the fits for the two peaks are 1.77 eV and 2.39 eV for A and B, respectively. The spectral feature at 2.39 eV is consistent with RAS data and DFT calculations [33]. In this context the peak was assigned to a sum of two broadened excitonic resonances located at 2.1 eV and 2.3 eV. The spectral position of peak B also agrees with recent results from investigations on multilayers [37] and theoretical studies on single GNRs [22, 38].

The peak labeled A in figure 1(c) has not been observed earlier. We speculate that in recent measurements on unaligned multilayers (samples with approximately 25 layers) [37], the visibility of this peak may have been reduced due to inhomogeneous broadening making its observation challenging. Peak A coincides with the spectral position of the emission peak (see figure 2(c)). At a first glance, this would appear to coincide with the origin of the PL emission in GNRs. However, we note that the spectra in figure 1(c) were obtained for the weakly emissive pristine ribbons. As an alternative explanation for peak A, theoretical studies have previously predicted the presence of quenching states degenerate with the emissive state in AGNRs [28, 29]. Finally, recent experimental and theoretical studies on single finite GNRs connected to an STM tip at one end of the ribbon have found optically bright transitions in the spectral range 1.1–2.0 eV at 4.5 K temperature [22]. In [22] the origin of the spectral features was identified as transitions from bulk states to localized edge states. It is unlikely that these states are the origin of peak A, as they can already be observed for a weakly emitting sample. Peak A has similar polarization dependence as peak B confirming its origin in the GNRs. The gradual slope in the extinction spectrum for perpendicular polarization is similar to absorption spectra of a graphene sheet and can be attributed to the edge-independent absorption of ribbons.

To unravel the connection between peak A in the extinction spectra and the photoluminescence we next measured extinction spectra before and after introduction of defects. The main result is shown in figure 2(a) (see also figure 2(c)). As indicated in the figure,

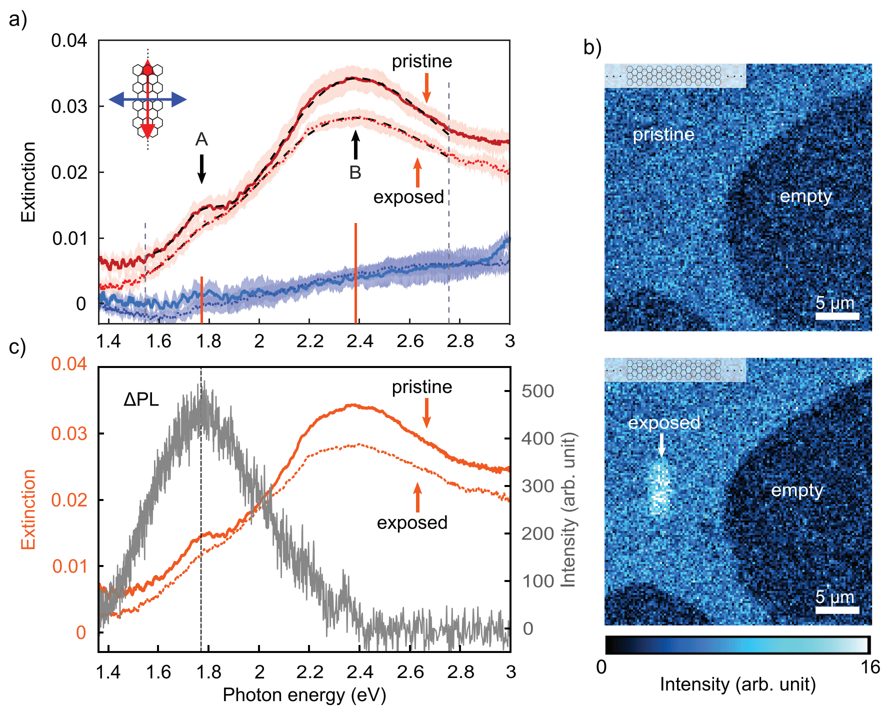

Figure 2. (a) Extinction spectra of AGNRs for both light polarized along (red) and perpendicular (blue) to the ribbons. The spectra before inducing defects are shown with solid lines. The spectra after defect induction are presented with dotted lines. Error bars are indicated as semi-transparent filled areas. (b) Photoluminescence scan of the area from which the spectra in (a) were measured. The upper panel is recorded before defect induction. In the lower panel a small region has been rendered emissive by exposing it with blue light. The dark regions correspond to holes in the film of nanoribbons. (c) Change in PL (ΔPL) when defects are introduced as a function of photon energy and the extinction spectrum before and after inducing defects.

we compare spectra for pristine and defected ribbons (solid and dotted lines, respectively) for both polarization along and perpendicular to the ribbons (red and blue color, respectively). The defects were locally induced in the ribbons by exposing the sample to 470 nm wavelength (≈2.64 eV photon energy) tightly focused laser light (spot size ≈ 1 μm). Figure 2(b) shows photoluminescence scans before and after inducing defects. The region of defected GNRs can be seen in the lower micrograph as an area of brigher intensity. Turning to the changes in the extinction spectra (figure 2(a)), peak B remains at the same energetic position with a slightly reduced peak height but with a broader width. In comparison, the area for peak A is reduced by more than a factor of two and is hardly visible after the induction of defects. Simultaneously the fluorescence signal is greatly increased (see figure 2(b)). The extinction spectra for perpendicularly polarized light remains almost the same. Figure 2(c) summarizes the observation. Here the increase in PL when defects are introduced is shown together with the extinction spectra before and after inducing defects. The center of PL peak is very close to the location of peak A.

Our observation that when the fluorescence is boosted by introducing defects the spectral feature in the extinction spectrum at 1.77 eV is reduced, suggests that this spectral peak originates in an exciton quencher and is not directly the source of the emission. This is analogous to carbon nanotubes where the quantum yield is strongly affected by the ratio of radiative and non-radiative decay channels due to defect and end-site states [31, 39–42]. Brightening of carbon nanotubes has been demonstrated by changing the ratio of quenching state to bright exciton gateway. Reacting carbon nanotubes with oxygen [31], aryl diazonium salts [32], or 4-iodoaniline [42], or exposing them to intensive laser pulses [43] to induce zero-dimensional emissive defects are examples to enhance their PL emission. Miyauchi *et al* [31] have attributed the PL enhancement in SWCNTs to the increase of emissive localized defect states which capture the mobile excitons in SWCNTs. This counteracts the influence of quenching sites along the tube. However, in our case the situation is different as we observe a clear reduction of the quenching state (peak A) as defects are induced. Our experiments do not allow us to determine the nature of the quenching state. Theoretical studies have previously predicted the presence of dark excitonic states degenerate with the emissive state in AGNRs [28, 29]. This would result in low photoluminescence efficiency. However, the transition responsible for peak A cannot be a purely dark state as a dark transition would not couple to the incident light. Our experimental results suggest that either the oscillator strength of the dark exciton is non-zero and the transition is not completely dark or that there are other states present responsible for the quenching of the emission. The observed feature at 1.77 eV may be a signature of such states.

2.2. Defect generation rate and photoluminescence excitation spectrum

After characterizing the influence of laser-induced defects on the extinction spectrum, we next maximize the rate of inducing defects and the PL signal. We first measure the dependence of the rate of increase of fluorescence as a function of the used photon energy. The fluorescence signal increases exponentially as a function of time until it saturates (see supplementary material figure S4). We extract the rate of fluorescence increase from measured data by fitting them with an exponential function (see details in supplementary material). Figure 3(a) shows the extracted rate constant as a function of photon energy. The rate increases as a function of photon energy by a factor of approximately five for the energy range of figure 3(a). The inset shows the recorded evolution of fluorescence signal as a function of time. Here each trace has been normalized to the corresponding saturation value.

The observed dependence on the photon energy is similar to what has been previously observed in light-induced defect-generation in aromatic molecules [44, 45]. In these reports, different wavelength regimes resulted in the generation of different photoproducts. Interestingly, the defect generation process does not depend strongly on absorption (see extinction spectrum in figure 1(c)). This has already been observed for defect formation in single and multilayer graphene [46] and similar effects have also been reported for aromatic molecules [44]. However, the PL and exctinction spectra and the emission increase at saturation are not altered when the energy of the photons used to generate the defects is varied. This indicates that the defects modify the optoelectronic properties of the GNRs in a well-defined manner.

To gain additional insight into how the used photon energy influences the fluorescence we measured the PL excitation spectrum. We first induced defects using 2.81 eV energy photons until the increase in fluorescence had saturated. Next we measured PL spectra for an excitation energy range of 1.9 eV to 3.0 eV (see spectra in supplementary material). The measured PL spectra for different excitation photon energies do not vary noticeably. This is different from fluorescence emission in graphene oxide which shows a large shift (approximately 0.26 eV) for an excitation range of 1.90 eV to 3.54 eV [47]. In our measurements we did not observe such a large shift (see supplementary material figure S6). The spectra were fitted with a Gaussian function at 1.75 eV (spectral location of fluorescence peak). The strength of the fitted peak as a function of the used photon energy is shown in figure 3(b). We observe a significant variation with a broad peak centered around 2.68 eV (peak C). The peak position was determined using a Gaussian fit. This is blue shifted from the resonance in the extinction spectrum at 2.39 eV (peak B). We note that the photoluminescence excitation spectrum does not directly reflect the absorption spectrum but rather the efficiency of populating the emissive state by decay process from the higher lying states. We remark that we have earlier found an excitonic transition at 2.6 eV [21], which is close to the observed peak C. Our observation suggests efficient coupling from higher energetic states to the emissive state. The small increase in the strength of PL for photon energies lower that 2 eV is an artifact due to the contribution of higher order Raman modes to the collected emission (shaded region).

2.3. Discussion

Our key observation is that photochemically generated defects significantly modify the transitions of 7-AGNRs as evidenced both by their extinction and PL. Based on our results and earlier studies, we propose that the defects, whose effect we observe, are due to photo-oxidation. Previously photo-oxidation of terrylene molecules due to their reaction with singlet oxygen was shown to result in significant modification of the emission properties of the molecules [44]. Here both spectral shifts and a ceasing of emission was observed. Singlet oxygen formation due to a self-sensitization process has been observed for photoexcited terrylene [44] and graphene quantum dots [48]. A similar process could take place between the photo-excited 7-AGNR and oxygen. Our observation of an increasing rate of defect generation for increasing energy of incident photons is characteristic for such reactions [42]. Finally, we have verified that the defect-induced increase in emission takes place much slower in vacuum than under ambient conditions (see supplementary material figure S5).

3. Conclusions

In summary, we have measured the extinction spectrum of a single layer of 7-AGNRs with a surface coverage of 50% and observed the modification of the extinction spectrum and photoluminescence properties when defects are introduced into the material under ambient conditions. We observe a broad peak centered at 2.39 eV, which we attribute to excitons, in addition to a peak at 1.77 eV. The lower energy peak can be attributed to a quenching state that results in low PL quantum efficiency for 7-AGNRs. For areas where we intentionally introduce defects using a photochemical process we observe a strong increase in the PL and simultaneously a decrease in the low-energy peak observed in the extinction spectrum.

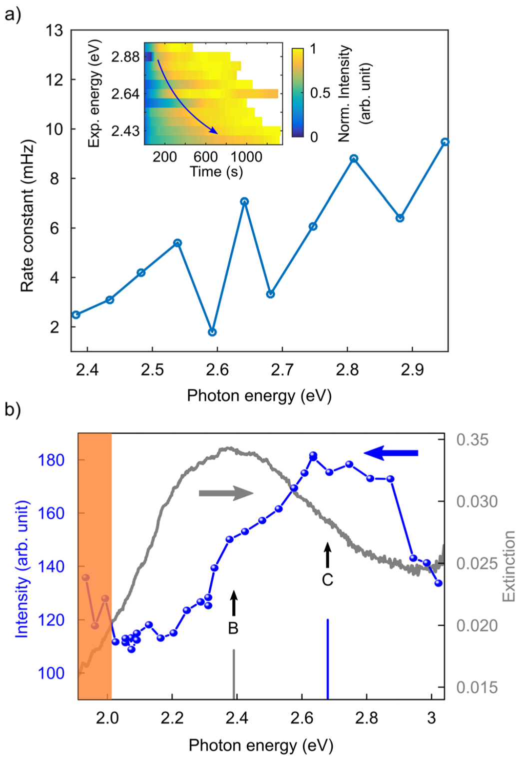

Figure 3. (a) Rate constant of fluorescence increase as a function of photon energy. Inset shows evolution of fluorescence intensity during the exposure. (b) PL emission strength as a function of excitation photon energy (blue) and extinction spectrum of sample (gray).

This indicates that the 1.77 eV photon energy spectral feature is related to a quenching transition that inhibits emission. Finally, PL excitation spectroscopy shows that the emission is not maximized at the wavelength corresponding to the highest absorption but instead at higher photon energy. This observation suggests that the emissive state is more efficiently populated from a higher lying state. We have earlier observed an excitonic feature close to the photon energy that results in the strongest emission [21].

Our results illustrate the importance of chemical modification to engineer the properties of GNRs. Recently it has been shown that the presence of structural defects substantially increase the mechanical flexibility of GNRs, but barely affect their electrical conductance [49], and that structural defects can be used to define heterostructures in GNRs [50]. More detailed investigations into the influence of defects on GNRs is of paramount importance. Theoretical studies on the influence of different chemical groups on GNRs would be very useful to guide experimental efforts. Time-resolved spectroscopy would provide a more detailed picture of how the different states are populated and their dynamics as has been found for SWCNTs [31]. Such efforts may lead to novel approaches to engineer GNRs for optoelectronic applications.

4. Methods

4.1. Sample fabrication

Surface polymerization of 10,10’-dibromo-9,9’-bianthracene (DBBA) molecules on Au(788) surface was used to synthesize aligned 7-AGNRs [5, 51]. First three cycles of Ar^+ sputtering (800 V) and annealing at 500 °C was used to clean the substrate. A home-built evaporator was used to evaporate DBBA molecules from a quartz crucible. The temperature of the evaporation process was controlled using a thermocouple attached to the molecule reservoir. Approximately 4 Å of DBBA molecules were deposited on the gold substrate, which was kept at room temperature. The deposition rate and thickness was controlled using a quartz microbalance applying the density and Z-factor of graphite. The surface polymerization was performed by first annealing the sample at 200 °C for 30 min followed by a second annealing at 380 °C for 15 min. The two annealing steps induce debromization and cyclodehydrogeneration, respectively.

A bubbling transfer technique based on electrochemical delamination process was employed to transfer the GNRs from the Au(788) to a quartz substrate [21]. A layer of poly(methyl methacrylate) (PMMA) was coated on the 7-AGNRs/Au(788) sample. The PMMA-coated sample was then placed in an electrochemical cell with an NaOH aqueous solution ($1\,\mathrm{mol\,l^{-1}}$). A reference mark on the Au(788) crystal shows the direction of (111) terraces. At the negatively charged cathode, the PMMA/7-AGNRs layer was detached from the Au(788) substrate by the emerging H_2 gas bubbles due to the reduction of water. The floating PMMA/7-AGNRs layer was then cleaned in distilled water and placed onto the substrate. To remove PMMA and clean the sample surface, we employed 1,2-dichloroethane (48h) and methanol (1h), followed by N_2 blowing. The sample was characterized by polarized Raman measurements (532nm laser) [21] after the synthesis on Au(788) and after the transfer on quartz substrate. In the Raman spectra we observe only characteristic features of GNRs and no spectral signature from PMMA. Figure S1 in the supplementary material presents exemplary polarization-resolved Raman spectra of the samples.

4.2. Optical measurements

All experiments were performed at room temperature. Photoluminescence measurements were carried out using an in-house developed confocal microscope. Laser light from a supercontinuum laser was focused down to a diameter of approximately one micron using a microscope objective with 0.8 numerical aperture (NA). The polarization of the incident light was controlled using an achromatic half-wave plate. In the detection path a quarter-wave plate was oriented at 45° with respect to an analyzer to mix the polarization states and provide polarization insensitive detection. All the polarization and power dependencies of the setup were compensated. In all measurements the incident power was kept below 150 μW.

In the extinction measurements a fiber-coupled spectrally broad LED source was first collimated and then focused weakly using a 0.25 NA objective on the back side of the sample in the same microscope as used for the PL experiments. Transmitted light was then collected by a 0.8 NA objective. Incident light was polarized with a Glan–Taylor polarizer. The polarization was controlled in the detection path similarly to the PL measurements. The sample could be positioned with nanometer accuracy using a piezo stage to record the light transmitted through ribbons and a hole as signal and reference, respectively. The reflection measurements were performed similarly.

A supercontinuum laser was used to measure the energy dependence of defect formation in the GNRs and the PL excitation spectrum. A variable bandpass filter was used to select the excitation photon energy. The laser power was kept below 50 μW and the light was focused with a 0.8 NA objective to a diffraction limited spot. For each photon energy a fresh region was exposed. The spectrally integrated intensity as a function of time was fitted with an exponential curve to obtain the rate constant.

For the PL excitation spectrum light from a supercontinuum laser was used. To narrow down the spectral bandwidth we used a tunable grating filter in the excitation. Several sharp-edge long pass filters were used to cut out the laser light in the emission. The spectra were normalized to the incident power and corrected for the setup wavelength dependence. In all PL experiments the polarization of the incident light was along the ribbons and the same polarization insensitive detection setup as in the extinction spectroscopy was used.

Acknowledgments

This work has been supported by the University of Cologne through the Institutional Strategy of the University of Cologne within the German Excellence Initiative (QM^2). SKA thanks the Bonn Cologne Graduate School of Physics and Astronomy and DAAD for financial support. AG and BS acknowledge the ERC grant No. 648589 'SUPER-2D'. MP was supported by a UoC postdoc grant. Research is supported by the U.S. Department of Energy, Office of Science, Basic Energy Sciences, under Award # DE-SC0010409 (design, synthesis, and characterization of molecular precursors)

ORCID iDs

Boris V Senkovskiy https://orcid.org/0000-0003-1443-6780
Alexander Grüneis https://orcid.org/0000-0003-2448-6060
Klas Lindfors https://orcid.org/0000-0002-6482-5605

References

[1] Talirz L, Ruffieux P and Fasel R 2016 *Adv. Mater.* **28** 6222
[2] Grill L, Dyer M, Lafferentz L, Persson M, Peters M V and Hecht S 2007 *Nat. Nanotechnol.* **2** 687
[3] Cai J *et al* 2010 *Nature* **466** 470
[4] Ruffieux P *et al* 2016 *Nature* **531** 489
[5] Linden S *et al* 2012 *Phys. Rev. Lett.* **108** 216801
[6] Ruffieux P *et al* 2012 *ACS Nano* **6** 6930
[7] Son Y W, Cohen M L and Louie S G 2006 *Phys. Rev. Lett.* **97** 216803
[8] Son Y W, Cohen M L and Louie S G 2006 *Nature* **444** 347
[9] Yang L, Park C H, Son Y W, Cohen M L and Louie S G 2007 *Phys. Rev. Lett.* **99** 186801
[10] Wang W X, Zhou M, Li X, Li S Y, Wu X, Duan W and He L 2016 *Phys. Rev.* B **93** 241403
[11] Cloke R R, Marangoni T, Nguyen G D, Joshi T, Rizzo D J, Bronner C, Cao T, Louie S G, Crommie M F and Fischer F R 2015 *J. Am. Chem. Soc.* **137** 8872
[12] Kawai S, Saito S, Osumi S, Yamaguchi S, Foster A S, Spijker P and Meyer E 2015 *Nat. Commun.* **6** 8098
[13] Chen Z, Lin Y M, Rooks M J and Avouris P 2007 *Physica* E **40** 228
[14] Wang X, Ouyang Y, Li X, Wang H, Guo J and Dai H 2008 *Phys. Rev. Lett.* **100** 206803
[15] Kim W Y and Kim K S 2008 *Nat. Nanotechnol.* **3** 408

[16] Bennett B P, Pedramrazi Z, Madani A, Chen Y C, De Oteyza D G, Chen C, Fischer F R, Crommie M F and Bokor J 2013 *Appl. Phys. Lett.* **103** 253114
[17] Chen Y C, Cao T, Chen C, Pedramrazi Z, Haberer D, de Oteyza D G, Fischer F R, Louie S G and Crommie M F 2015 *Nat. Nanotechnol.* **10** 156
[18] Gröning O *et al* 2018 *Nature* **560** 209
[19] Rizzo D J, Veber G, Cao T, Bronner C, Chen T, Zhao F, Rodriguez H, Louie S G, Crommie M F and Fischer F R 2018 *Nature* **560** 204
[20] Chernov A I, Fedotov P V, Talyzin A V, Suarez Lopez I, Anoshkin I V, Nasibulin A G, Kauppinen E I and Obraztsova E D 2013 *ACS Nano* **7** 6346
[21] Senkovskiy B V *et al* 2017 *Nano Lett.* **17** 4029
[22] Chong M C, Afshar-Imani N, Scheurer F, Cardoso C, Ferretti A, Prezzi D and Schull G 2018 *Nano Lett.* **18** 175
[23] Högele A, Galland C, Winger M and Imamoğlu A 2008 *Phys. Rev. Lett.* **100** 217401
[24] He X *et al* 2017 *Nat. Photon.* **11** 577
[25] Khasminskaya S *et al* 2016 *Nat. Photon.* **10** 727
[26] Zhao S *et al* 2018 *Nat. Commun.* **9** 3470
[27] Pfeiffer M, Senkovskiy B V, Haberer D, Fischer F R, Yang F, Meerholz K, Ando Y, Grüneis A and Lindfors K 2018 *Nano Lett.* **18** 7038
[28] Yang L, Cohen M L and Louie S G 2007 *Nano Lett.* **7** 3112
[29] Prezzi D, Varsano D, Ruini A, Marini A and Molinari E 2008 *Phys. Rev.* B **77** 041404
[30] Ma C, Xiao Z, Puretzky A A, Baddorf A P, Lu W, Hong K, Bernholc J and Li A P 2018 *Phys. Rev. Mater.* **2** 014006
[31] Miyauchi Y, Iwamura M, Mouri S, Kawazoe T, Ohtsu M and Matsuda K 2013 *Nat. Photon.* **7** 715
[32] Piao Y, Meany B, Powell L R, Valley N, Kwon H, Schatz G C and Wang Y 2013 *Nat. Chem.* **5** 840
[33] Denk R *et al* 2014 *Nat. Commun.* **5** 4253
[34] Passi V, Gahoi A, Senkovskiy B V, Haberer D, Fischer F R, Grüneis A and Lemme M C 2018 *ACS Appl. Mater. Interfaces* **10** 9900
[35] Gao L *et al* 2012 *Nat. Commun.* **3** 699
[36] Wang Y, Zheng Y, Xu X, Dubuisson E, Bao Q, Lu J and Loh K P 2011 *ACS Nano* **5** 9927
[37] Chen Z *et al* 2017 *J. Am. Chem. Soc.* **139** 3635
[38] Deilmann T and Rohlfing M 2017 *Nano Lett.* **17** 6833
[39] Cognet L, Tsyboulski D A, Rocha J D R, Doyle C D, Tour J M and Weisman R B 2007 *Science* **316** 1465
[40] Hertel T, Himmelein S, Ackermann T, Stich D and Croche J 2010 *ACS Nano* **4** 7161
[41] Harrah D M and Swan A K 2011 *ACS Nano* **5** 647
[42] Wu X, Kim M, Kwon H and Wang Y 2018 *Angew. Chem. Int. Ed.* **57** 648
[43] Harutyunyan H, Gokus T, Green A A, Hersam M C, Allegrini M and Hartschuh A 2009 *Nano Lett.* **9** 2010
[44] Christ T, Kulzer F, Bordat P and Basche T 2001 *Angew. Chem. Int. Ed.* **40** 4192
[45] Afshari E, Brauer H D and Schmidt R 1992 *Photochem. Photobiol.* A **63** 319
[46] Imamura G and Saiki K 2014 *J. Phys. Chem.* C **118** 11842
[47] Imamura G and Saiki K 2012 *Sci. Rep.* **2** 792
[48] Ge J *et al* 2014 *Nat. Commun.* **5** 4596
[49] Koch M, Li Z, Nacci C, Kumagai T, Franco I and Grill L 2018 *Phys. Rev. Lett.* **121** 047701
[50] Blankenburg S, Cai J, Ruffieux P, Jaafar R, Passerone D, Feng X, Müllen K, Fasel R and Pignedoli C A 2012 *ACS Nano* **6** 2020
[51] Senkovskiy B V, Usachov D Y, Fedorov A V, Haberer D, Ehlen N, Fischer F R and Grüneis A 2018 *2D Mater.* **5** 035007

4.3 Summary

In this chapter, the measurement of the extinction spectrum for a single layer of aligned 7–AGNRs is reported. The extinction spectrum shows strong polarization dependence in agreement with anisotropy in the GNRs structure and alignment: The extinction is highest for light polarized along the GNRs. The spectrum consists of two excitonic features at 1.77 and 2.39 eV. The lateral distance between the GNRs is in the order of 1 nm, resulting in a coverage of 50%. Taking this into account, for full surface coverage, the absolute absorbance of the GNRs is 6.8% at 2.39 eV. This is 3 times higher than the graphene absorbance in the visible spectral range. This high absorbance for only one-atom-thick layer is interesting for photodetection applications (see chapter 5).

The impact of defect formation in the extinction of the GNRs has been probed. The results show that the higher-energy excitonic feature remains almost unmodified. Upon formation of defects, the low-energy peak vanishes and simultaneously the PL intensity increases. The inverse relation between the low-energy peak in the extinction and the feature in PL emission, and the fact that both spectral peaks energetically match (in the extinction at 1.77 eV and in the emission at 1.8 eV), strongly suggest that the peak in extinction spectrum arises from a quenching state(s). This state contributes to hinder the PL emission in the pristine GNRs. The optical experiments, i.e. extinction, PL, and Raman spectroscopies are not capable to explain further details about the microscopic nature of defects, and it is a subject for further investigations. We additionally evaluated the light-driven defects formation in vacuum conditions. The results show negligible change in the PL emission. This implies the oxygen-related nature of the defects. The present results shed light towards further theoretical and experimental investigations of such systems.

CHAPTER 5

Demonstration of nanoscale photodetectors using atomically precise graphene nanoribbons

5.1 Introduction

In this chapter, the first demonstration of nanoscale photodetectors using atomically precise GNRs is presented. The photodetectors consist of a single layer of aligned 7–AGNRs between source and drain electrodes. The channel length in typical devices are $\approx$ 100 nm, noticeably larger than the individual GNRs (on average $\approx$ 30 nm long). This implies that the electrical transport is dominated by charge hopping between the GNRs. The photodetection performance of the devices has been explored in a confocal microscopy setup using a supercontinuum light source to cover the visible spectral range.

Upon illumination, absorption of incident photons in the GNRs results in the generation of electron-hole pairs. These photo-generated carriers increase the conductivity, and thus modify the current transport in the GNRs. Detection of these changes is the main principle of the GNRs-based photodetectors. The photodetection has been studied for low bias voltages (typically V_B = 2 V) in which the devices exhibit remarkably low dark current (tens of pA). This is in contrast to the typical graphene-based photodetectors. The alignment of GNRs results in polarization anisotropy of the absorption [2] (see chapter 4). This consequently facilitates inherent polarization selectivity in the photodetection of the devices. Apart from the photoconductive mechanism, we observe a weak photothermal effect in the total response of the photodetectors. This effect, which is polarization insensitive, originates from absorption of the light in the electrodes. The contributions of these two effects have been separated via polarization-sensitive measurements with two types of the devices, i.e. one type with the GNRs along the electrodes and the other one with GNRs perpendicular to the electrodes. Results show that the photoconductivity is the dominant mechanism of the photodetection. This is supported by position-resolved and wavelength-dependent measurements of the photodetectors.

5.2 Photodetection using atomically precise graphene nanoribbons

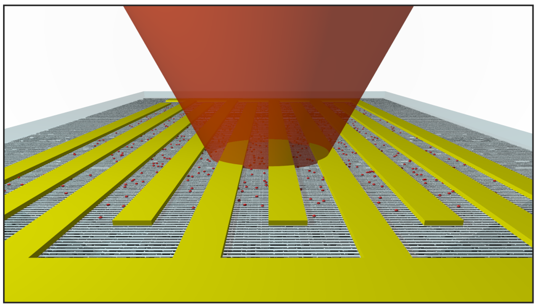

Schematic view of the first GNR-based photodetector with interdigitated structure.

Note: The following section of this chapter is a manuscript with the same title as of the section. After submission of this thesis, the manuscript has been published in ASC Applied Nano Materials. The permission is granted by the American Chemical Society (ACS). The full citation is: S. K. Alavi, B. V. Senkovskiy, D. Hertel, D. Haberer, Y. Ando, K. Meerholz, F. R. Fischer, A. Grüneis, and K. Lindfors, *Photodetection using atomically precise graphene nanoribbons*, ACS Applied Nano Materials, **3**, 8343–8351 (2020). (https://doi.org/10.1021/acsanm.0c01549)

Photodetection using atomically precise graphene nanoribbons

Seyed Khalil Alavi,[†,‡] Boris V. Senkovskiy,[¶] Dirk Hertel,[†] Danny Haberer,[§] Yoichi Ando,[¶] Klaus Meerholz,[†] Felix R. Fischer,[§,∥,⊥] Alexander Grüneis,[¶] and Klas Lindfors[*,†]

†*Department für Chemie, Universität zu Köln, Luxemburger Strasse 116, 50939 Köln, Germany*

‡*Institut für Angewandte Physik der Universität Bonn, Wegeler Strasse 8, 53115 Bonn, Germany*

¶*II. Physikalisches Institut, Universität zu Köln, Zülpicher Strasse 77, 50937 Köln, Germany*

§*Department of Chemistry, University of California at Berkeley, Tan Hall, Berkeley, CA 94720, USA*

∥*Materials Sciences Division, Lawrence Berkeley National Laboratory, Berkeley, CA 94720, USA*

⊥*Kavli Energy NanoSciences Institute at the University of California Berkeley and the Lawrence Berkeley National Laboratory, Berkeley, California 94720, USA*

E-mail: klas.lindfors@uni-koeln.de

Abstract

In the search for high sensitivity, low noise, and high bandwidth photodetectors, novel materials are a key ingredient. One- and two-dimensional materials are of particular interest in this area due to their extraordinary properties such as ballistic transport. Here we demonstrate nanoscale photoconductive photodetectors using aligned atomically precise seven-atom wide armchair-edge graphene nanoribbons. The detector responsivity is 0.035 $\mathrm{mAW^{-1}}$ at a bias voltage of 2 V. The dark current is below 30 pA for a bias voltage of 1.5 V, which is orders of magnitude lower than that of typical graphene photodetectors. The possibility to align the nanoribbons and to tune their optical and electronic properties by choice of ribbon width and edge structure, enables nanoscale polarization-resolving photodetectors optimized for specific spectral ranges. Graphene nanoribbons with identical electronic and optical properties can be prepared on large scale using bottom up synthesis, making them a highly interesting material for electronics and optoelectronics.

Keywords

Graphene nanoribbons, photodetection, photoconduction, charge transport

High performance photodetectors are essential components in many areas of science and technology such as optical communications, integrated optics, imaging and sensing, and quantum technology. Graphene and other two-dimensional (2D) materials have attracted much interest in the quest for future optoelectronic devices. In photodetectors based on 2D materials, optical detection is accomplished using different mechanisms.[1] For example, in graphene-based detectors, photoconductance (PC),[2,3] photothermoelectric (PTE),[4,5] photogating (PG),[6] and bolometric[7] effects have been recruited in the detection of light. Detectors based on PC and PG[8,9] as well as PTE[10] effects have also been reported for devices featuring $\mathrm{MoS_2}$ as active material. Although the development of graphene-based photodetectors has been rapid and impressive, graphene has a vanishing bandgap and its absorption spectrum cannot be engineered for specific applications. The absence of a bandgap limits the merit of graphene based photoconductive photodetectors due to large dark current, which leads to a worse on/off ratio and increases energy consumption. An interesting class of materials addressing these restrictions is atomically precise graphene nanoribbons (GNRs).

Graphene nanoribbons posses well–defined and width–dependent electrical and optical properties and can thus be tuned for specific applications.[11,12] Graphene nanoribbons can be prepared using bottom–up synthesis through polymerization of molecular precursors providing substantial control over the properties of the GNRs.[13–18] By suitable choice of the precursor, the resulting GNRs can be tuned from small to wide bandgap semiconductors.[19–21] This enables tailoring the absorption spectrum to match a specific spectral range. Semiconducting GNRs can further be doped by suitable choice of the precursor.[22] Aligned GNRs with uniform properties can be prepared on wafer scale in contrast to for example carbon nanotubes (CNTs). The alignment results in a dependence of light absorption on the polarization direction of the incident light, which is useful for polarimetric imaging.[23] The possibility to synthesize aligned GNRs with identical properties on large areas is essential for scalability or for preparing devices such as detector arrays. Graphene nanoribbons are thus potentially an ideal material for applications in electronics and optoelectronics.

Nanoscale photodetectors are a particularly interesting area of application for semiconducting GNRs. For example, the possibility to engineer the properties of GNRs allows optimizing the active material for different wavelength regimes and applications. Additionally, in comparison to for example graphene,[1–6,6,24–27] semiconducting GNRs are expected to have a much smaller dark current due to their semiconducting properties and a larger absorption efficiency.[18,28] The few so far demonstrated photodetectors based on GNRs have made use of ribbons etched out of a continuous layer of graphene with widths of tens of nanometers,[29,30] or of a few nanometer wide ribbons obtained by selectively unzipping single-walled carbon nanotubes (SWCNT).[31] In these cases, the properties of the structures remain almost identical to that of an extended layer of graphene and the structure of the edge of the ribbon is not controlled. The edges, however, are critical for transport processes. Thus the potential of atomically precisely controlled GNRs has not yet been realized. Here we demonstrate the first photodetector based on aligned GNRs and observe high responsivity and low dark current over a large range of the visible spectral range. The response of the photodetector is polarization sensitive due to the alignment of the ribbons and the electrode structure.

The GNR photodetector is based on observing the change in conductance in a layer of aligned GNRs upon absorption of light. The detector consists of a single layer of aligned 7-atom wide armchair-edge graphene nanoribbons (7–AGNRs) on a glass substrate, on top of which a set of interdigitated finger electrodes are fabricated. The gap between the source and drain electrodes has been designed to be 100 nm. As metal we use a layer of titanium for adhesion, followed by a thicker layer of gold. Full details about the sample preparation are given in the Methods Section. Detectors prepared on silicon substrates using a different electrode pattern are presented in the Supporting Information.

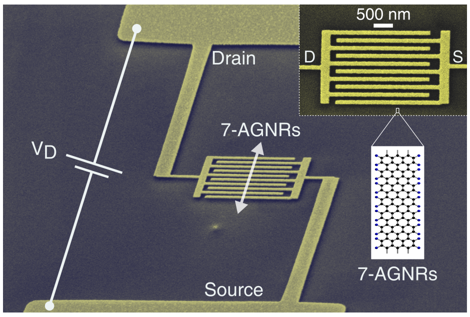

Figure 1: The false colored scanning electron micrograph shows the interdigitated electrodes on top of a layer of 7–AGNRs. The GNRs are aligned parallel to the gap connecting the electrodes. The inset shows a higher magnification electron micrograph of the electrodes. The arrow and schematic show the orientation of the GNRs.

Figure 1 shows electron micrographs of a typical structure. The gap in the realized device very well matches the design value of 100 nm. The average length of the 7–AGNRs is approximately 30 nm as determined from scanning tunneling microscopy on similar samples as those used in this study.[32] Charge transport between source and drain electrodes thus includes hopping between GNRs. Reducing the gap between the electrodes to the length of the GNRs could thus significantly improve the efficiency with which charges are transported to the electrodes.[33,34] In addition to the devices based on interdigitated finger electrodes, we have also realized structures consisting of a point-like gap between two electrodes. In these structures we have reached a gap width of 100 nm. Data on these structures is presented in Supporting Information Fig. S1.

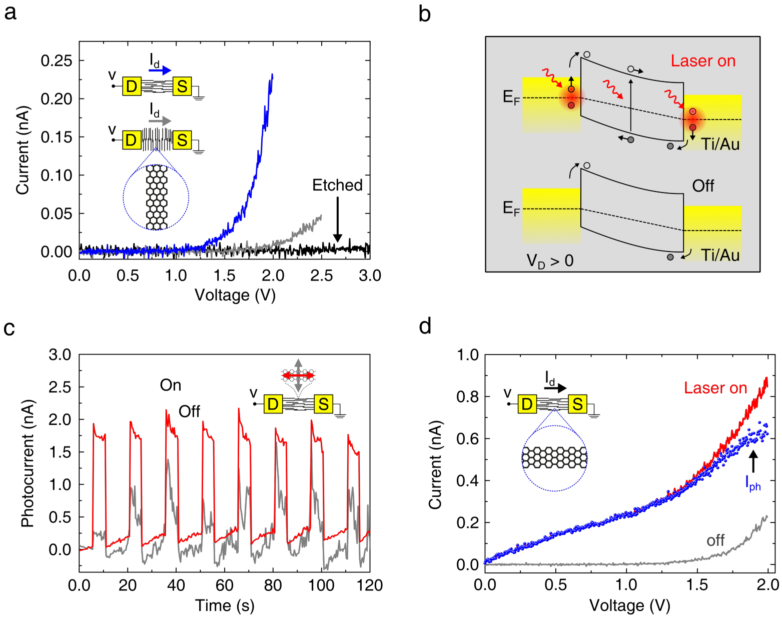

Figure 2: a) The current–voltage curves for devices with GNRs across (blue) and perpendicular to (gray) the gap between the source and drain electrodes are nonlinear above a threshold voltage. After etching the GNRs away, no charge transport is observed (black). b) Energy band diagram in device under bias. The photogenerated carriers are transported to the electrodes under presence of bias voltage. c) The photocurrent is polarization dependent. The current is larger for light polarized along (red) than perpendicular (gray) to GNRs due to the higher absorption. The laser light was modulated and kept on for 5 s and turned off for 10 s. Here the device was biased with 2 V. The dark currents are subtracted from the data. d) Illumination results in a photocurrent component in the current–voltage curve. The photocurrent (blue dots) is obtained as the difference of the current–voltage curve under laser illumination (red) and in the dark (gray). The wavelength of the incident light was 635 nm and the peak intensity was 19.1 kW/cm^2 in the optical experiments.

We first characterize the charge transport properties of the fabricated devices in the absence of illumination. The experiments are performed under ambient conditions. The drain current I_D as a function of drain-source voltage V_D is shown in Fig. 2a for devices with the GNRs oriented across the gap separating the source and drain electrodes and for devices with the GNRs oriented in the perpendicular direction. Data for point-like contacts is shown in Supporting Information Fig. S1b. The degree of alignment of the GNRs is manifested by the strong polarization dependence of the Raman scattering signal of the samples (see Supporting Information Fig. S2a and S2b). The drain current strongly depends on the orientation of the GNRs in the gap, with the current being much higher for transport along the GNRs, e.g., the ratio of the current for the two orientations exceeds 27 at $V_{\mathrm{D}} = 2$ V in Fig. 2a. This is in agreement with recent observation of inter-ribbon hopping in films of AGNRs.[33] For transport in the direction perpendicular to the GNRs the number of hopping events required to cross the gap is much larger than for transport along the GNRs. This results in the observed orientation dependence of the drain current. To prove the role of GNRs in current transport in the devices, we used oxygen plasma to etch the GNRs from selected samples after all other measurements. The GNRs characteristic features vanish from Raman spectra and the charge transport ceases after the etching, as observed in Fig. 1a (see also Supporting Information Fig. S2c-S2e). This proves that the charge transport is due to the GNRs.

The current–voltage curves are nonlinear above a threshold voltage and can be described by a power law $I_{\mathrm{D}} \propto V_{\mathrm{D}}^{n}$. From fits to the data we conclude that the exponent n is approximately 7 for transport both along and perpendicular to the GNRs. The threshold voltages were determined from the change of the slope of the current–voltage curves in a log–log plot (see Supporting Information Fig. S3). The corresponding values are 1.0 V and 1.5 V for devices with the GNRs across and perpendicular to the gap between the source and drain electrodes, respectively. The power law type curves and the values of the exponents are in good agreement with the space-charge limited current transport model in the presence of deep traps.[33,35–38] In this model, which is often used to describe short-channel organic field-effect transistors, localized states in the semiconductor are filled upon application of an electric field. This results in the build up of a space-charge layer, which hampers carrier injection. We finally point out that the transport at higher voltage is further influenced by Joule heating as discussed below.

We next study the photodetection performance of the devices in the visible spectral range. The optical measurements are performed in a confocal microscopy setup (see Methods Section). Figure 2b shows a schematic energy band diagram of the device when $V_{\mathrm{D}} > 0$ V for the cases when it is under illumination (top) and in the dark (bottom). In the dark, carriers can be injected from the metal contacts into the GNRs and be transported across the gap between the source and drain electrodes. Laser illumination of the device generates carriers, which are separated and transported to the electrodes under the influence of the bias electric field. In this case the device operates as a photoconductive detector. Additionally, charge transport may be enhanced due to heating generated by light absorption in the metal electrodes and the GNRs. The hopping transport responsible for conduction through the layer of GNRs is enhanced at higher temperature.[39,40] Figure 2c shows the temporal photoresponse of the device introduced in Fig. 1. The incident light is a focused single-mode laser beam with peak intensity of 19.1 kW/cm^2 and wavelength of 635 nm, and $V_{\mathrm{D}} =$ 2 V. The photoresponse is shown for both polarizations along (red) and perpendicular to (gray) GNRs. Here the dark currents (at $V_{\mathrm{D}} = 2$ V) are substracted from the responses for both polarizations. Additionally, from the obtained photocurrent for the perpendicular polarization, a time-dependent background current $I_{\mathrm{bk}}(t)$ describing the gradual increase in the current due to ad- and desorption of impurities is subtracted. As the functional form for the background current we use $I_{\mathrm{bk}}(t) = I_0 - \Delta I \exp(-t/\tau)$, where the constants I_0, ΔI, and τ are obtained by fitting to data in Fig. 2c during the periods without the illumination. The origin of the increase is discussed in detail below. The data without background subtraction are shown in Supporting Information Fig. S4a. The incident laser beam is focused down to 1 μm diameter and located at the center of the device. The beam is sequentially switched with a mechanical shutter on for 5 s after a 10 s off time. The maximum measured photocurrent for the device for polarization parallel to the GNRs is 2.65 nA. The resulting responsivity, which is defined as the ratio of the photocurrent and applied optical power, is 0.035 mAW^{-1} for the wavelength 635 nm and at a bias of 2 V. The gradual decrease (increase) of the current during the periods with the laser on (off) visible in Fig. 2c is due to the ad- and desorption of impurities, which is discussed in detail below. Finally, we remark that the devices gradually degrade when exposed to light under ambient conditions resulting in a decrease of the photocurrent. This is consistent with our earlier observation that the photoluminescence properties of GNRs are modified due to the creation of defects when exposed to light under ambient conditions.[32]

For the polarization of the incident light perpendicular to the GNRs, the photoresponse is reduced, but less than expected based on the observed polarization anisotropy in absorption of GNRs (see Fig. 4b) and Raman signal (see Supporting Information Fig. S2a and S2b).[18,28] In addition to the polarization-dependent absorption of light by the GNRs, the polarization dependence of the signal is additionally enhanced by the difference in intensity distribution in the electrode structure for the two polarization states of the incident light. This is discussed in detail below. We attribute the photocurrent for perpendicular polarization dominantly to an increase in charge transport due to improved transport at GNR–GNR interfaces at higher temperature.[39–41] This is supported by the observation that for a device with the GNRs aligned perpendicular to the line connecting the source and drain electrodes, the photocurrent is decreased but non-zero and almost independent of the polarization (see Supporting Information Fig. S4b). In our devices, absorption in the metal electrodes results in heating, which raises the temperature in the GNRs. This process is discussed below (see also Fig. 4d).

The drain current as a function of bias voltage V_D is compared in Fig. 2d for the dark (gray) and under illumination (red) cases. The incident beam is polarized along the GNRs. To gain further information about the photodetection mechanism, the light-generated current can be extracted from this data as the difference in the drain current under illumination I_on and in the dark I_off. The photocurrent $I_\mathrm{ph} = I_\mathrm{on} - I_\mathrm{off}$ shows linear dependence on V_D (see Fig. 2d). The slope of the photocurrent as a function of V_D changes at 1.3 V due to thermal–enhanced tunneling of photogenerated carriers at GNR-electrode interfaces.[42] The linear behavior of I_ph as a function of V_D suggests that photoconduction is the dominant effect in the observed photoresponse for the device with the GNRs aligned across the gap between the electrodes. The photocurrent originates in the increase in conductivity due to photogenerated carriers. The absence of saturation in photocurrent is an indication of a high recombination rate in GNRs.

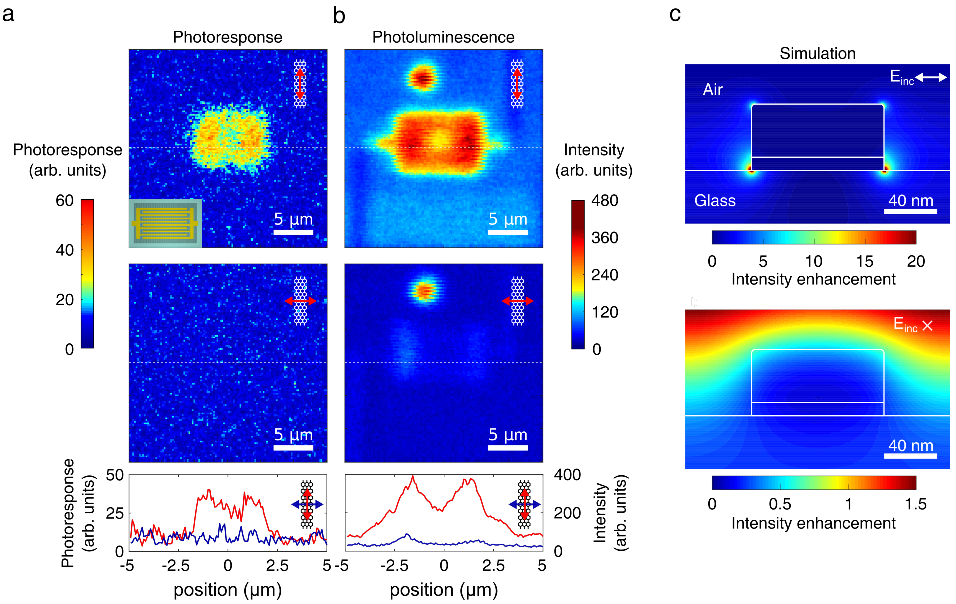

Figure 3: a) The photocurrent is only observed when the incident light is at the electrodes bridged by the GNRs (top). No signal is measured when the electrodes leading away from the nanostructure are illuminated. The signal for light polarized perpendicular to the GNRs (middle) is too weak to be detected. The inset in the top panel shows a sketch of the electrode structure. The data was measured under 1.5 V bias using a laser wavelength of 635 nm with an intensity of 19.1 kW/cm^2. b) The fluorescence micrographs recorded synchronously with the photocurrent distributions show a much stronger signal for light polarized along the GNRs (top) than perpendicular (middle). The signal is enhanced due to plasmons in the region of the electrode structure. The bottom panels in a) and b) show horizontal cross sections of the photoresponse and photoluminescence, respectively, for the vertical positions marked by dashed lines in the top and middle panels. c) The simulated distribution of intensity enhancement around an electrode for polarization perpendicular (top) and parallel (bottom) to the electrodes illustrates the enhancement due to the excitation of plasmons.

We next focus on the position dependence of the photodetection in the device. For this purpose we recorded the photocurrent as a function of position of the incident laser spot in a sample–scanning confocal microscope (see Methods Section for details). The fluorescence signal of GNRs was recorded simultaneously. The photocurrent and fluorescence signal as a function of position of excitation beam are shown in Fig. 3a and Fig. 3b, respectively, for 635 nm wavelength incident light. Here the upper panels represent the data for incident beam polarized along the GNRs. In the middle panels the polarization is turned by 90 degrees. The key finding is that the active detection area is limited to the area of the interdigitated electrodes, while a constant fluorescence signal is observed from the surrounding region. Only GNRs between finger electrodes contribute to the detection (and current transport). If photothermal effects would be the source of the drain current, we would expect a signal along the electrodes leading away from the device. In the devices studied here, the photocurrent is unidirectional and the devices can thus be used under global illumination. This is in contrast to graphene–based detectors where carriers generated near the electrodes are harvested due to the bending of the energy bands near the metal–graphene interface.[2,3,6,24–26,43] The photocurrent at opposite electrodes shows a sign reversal and the resulting overall photocurrent is zero for global illumination. This can be compensated through biasing the device, but this results in a dark current several orders of magnitude higher than the generated photocurrent.[44]

For light polarized perpendicular to the GNRs, the photocurrent is too low to be detected as observed in the micrograph for perpendicular polarization in Fig. 3a. The fluorescence micrographs (Fig. 3b) also show similar polarization dependence. The degree of polarization anisotropy is increased by the enhancement of the intensity of the incident optical field in the nanoscale metallic structure. To study this, we simulated the electric field distribution in the structure using the finite element method (see Methods Section). Here we consider a two-dimensional structure, where the electrode structure is represented by an array of wires. The incident field is a plane wave incident along the substrate normal with a vacuum wavelength of 635 nm. Figure 3c shows the intensity enhancement around an electrode. The beam is polarized perpendicular (along GNRs) to the electrode in upper panels and it is turned by 90 degree in lower panels. The intensity shows strong enhancement for polarization perpendicular (along GNRs) to the wires at the corners of the gold wire with a noticeable enhancement remaining further away. For the other polarization (lower panel) there are no hotspots of the intensity and the overall intensity is slightly attenuated in comparison to the case of no grating.

We next determine the wavelength dependence of the responsivity. Figure 4a shows the measured responsivity as a function of wavelength of incident light for light polarized along (red) and perpendicular to (blue) the GNRs. Here the bias voltage was $V_{\mathrm{D}} = 2.5$ V and the responsivity has been normalized with its maximum value for light polarized along the GNRs. The device exhibits a broadband response in the measurement range mimicking the extinction spectra of the GNRs (Fig. 4b). The spectra shown in Fig. 4b were measured for a single layer of GNRs on a separate transparent substrate. For a single layer of GNRs, the extinction directly represents the absorption features as the reflection is negligible.[28] The increase in responsivity for parallel polarization in shorter wavelength regime is due to broad excitonic resonances in the extinction spectrum at approximately 590 and 538 nm wavelength.[18] The wavelength dependence can be tuned by changing the width and edge-geometry of the GNRs.[19–21]

In shorter wavelength regime, the heating due to absorption of light is expected to have a more pronounced contribution to the photoresponse as a result of increased absorption in the metal.[45] We show in Fig. 4c and 4d the simulated average intensity enhancement at the level of the GNRs between the electrodes and the absorption in the metal electrodes, respectively. The most important observation is that the structure enhances the intensity of the incident light for polarization along the GNRs while the absorption in the metal is almost insensitive to the polarization. This observation together with the polarization-sensitive absorption of the GNRs allows us to conclude that the polarization dependent component of the signal originates in carrier generation in the GNRs while the polarization insensitive part is due to laser–induced heating of the electrodes. To study the influence of heating in our devices, we measured the response for a device with a point-like gap, where the gap was short circuited so that no photoconductive effect was detected. We observed no signal for the same power range (approximately 8 μW at 530 nm wavelength) as used in the experiments shown in Fig. 4. The smallest detectable signals required an incident power 240 times larger (data shown in Supporting Information Fig. S5). The results from this experiment proves the role of the GNRs in the photoconductive detection. Furthermore, the thermal effect observed at high incident intensity results in a decrease of the drain current distinctively different from the device with open gap.

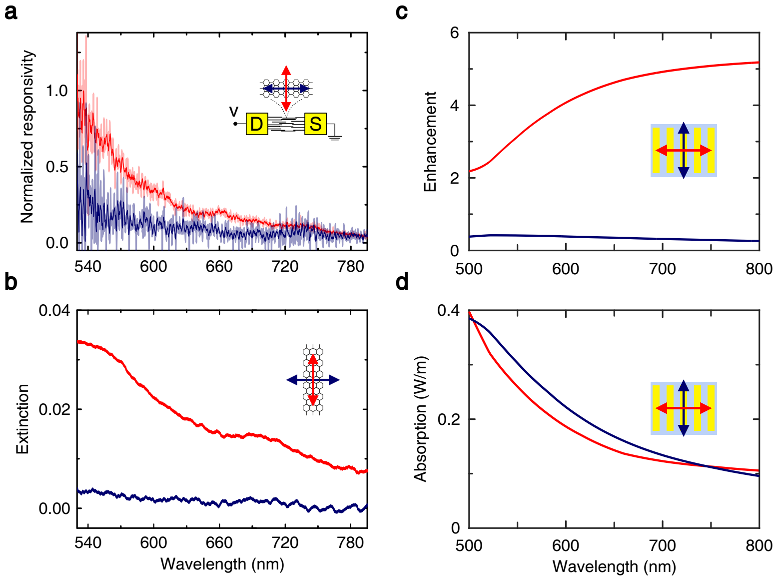

Figure 4: a) The responsivity is larger for illumination polarized along (red) than perpendicular to (blue) GNRs. The device is under 2.5 V bias. The smoothed data of the responsivity as a function of wavelength are shown additionally. b) The wavelength dependence of the response of the detector mimic the measured extinction spectra for parallel (red) and perpendicular (blue) polarizations. c) The simulated average intensity enhancement in the region of the GNRs for polarization parallel (blue) and perpendicular (red) to the electrodes illustrates the influence of plasmons when perpendicular polarization is used. d) The absorption of the metal is almost insensitive to the polarization state of the incident light.

We observe that the devices exhibit a gradual increase in current when a constant bias is applied. The time evolution of current is shown in Fig. 5a for $V_\mathrm{D} = 2$ V. The effect appears to be independent of orientation of GNRs as it is also observed for devices with perpendicular GNRs (data shown in Supporting Information Fig. S6). We remark that scanning electron microscopy was performed on the devices after all other characterization steps. Moreover, the process appears to be reversible as seen in Fig. 5b (see also Supporting Information Fig. S6). The observed increase in current is thus not due to modification of the structure.

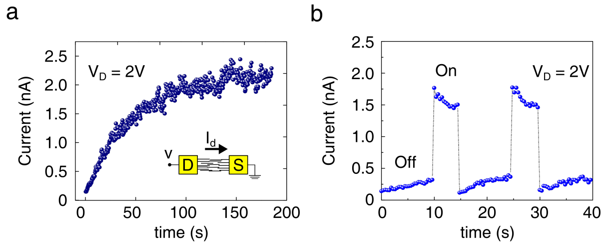

Figure 5: a) The drain current is increased due to annealing of the sample. Here the average of three time traces measured without illumination is shown. b) The current undergoes a gradual increase in dark (as in a)). Turning on the illumination reverses the process leading to a decreasing current as a function of time. Here the drain voltage is $V_{\mathrm{D}} = 2$ V.

In carbon nanotube based devices Joule heating is expected to influence charge transport by changing the temperature and thus conductivity.[46] However, such changes are expected to be very fast unlike the slow change observed here. For example, devices based on films of SWCNTs,[47] single or multilayers of graphene,[48] or a heterostructure of hBN–graphene–hBN[49] have been demonstrated as high–speed Blackbody emitters based on Joule heating and with a response time below a nanosecond. This is far from the time constant observed here (43.5 s). On the other hand, Joule heating can provide high enough temperature to result in desorption of contaminants from the GNRs. As shown in Fig. 5b, the current gradually increases in dark and decreases under illumination (see also Fig. 2c). Similar slow changes in charge transport have been reported in individual[50,51] and films[41,52] of SWCNTs, where the origin of the changes is attributed to absorption or desorption of dopants. For example, in Ref. 50 the gradual increase in current for constant bias is attributed to absorption of oxygen. We similarly attribute the observed slow current changes to desorption of contaminants from the sample due to Joule heating.

In summary, we have demonstrated a polarization sensitive photodetector based on aligned semiconducting GNRs with a responsivity of 0.035 mAW^{-1} (at $V_{\mathrm{D}} = 2$ V) and a dark current below 30 pA (at $V_D = 1.5$ V). Considering that the coverage of the GNRs is smaller than 50 %,[28,53] we conclude that the responsivity of the detector is comparable to the values reported for single layer graphene devices.[2,3,43,44,54] Charge transport through the device can be improved by decreasing the gap between source and drain or by growing longer GNRs. The semiconducting nature of the GNRs results in a significantly lower dark current than graphene-based photodetectors. The detection mechanism of the device is dominantly photoconductive: photogenerated carriers result in an increase of the conductance across the active region of GNRs. The photoconductive signal displays a linear dependence of the photocurrent on the bias voltage. Based on the position and polarization dependence of the photocurrent, we can exclude pure thermal effects from being the main source of the signal of the detector. The wavelength dependence of the detector follows the absorption spectra of the GNRs. The responsivity spectrum can thus be engineered by the choice of the GNRs. The use of aligned GNRs can be beneficial for high frequency and low power consumption as has been previously observed for FETs based on aligned-CNTs.[55–57]

Our simple proof-of-concept device demonstrates the potential of using GNRs as the active material in a photodetector. It opens up several directions for further research. The versatility of GNR properties is ideal for developing detectors for different spectral regimes. In particular, by using smaller bandgap GNRs the important infrared spectral range can be addressed. The bandwidth of our photodetector was not addressed within this work. This is an obvious area of further research. Recently photodetectors based on graphene with very high bandwidth have been demonstrated.[58] Graphene nanoribbon-based systems might offer a similarly high speed. A key aspect of the bottom-up synthesized GNRs is their identical structure at the atomic level over large areas. This is ideal for studying the transport of photogenerated carriers in the structure and for example the influence of the GNR-metal interface or chemical modification on transport. Finally, the homogeneity of the samples should allow developing multi-pixel devices and the polarization-dependence of the absorption can be applied in polarimetric measurements.

Methods

7–AGNRs growth and transfer

7–AGNRs were synthesized by surface polymerization of 10,10'-dibromo-9,9'-bianthracene (DBBA) molecules on Au(788) surface in ultra-high vacuum (UHV).[34,59] First gold was cleaned via three cycles of Ar+ sputtering (800V) followed by annealing at 500 °C. We used a home–built evaporator to evaporate DBBA molecules from quartz crucible. A quartz microbalance was used to control the deposition rate and thickness to deposit approximately 4 Å of DBBA molecules on the gold substrate at room temperature. We used the density and Z–factor of graphite for the thickness measurement. Initial annealing to 200 °C for 30 min was employed to induce surface polymerization of DBBA. This was followed by 15 min annealing at 380 °C for debromization and cyclodehydrogeneration of the polymer to form 7–AGNRs.

The grown 7–AGNRs were transferred from the Au(788) surface to optical glass and silicon substrates. We applied the so-called bubbling transfer, which is based on electrochemical delamination of the layer of GNRs.[32] To perform the transfer, the 7–AGNRs/Au(788) sample was coated by a layer of poly(methyl methacrylate) (PMMA) and was then placed in an electrochemical cell with an NaOH aqueous solution (1 mol/L). Due to the reduction of water at the negatively charged cathode in the cell, the PMMA/7–AGNRs layer starts to detach from the Au(788) substrate by the emerging H_2 gas bubbles at the 7-AGNRs/Au(788) interface. After cleaning the floating PMMA/7–AGNRs layer in distilled water, it was placed onto the target substrate. In order to remove PMMA and clean the surface, the sample was placed in 1,2-dichloroethane for 48 h and afterwards in methanol for approximately 1 h. The sample was subsequently dried by blowing with dry nitrogen. The quality of the GNRs and their alignment was investigated using polarized-light Raman spectroscopy with 532 nm wavelength light.[32] Spectra were measured in UHV before transfer of GNRs and after transfer under ambient conditions. Exemplary spectra of polarization–resolved Raman are shown in

Supporting Information Fig. S2a and S2b. We observe only characteristic Raman features of GNRs and a strong dependence on the polarization of the incident light indicative of aligned GNRs and no remaining PMMA.

Device fabrication

As substrates we used polished optical glass (Schott D 263 T) and highly doped single-side polished silicon with 300 nm thick thermally grown oxide. The substrates were patterned using optical lithography with 150×150 μm^2-sized contact pads for electrical probing. As contact material we used 10 nm of titanium for adhesion followed by 50 nm of gold. A single layer of GNRs was transferred onto the patterned substrates. The nanoscale electrodes defining the photodetector and connecting the active region to the large contact pads were subsequently prepared using electron beam lithography. For this, the samples were coated with a double layer of PMMA. The bottom layer (molecular weight 250000) is more sensitive than the top layer (molecular weight 950000), resulting in an undercut that facilitates lift-off processing. For structures prepared on glass substrates, a 30 nm thick layer of conductive polymer (eSpacer 300Z) was spin coated on top of the resist to prevent charging of the sample. After exposure in the electron beam writer, the sample was developed and a 10 nm layer of titanium and a 40 nm layer of gold were deposited by thermal evaporation from resistively heated sources. Finally, the metal was removed from the unexposed regions of the sample using a lift-off process.

Simulations

We performed full-field simulations using a finite element solver (Comsol Multiphysics). We use a two-dimensional simulation model with periodic boundary conditions along the direction of the substrate to obtain the intensity distribution in the electrode structure. The intensity enhancement shown in Fig. 3c is calculated as the ratio of the square of the norm of the electric field with the electrode and without the electrode (but with the substrate).

For the spectrum shown in Fig. 4c, we average the intensity enhancement shown in Fig. 3c between the electrodes at a height of 2 nm above the substrate. For the simulations we assume a wavelength independent refractive index of 1.5 for the glass substrate and use the data from Refs. 60 and 61 for the refractive index of titanium and gold, respectively.

Electrical and optical measurements

After fabrication, the devices were first electrically characterized using a semiconductor analyzer in nitrogen atmosphere at room temperature. Further optical and electrical characterization was performed under ambient conditions in a home–built sample–scanning confocal microscope. The polarization of the incident light was controlled with a polarizer and a half–wave plate. A 532 nm laser and a supercontinuum source (SCS) were used for illumination. The beam is focused using an objective with 0.8 numerical aperture, resulting in an approximately 1 μm diameter focal spot. The fluorescence or Raman scattered light was collected with the objective and separated from the excitation using dielectric filters. In the emission path, a quarter wave plate was installed to guarantee polarization–independent detection. The emission was directed to a grating spectrometer equipped with a deep-cooled CCD camera for spectral information or to a single–photon counting module. The polarization–dependencies of the optical train were compensated in the data analysis.

To measure the temporal photoresponse, the bias voltage dependence of the photocurrent, and the wavelength dependence of the photocurrent, the devices were connected to a source measure unit in the confocal microscope. To acquire the wavelength dependence of the photocurrent, the wavelength of SCS was sweept at a rate of 1 nm/s using a 5 nm bandwidth of the laser. The wavelength–dependence of the setup and variations in the laser power were compensated using a calibrated power meter.

In the position–resolved measurement a mechanical chopper was used to modulate the power of the incident light with a frequency of 1.2 kHz. The electrodes of the sample were connected to a transimpedance–amplifier, which was also used to bias the detector

($V_\mathrm{D} = 1.5$ V). The output of the amplifier was connected to a lock–in amplifier to demodulate the signal. The demodulated signal was recorded synchronously with the scanning of the sample in the microscope.

Acknowledgements

K.L. and A.G. acknowledge DFG projects LI 2633/5-1 and GR 3708/4-1. S.K.A. acknowledges Bonn Cologne graduate school (BCGS) of physics and astronomy and DAAD for financial support. Research was supported by the University of Cologne through the Institutional Strategy of the University of Cologne within the German Excellence Initiative (QM^2). A.G. and B.S. thank the ERC grant No. 648589 ”SUPER-2D”. Research is supported by the U.S. Department of Energy, Office of Science, Basic Energy Sciences, under Award # DE-SC0010409 (design, synthesis, and characterization of molecular precursors). K.L. and S.K.A. acknowledge a grant from the Volkswagen Foundation.

The authors declare no competing financial interest.

Author contributions

K.L. planned the study. The precursor molecules were synthesized by D.Haberer under the supervision of F.R.F. B.V.S. grew and transferred the GNRs under the supervision of A.G. The photodetector nanostructures were fabricated by K.L. and S.K.A. under the supervision of Y.A. S.K.A. carried out the electrical characterization and photodetection experiments under the supervision of K.L. and with support from D.Hertel and K.M. The manuscript was written by K.L. and S.K.A. with contributions from all authors. All authors have given approval to the final version of the manuscript.

Supporting Information Available

Data on point-like structures, polarization-resolved Raman spectra, raw data for time-resolved drain-current, results for photodetector with closed gap, time-resolved increase of current due to contaminants.

References

(1) Koppens, F. H. L.; Mueller, T.; Avouris, P.; Ferrari, A. C.; Vitiello, M. S.; Polini, M. *Nature Nanotechnology* **2014**, *9*, 780–793.

(2) Lemme, M. C.; Koppens, F. H. L.; Falk, A. L.; Rudner, M. S.; Park, H.; Levitov, L. S.; Marcus, C. M. *Nano Letters* **2011**, *11*, 4134–4137.

(3) Rao, G.; Freitag, M.; Chiu, H.-Y.; Sundaram, R. S.; Avouris, P. *ACS Nano* **2011**, *7*, 5848–5854.

(4) Fang, J.; Wang, D.; DeVault, C. T.; Chung, T.-F.; Chen, Y. P.; Boltasseva, A.; Shalaev, V. M.; Kildishev, A. V. *Nano Letters* **2017**, *17*, 57–62.

(5) Gabor, N. M.; Song, J. C. W.; Ma, Q.; Nair, N. L.; Taychatanapat, T.; Watanabe, K.; Taniguchi, T.; Levitov, L. S.; Jarillo-Herrero, P. *Science* **2011**, *334*, 648–652.

(6) Mueller, T.; Xia, F.; Avouris, P. *Nature Photonics* **2010**, *4*, 297–301.

(7) Han, Q.; Gao, T.; Zhang, R.; Chen, Y.; Chen, J.; Liu, G.; Zhang, Y.; Liu, Z.; Wu, X.; Yu, D. *Scientific Reports* **2013**, *3*, 3533.

(8) Bartolomeo, A. D.; Genovese, L.; Foller, T.; Giubileo, F.; Luongo, G.; Croin, L.; Liang, S.-J.; Ang, L. K.; Schleberger, M. *Nanotechnology* **2017**, *28*, 21.

(9) Furchi, M. M.; Polyushkin, D. K.; Pospischil, A.; Mueller, T. *Nano Letters* **2014**, *14*, 6165–6170.

(10) Buscema, M.; Barkelid, M.; Zwiller, V.; van der Zant, H. S. J.; Steele, G. A.; Castellanos-Gomez, A. *Nano Letters* **2013**, *13*, 358–363.

(11) Duttaa, S.; Pati, S. K. *J. Mater. Chem.* **2010**, *20*, 8207–8223.

(12) Corso, M.; Carbonell-Sanromà, E.; de Oteyza, D. G. In *On-Surface Synthesis II*; de Oteyza, D. G., Rogero, C., Eds.; Springer, Cham, 2018; pp 113–152.

(13) Gröning, O.; Wang, S.; Yao, X.; Pignedoli, A., Carlo; Barin, B., Gabriela; Daniels, C.; Cupo, A.; Meunier, V.; Feng, X.; Narita, A.; Müllen, K.; Ruffieux, P.; Fasel, R. *Nature* **2018**, *560*, 209–213.

(14) Rizzo, D. J.; Veber, G.; Cao, T.; Bronner, C.; Chen, T.; Zhao, F.; Rodriguez, H.; Louie, S. G.; Crommie, M. F.; Fischer, F. R. *Nature* **2018**, *560*, 204–208.

(15) Ruffieux, P.; Wang, S.; Yang, B.; Sánchez-Sánchez, C.; Liu, J.; Dienel, T.; Talirz, L.; Shinde, P.; Pignedoli, C. A.; Passerone, D.; Dumslaff, T.; Feng, X.; Müllen, K.; Fasel, R. *Nature* **2016**, *531*, 489–492.

(16) Llinas, J. P. et al. *Nature Communications* **2017**, *8*, 633.

(17) Ruffieux, P.; Cai, J.; Plumb, N. C.; Patthey, L.; Prezzi, D.; Ferretti, A.; Molinari, E.; Feng, X.; Müllen, K.; Pignedoli, C. A.; Fasel, R. *ACS Nano* **2012**, *6*, 6930–6935.

(18) Denk, R.; Hohage, M.; Zeppenfeld, P.; Cai, J.; Pignedoli, C. A.; Söde, H.; Fasel, R.; Feng, X.; Müllen, K.; Prezzi, S. W. D.; Ferretti, A.; Ruini, A.; Molinari, E.; Ruffieux, P. *Nature Communications* **2014**, *5*, 4253.

(19) Merino-Díez, N.; Garcia-Lekue, A.; Carbonell-Sanromà, E.; Li, J.; Corso, M.; Colazzo, L.; Sedona, F.; Sánchez-Portal, D.; Pascual, J. I.; de Oteyza, D. G. *ACS Nano* **2017**, *11*, 11661–11668.

(20) Wang, W.-X.; Zhou, M.; Li, X.; Li, S.-Y.; Wu, X.; Duan, W.; He, L. *Phys. Rev. B* **2016**, *93*, 241403.

(21) Kimouche, A.; Ervasti, M. M.; Drost, R.; Halonen, S.; Harju, A.; Joensuu, P. M.; Sainio, J.; Liljeroth, P. *Nature Communications* **2015**, *7*, 10177.

(22) Cloke, R. R.; Marangoni, T.; Nguyen, G. D.; Joshi, T.; Rizzo, D. J.; Bronner, C.; Cao, T.; Louie, S. G.; Crommie, M. F.; Fischer, F. R. *Journal of the American Chemical Society* **2015**, *137*, 8872–8875.

(23) Tyo, J. S.; Goldstein, D. L.; Chenault, D. B.; Shaw, J. A. *Appl. Opt.* **2006**, *45*, 5453–5469.

(24) Xia, F.; Mueller, T.; Golizadeh-Mojarad, R.; Freitag, M.; Lin, Y.-M.; Tsang, J.; Perebeinos, V.; Avouris, P. *Nano Letters* **2009**, *9*, 1039–1044.

(25) Yao, Y.; Shankar, R.; Rauter, P.; Song, Y.; Kong, J.; Loncar, M.; Capasso, F. *Nano Letters* **2014**, *14*, 3749–3754.

(26) Chakraborty, C.; Beams, R.; Goodfellow, K. M.; Wicks, G. W.; Novotny, L.; Vamivakas, A. N. *Appl. Phys. Lett.* **2014**, *105*, 241114.

(27) Shiue, R.-J.; Gao, Y.; Wang, Y.; Peng, C.; Robertson, A. D.; Efetov, D. K.; Assefa, S.; Koppens, F. H. L.; Hone, J.; Englund, D. *Nano Letters* **2016**, *15*, 7288–7293.

(28) Alavi, S. K.; Senkovskiy, B. V.; Pfeiffer, M.; Haberer, D.; Fischer, F. R.; Grüneis, A.; Lindfors, K. *2D Materials* **2019**, *6*, 035009.

(29) Shi, S.-F.; Xu, X.; Ralph, D. C.; McEuen, P. L. *Nano Letters* **2011**, *11*, 1814–1818.

(30) Freitag, M.; Low, T.; Zhu, W.; Yan, H.; Xia, F.; Avouris, P. *Nature Communications* **2013**, *4*, 1951.

(31) Wei, D.; Xie, L.; Lee, K. K.; Hu, Z.; Tan, S.; Chen, W.; Sow, C. H.; Chen, K.; Liu, Y.; Wee, A. T. S. *Nature Communications* **2013**, *4*, 1374.

(32) Senkovskiy, B. V. et al. *Nano Letters* **2017**, *17*, 4029–4037.

(33) Ohtomo, M.; Sekine, Y.; Hibino, H.; Yamamoto, H. *Appl. phys. Lett.* **2018**, *112*, 021602.

(34) Linden, S.; Zhong, D.; Timmer, A.; Aghdassi, N.; Franke, J. H.; Zhang, H.; Feng, X.; Müllen, K.; Fuchs, H.; Chi, L.; Zacharias, H. *Phys. Rev. Lett.* **2012**, *108*, 216801.

(35) Wanga, J. Z.; Zheng, Z. H.; Sirringhaus, H. *Appl. Phys. Lett.* **2006**, *89*, 083513.

(36) Hirose, T.; Nagase, T.; Ueda, T. K. R.; Otomo, A.; Naito, H. *Appl. Phys. Lett.* **2010**, *97*, 083301.

(37) Carbone, A.; Kotowska, B. K.; ; Kotowski, D. *Phys. Rev. Lett.* **2005**, *95*, 236601.

(38) Chung, H.-J.; Jeong, J. H.; Ahn, T. K.; Lee, H. J.; Kim, M.; Jun, K.; Park, J.-S.; Jeong, J. K.; Mo, Y.-G.; Kim, H. D. *Electrochem. Solid-State Lett.* **2008**, *11*, H51–H54.

(39) Kaiser, A. B.; Skakálová, V. *Chem. Soc. Rev.* **2011**, *40*, 3786–3801.

(40) Richter, N.; Chen, Z.; Tries, A.; Prechtl, T.; Narita, A.; Müllen, K.; Asadi, K.; Bonn, M.; Kläui, M. *ArXiv* **2018**, 1806.00962.

(41) Hong, W.; Lee, E.; Park, J. K.; Lee, C. E. *J. Appl. Phys* **2013**, *113*, 216101.

(42) Freitag, M.; Martin, Y.; Misewich, J. A.; Martel, R.; Avouris, P. *Nano Letters* **2003**, *3*, 1067–1071.

(43) Xia, F.; Mueller, T.; Lin, Y.-M.; Valdes-Garcia, A.; Avouris, P. *Nature Nanotechnology* **2009**, *4*, 839–843.

(44) Freitag, M.; Low, T.; Xia, F.; Avouris, P. *Nature Photonics* **2013**, *7*, 53–59.

(45) Echtermeyer, T. J.; Nene, P. S.; Trushin, M.; Gorbachev, R. V.; Eiden, A. L.; Milana, S.; Sun, Z.; Schliemann, J.; Lidorikis, E.; Novoselov, K. S.; Ferrari, A. C. *Nano Letters* **2014**, *14*, 3733–3742.

(46) Itkis, M. E.; Yu, A.; Haddon, R. C. *Nano Letters* **2008**, *8*, 2224–2228.

(47) Mori, T.; Yamauchi, Y.; Honda, S.; Maki, H. *Nano Letters* **2014**, *14*, 3277–3283.

(48) Miyoshi, Y.; Fukazawa, Y.; Amasaka, Y.; Reckmann, R.; Yokoi, T.; Ishida, K.; Kawahara, K.; Ago, H.; Maki, H. *Nature Communications* **2018**, *9*, 1279.

(49) Shiue, R.-J.; Gao, Y.; Tan, C.; Peng, C.; Zheng, J.; Efetov, D. K.; Duck Kim, Y.; Hone, J.; Englund, D. *Nature Communications* **2019**, *10*, 109.

(50) Chen, R. J.; Franklin, N. R.; Kong, J.; Cao, J.; Tombler, T. W.; Zhang, Y.; Dai, H. *Applied Physics Letters* **2001**, *79*, 2258–2260.

(51) Kong, J.; Franklin, N. R.; Zhou, C.; Chapline, M. G.; Peng, S.; Cho, K.; Dai, H. *Science* **2000**, *287*, 622–625.

(52) Collins, P. G.; Bradley, K.; Ishigami, M.; Zettl, A. *Science* **2000**, *287*, 1801–1804.

(53) Passi, V.; Gahoi, A.; Senkovskiy, V., Boris; Haberer, D.; Fischer, R., F.; Grüneis, A.; Lemme, C., Max *ACS Appl. Mater. Interfaces* **2018**, *10*, 9900–9903.

(54) Liu, Y.; Cheng, R.; Liao, L.; Zhou, H.; Bai, J.; Liu, G.; Liu, L.; Huang, Y.; Duan, X. *Nature Communications* **2011**, *2*, 579.

(55) Brady, G. J.; Way, A. J.; Safron, N. S.; Evensen, H. T.; Gopalan, P.; Arnold, M. S. *Sci. Adv.* **2016**, *2*, e1601240.

(56) Tulevski, G. S.; Franklin, A. D.; Frank, D.; Lobez, J. M.; Cao, Q.; Park, H.; Afzali, A.; Han, S.-J.; Hannon, J. B.; Haensch, W. *ACS Nano* **2014**, *8*, 8730–8745.

(57) Brady, G. J.; Joo, Y.; Roy, S. S.; Gopalan, P.; Arnold, M. S. *Appl. Phys. Lett.* **2014**, *104*, 083107.

(58) Ma, P.; Salamin, Y.; Baeuerle, B.; Josten, A.; Heni, W.; Emboras, A.; Leuthold, J. *ACS Photonics* **2019**, *6*, 154–161.

(59) Blankenburg, S.; Cai, J.; Ruffieux, P.; Jaafar, R.; Passerone, D.; Feng, X.; Müllen, K.; Fasel, R.; Pignedoli, C. A. *ACS Nano* **2012**, *6*, 2020–2025.

(60) Johnson, P. B.; Christy, R. W. *Physical Review B* **1974**, *9*, 5056–5070.

(61) Johnson, P. B.; Christy, R. W. *Physical Review B* **1972**, *6*, 4370–4379.

5.3 Summary

The first demonstration of nanoscale GNR-based photodetectors has been presented in this chapter. In these photodetectors, a single layer of aligned 7–AGNRs serves as the active medium. Since the conductive channel is longer than the length of individual GNRs, electrical transport is mediated by charge hopping. This is reflected in the characteristic current-voltage curves, which exhibit nonlinear behavior.

We showed that the photodetection is a result of the two distinct effects: a dominant photoconductive and a weak polarization-insensitive photothermal effect. As expected, the former effect originates from absorption of light in the GNRs, and thus exhibits polarization dependence according to the alignment and structure of the GNRs. The latter effect is a consequence of light absorption in the electrodes and is recognized to be polarization insensitive. The contribution of each effect has been resolved with the support of position-resolved and spectral measurements. Only the GNRs between the electrodes contribute to the photodetection and the electrical transport. We measured the spectral response of our photodetectors for the range of 530−800 nm. The measured responsivity is $\approx 0.04\ \mathrm{mAW}^{-1}$ at 635 nm. Regarding the low surface coverage of the GNRs ($\approx 50\%$) [2], the responsivity is comparable with that of graphene-based photodetectors [138–140, 143]. Our results are the first step to highlight the promise of on-surface grown GNRs to develop optoelectronic devices.

CHAPTER 6

Summary and outlook

The work presented in this thesis details the investigation of the photophysical properties of atomically precise armchair graphene nanoribbons, and further their use to demonstrate nanoscale photodetection platform. In all the experiments a single layer of aligned 7-AGNRs have been used. The results for optical characterization are summarized in chapters 3 and 4. Demonstration of a nanoscale photodetector, which is the first step to apply GNRs in optoelectronics, is reported in chapter 5.

In chapter 3, I presented the results of polarization-resolved Raman spectroscopy, which has been used to evaluate the quality and ratio of alignment for transferred 7–AGNRs. The Raman spectroscopy further has been employed to resolve the excitonic features of the GNRs. It was further observed that pristine 7–AGNRs intrinsically have low PL emission. The origin of low emission in such GNRs has been attributed to be dark/quenching states [1, 2, 52]. Interestingly, the PL emission could be enhanced. I showed that this can be achieved by intentionally inducing laser-driven defects into the 7–AGNR's lattice and consequently increase their PL emission.

In chapter 4, I studied further the optical properties of GNRs using extinction spectroscopy. The extinction spectra have been measured for a single layer of aligned 7–AGNRs on quartz. The extinction spectra show polarization dependence in accordance with the Raman and PL, i.e. largest extinction for polarization along the main axis of the GNRs. It is dominated by two excitonic peaks at ≈ 2.4 and 1.77 eV. Our results show that the absorbance of a single layer of 7–AGNRs is 6.8% (at 2.4 eV photon energy), in excellent agreement with theoretical predictions ($\approx 8\%$) [2, 56], which is three times more than the absorbance of a single layer of graphene. I additionally probed the effect of defects on the extinction spectra. After induction of defects, the extinction of the GNRs does not exhibit drastic modification except for the low-energy peak (at 1.77 eV), which vanishes upon formation of the defects. It was observed that there is an inverse relation between this peak and the increase in PL emission. This relation indicates that the low-energy peak in the extinction spectrum is not the origin of the defect-induced brightening in the GNRs, but rather, it arises from a quenching state(s), and contributes to hindering the PL emission in pristine GNRs. (see chapter 4) [2]. Additional experiments were carried out to explore the formation of defects. It was found that the rate of defect formation increases monotonically as a function of photon energy. The defects were realized to be of the form of sp^3 hybridization. Further information about the microscopic details of the defects is beyond the scope of this work and remains to be explored in the future.

Chapter 5 introduces the first proof-of-concept photodetector in which 7–AGNRs have been exploited as the active material. The photodetectors consist of metal electrodes separated with ≈ 100 nm-wide gaps, fabricated on top of a single layer of aligned 7–AGNRs. The dark current of the photodetectors is tens of pA, several orders of magnitude lower than for similar graphene-based photodetectors [143], despite exhibiting similar responsivity. Unlike other 2D materials like graphene or TMDs, the active medium in our photodetectors consists of the isolated GNRs, which are separated by nanometer distances. Thus for a channel larger than the length of the GNRs (on average 30 nm), the electrical transport is through charge hopping at the interface of GNR-GNR. It was shown that the dominant detection mechanism in the photodetectors is photoconductive. The performance of the photodetectors was characterized using position-resolved and wavelength-dependent experiments. These, in combination with polarization-sensitive measurements, enabled us to resolve an additional contribution of a weak polarization-insensitive photothermal effect in the photoresponse of the photodetectors. The photothermal effect arises from light absorption in the electrodes.

The research performed in this work has opened up several new research directions and questions. In the following I will present the most relevant ones.

In the area of light emission: It is an exciting discovery that we can locally implant defects into the lattice of GNRs and influence their fundamental properties, e.g., energy structure and transitions. As a next step it would be interesting to apply our approaches to other GNRs than the 7-AGNRs studied here. This could allow tuning the emission spectrum. Chemically-driven defect points in CNTs have been employed as promising single photon emitters with a variety of spectral emission lines operating at room temperature [159, 160]. This method can be explored in GNRs for similar purposes.

This highlights the importance of fundamental knowledge about the effects behind the generation of defects in GNRs. A better understanding will provide more insight into the direction of exploiting different ways of defect implantation, which we already started to investigate. In this regard, chemical approaches, e.g., based on diazonium salts [161] or aryl groups [159], can be tested. A comparison of light-driven defect formation in air and under vacuum demonstrates the importance of gases, e.g., oxygen to implement the process (see chapter 4). A straightforward experiment would be to verify the defect formation, in a systematic manner, under the flow of selected gases. This can be combined with time-resolved spectroscopy experiment by means of which it is possible to study the dynamics of the PL emission in defected GNRs.

In parallel, we are interested in coupling GNRs to plasmonic nanostructures. This might lead to the observation of new phenomena. Recently, characteristic features of quantum emitters have been realized from GNRs, which were coupled to gold nanoantennas [162]. There, the individual GNRs in antenna hot spot show photoblinking with narrow (50 meV) emission lines around 1.7 eV. We plan to investigate this also for the GNRs in which we intentionally implant defects. This perhaps could be interesting to study the induced changes by defects in the quantum nature of the emitters.

In the direction of device demonstration: The demonstration of PDs with 7–AGNRs paves the way towards further innovation to fabricate optoelectronic devices. Here we only used 7–AGNRs. As a next simple step photodetection can be implemented using different GNRs. A large variety of GNRs with different widths and edges have already been synthesized. These can be used instead of 7–AGNRs, in order to cover various wavelength ranges in particular to address the infrared spectral range. Photodetection can be extended using multilayers of GNRs. Increasing the number of layers increases the absorption of light and thus could improve the photodetection, though this could lead to

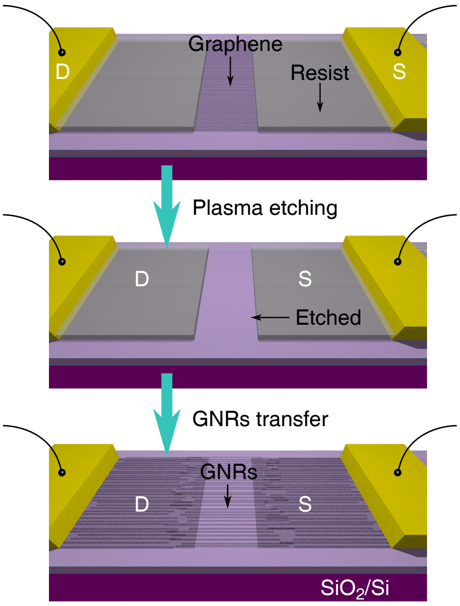

Figure 6.1: A simple design of GNRs-based photodetector with the advantage of graphene electrodes. The standard electron beam lithography (EBL) method can be employed to prepare nanoscale gaps in EBL resist, which is coated on top of a single layer of graphene. The sample is then exposed to oxygen plasma. The graphene is consequently removed from the uncovered area. Eventually, the GNRs layer can be transferred on top of graphene electrodes to prepare the PD.

slower response times [125, 163].

The performance of our devices is limited by the charge hopping mechanism at the interface of GNR-GNR. This is because the separation between the electrodes is larger than the GNR's length. For shorter electrode separation, with no hopping event, current above 1 μA has been reported in a single 9–AGNR field-effect transistor [113]. The current is expected to increase significantly for devices fabricated using aligned GNRs, where many GNRs can contribute to the charge transport. This consequently improves the collection efficiency of photo-generated carriers in GNR-based PDs. Growth of longer GNRs is thus a key task for future research. In this direction, an alternative is the lateral fusion of GNRs [59, 164]. The resulting physical bond between neighboring GNRs should significantly enhance the charge transport.

In general, the injection of charge carriers into 2D materials is limited due to the high tunneling barrier at the 2D-metal interface. This has also been reported for single GNR-based devices [110, 113]. This limitation could presumably be eliminated by replacing the metal with, e.g., graphene electrodes for which the barriers potentially are smaller [32, 102, 165]. We plan to demonstrate such devices. Figure 6.1 shows a simple exemplary configuration, where GNRs can be coupled to graphene electrodes. Initially, nanoscale gaps can be patterned using electron beam lithography in a single layer of graphene. This is followed by oxygen plasma etching in which exposed graphene in the nanogaps is removed. In the next step, a single layer of GNRs is transferred on top of the graphene. There, the carbon atoms in GNRs and graphene can form physical bonds, resulting in the reduction of the contact resistance. Additionally, there would be no short channel effects, and the electrodes do not impose any restriction on coupling of incident light to the GNRs.

In addition to implement of photodetection using GNRs, the same fabricated devices can be employed to investigate the merits of GNRs for different directions. One idea is to study electroluminescence (EL) emission from the GNRs. The EL emission has been reported from single 7–AGNRs on top of a gold substrate [71]. There, the injection of carriers has been implemented by applying a voltage between a scanning tunneling microscopy tip and the substrate. This can be explored using our simple devices. Graphene has been recently used to develop high-speed blackbody radiators [103, 107]. The GNRs could be used similarly with the advantage that the emission is expected to have polarization selectivity.

Bibliography

1. Senkovskiy, B. V. *et al.,* “Making Graphene Nanoribbons Photoluminescent”, Nano Letters **17** 4029–4037 (2017).
2. Alavi, S. K. *et al.,* “Probing the origin of photoluminescence brightening in graphene nanoribbons”, 2D Materials **6** 035009 (2019).
3. Alavi, S. K. *et al.,* “Photodetection Using Atomically Precise Graphene Nanoribbons”, ACS Applied Nano Materials **3** 8343–8351 (2020).
4. Wang, G. *et al.,* “Colloquium: Excitons in atomically thin transition metal dichalcogenides”, Reviews of Modern Physics **90** 021001 (2018).
5. Geim, A. K. & Grigorieva, I. V., “Van der Waals heterostructures”, Nature **499** 419–425 (2013).
6. Novoselov, K. S., Mishchenko, A., Carvalho, A. & Castro Neto, A. H., “2D materials and van der Waals heterostructures”, Science **353** 461 (2016).
7. Liu, Y. *et al.,* “Van der Waals heterostructures and devices”, Nature Reviews Materials **1** 1–17 (2016).
8. Yap, Y. K. & Zhou, Z., “Two-Dimensional Electronics and Optoelectronics” (MDPI, 2018).
9. Palacios-Berraquero, C. *et al.,* “Large-scale quantum-emitter arrays in atomically thin semiconductors”, Nature Communications **8** 1–6 (2017).
10. Exarhos, A. L., Hopper, D. A., Patel, R. N., Doherty, M. W. & Bassett, L. C., “Magnetic-field–dependent quantum emission in hexagonal boron nitride at room temperature”, Nature Communications **10** 1 (2019).
11. Kianinia, M. *et al.,* “All–optical control and super-resolution imaging of quantum emitters in layered materials”, Nature Communications **9** 874 (2018).
12. Yan, Y. *et al.,* “Recent Advances on Graphene Quantum Dots: From Chemistry and Physics to Applications”, Advanced Materials **31** 1808283 (2019).
13. Yeh, T. F. *et al.,* “Elucidating Quantum Confinement in Graphene Oxide Dots Based on Excitation-Wavelength-Independent Photoluminescence”, Journal of Physical Chemistry Letters **7** 2087–2092 (2016).
14. Ye, R. *et al.,* “Bandgap engineering of coal-derived graphene quantum dots”, ACS Applied Materials and Interfaces **7** 7041–7048 (2015).

15. Moreno, C. *et al.,* “Bottom-up synthesis of multifunctional nanoporous graphene”, Science **360** 199–203 (2018).
16. Corso, M., Carbonell-Sanromà, E. & de Oteyza, D. G., “Bottom-Up Fabrication of Atomically Precise Graphene Nanoribbons, In: On-Surface Synthesis II ” (eds de Oteyza, D. G. & Rogero, C.) 113–152 (Springer, Cham, 2018).
17. Talirz, L., Ruffieux, P. & Fasel, R., “On-Surface Synthesis of Atomically Precise Graphene Nanoribbons”, Advanced Materials **28** 6222–6231 (2016).
18. Narita, A. *et al.,* “Bottom-up synthesis of liquid-phase-processable graphene nanoribbons with near-infrared absorption”, ACS Nano **8** 11622–11630 (2014).
19. Cai, J. *et al.,* “Atomically precise bottom-up fabrication of graphene nanoribbons”, Nature **466** 470–473 (2010).
20. Li, X., Wang, X., Zhang, L., Lee, S. & Dai, H., “Chemically derived, ultrasmooth graphene nanoribbon semiconductors”, Science **319** 1229–1232 (2008).
21. Son, Y. W., Cohen, M. L. & Louie, S. G., “Energy gaps in graphene nanoribbons”, Phys. Rev. Lett. **97** (2006).
22. Barone, V., Hod, O. & Scuseria, G. E., “Electronic structure and stability of semiconducting graphene nanoribbons”, Nano Letters **6** 2748–2754 (2006).
23. Celis, A. *et al.,* “Graphene nanoribbons: Fabrication, properties and devices”, Journal of Physics D: Applied Physics **49** 143001 (2016).
24. Duttaa, S. & Pati, S. K., “Novel properties of graphene nanoribbons: a review”, J. Mater. Chem. **20** 8207–8223 (2010).
25. Ruffieux, P. *et al.,* “Electronic Structure of Atomically Precise Graphene Nanoribbons”, ACS Nano **6** 6930–6935 (2012).
26. Wang, X. & Shi, Y., “Fabrication techniques of graphene nanostructures”, RSC Nanoscience and Nanotechnology **2014** 1–30 (2014).
27. Shi, Z. *et al.,* “Patterning Graphene with Zigzag Edges by Self-Aligned Anisotropic Etching”, Advanced Materials **23** 3061–3065 (2011).
28. Bai, J., Zhong, X., Jiang, S., Huang, Y. & Duan, X., “Graphene nanomesh”, Nature Nanotechnology **5** 190–194 (2010).
29. Han, M. Y., Brant, J. C. & Kim, P., “Electron transport in disordered graphene nanoribbons”, Phys. Rev. Lett. **104** 056801 (2010).
30. Sik Hwang, W. *et al.,* “Graphene nanoribbon field-effect transistors on wafer-scale epitaxial graphene on SiC substrates”, APL Materials **3** 11101 (2015).
31. Bryan, S. E., Yang, Y. & Murali, R., “Conductance of Epitaxial Graphene Nanoribbons: Influence of Size Effects and Substrate Morphology”, The Journal of Physical Chemistry C **115** 10230–10235 (2011).

32. Qi, Z. J. *et al.,*
“Correlating Atomic Structure and Transport in Suspended Graphene Nanoribbons”,
Nano Letters **14** 4238–4244 (2014).

33. Kosynkin, D. V. *et al.,*
“Longitudinal unzipping of carbon nanotubes to form graphene nanoribbons”,
Nature **458** 872–876 (2009).

34. Wei, D. *et al.,* “Controllable unzipping for intramolecular junctions of graphene nanoribbons and single-walled carbon nanotubes”, Nature Communications **4** 1374 (2013).

35. Vo, T. H. *et al.,* “Large-scale solution synthesis of narrow graphene nanoribbons”,
Nature Communications **5** 3189 (2014).

36. Gröning, O. *et al.,*
“Engineering of robust topological quantum phases in graphene nanoribbons”,
Nature **560** 209–213 (2018).

37. Rizzo, D. J. *et al.,* “Topological band engineering of graphene nanoribbons”,
Nature **560** 204–208 (2018).

38. Merino-Díez, N. *et al.,* “Width-Dependent Band Gap in Armchair Graphene Nanoribbons Reveals Fermi Level Pinning on Au(111)”, ACS Nano **11** 11661–11668 (2017).

39. Wang, W.-X. *et al.,*
“Energy gaps of atomically precise armchair graphene sidewall nanoribbons”,
Phys. Rev. B **93** 241403 (2016).

40. Kimouche, A. *et al.,* “Ultra-narrow metallic armchair graphene nanoribbons”,
Nature Communications **7** 10177 (2015).

41. Costa, P. S., Teeter, J. D., Enders, A. & Sinitskii, A.,
“Chevron-based graphene nanoribbon heterojunctions: Localized effects of lateral extension and structural defects on electronic properties”, Carbon **134** 310–315 (2018).

42. Kawai, S. *et al.,* “Atomically controlled substitutional boron-doping of graphene nanoribbons”,
Nature Communications **6** 8098 (2015).

43. Basagni, A. *et al.,* “Molecules-oligomers-nanowires-graphene nanoribbons: A bottom-up stepwise on-surface covalent synthesis preserving long-range order”,
Journal of the American Chemical Society **137** 1802–1808 (2015).

44. Lipton-Duffin, J. A., Ivasenko, O., Perepichka, D. F. & Rosei, F.,
“Synthesis of Polyphenylene Molecular Wires by Surface-Confined Polymerization”,
Small **5** 592–597 (2009).

45. Blankenburg, S. *et al.,*
“Intraribbon Heterojunction Formation in Ultranarrow Graphene Nanoribbons”,
ACS Nano **6** 2020–2025 (2012).

46. Koch, M., Ample, F., Joachim, C. & Grill, L.,
“Voltage-dependent conductance of a single graphene nanoribbon”,
Nature Nanotechnology **7** 713–717 (2012).

47. Richter, N. *et al.,*
“Charge transport mechanism in networks of armchair graphene nanoribbons”,
Scientific Reports **10** 1–8 (2020).

48. Yang, L., Park, C.-H., Son, Y.-W., Cohen, M. L. & Louie, S. G.,
“Quasiparticle Energies and Band Gaps in Graphene Nanoribbons”, Phys. Rev. Lett. **99** 186801 (2007).

49. Yang, L., Cohen, M. L. & Louie, S. G.,
“Excitonic Effects in the Optical Spectra of Graphene Nanoribbons”,
Nano Letters **7** 3112–3115 (2007).

50. Cloke, R. R. *et al.,* “Site-Specific Substitutional Boron Doping of Semiconducting Armchair Graphene Nanoribbons”, Journal of the American Chemical Society **137** 8872–8875 (2015).

51. De Oteyza, D. G. *et al.,*
“Substrate-Independent Growth of Atomically Precise Chiral Graphene Nanoribbons”,
ACS Nano **10** 9000–9008 (2016).

52. Prezzi, D., Varsano, D., Ruini, A., Marini, A. & Molinari, E.,
“Optical properties of graphene nanoribbons: The role of many-body effects”,
Phys. Rev. B **77** 041404 (2008).

53. Ruffieux, P. *et al.,* “On–surface synthesis of graphene nanoribbons with zigzag edge topology”, Nature **531** 489–492 (2016).

54. Li, Y. Y., Chen, M. X., Weinert, M. & Li, L., “Direct experimental determination of onset of electron-electron interactions in gap opening of zigzag graphene nanoribbons”,
Nature Communications **5** 4311 (2014).

55. Ruffieux, P. *et al.,* “Electronic Structure of Atomically Precise Graphene Nanoribbons”,
ACS Nano **6** 6930–6935 (2012).

56. Denk, R. *et al.,* “Exciton-dominated optical response of ultra-narrow graphene nanoribbons”, Nature Communications **5** 4253 (2014).

57. Talirz, L. *et al.,* “On-Surface Synthesis and Characterization of 9-Atom Wide Armchair Graphene Nanoribbons”, ACS Nano **11** 1380–1388 (2017).

58. Chen, Y. C. *et al.,*
“Tuning the band gap of graphene nanoribbons synthesized from molecular precursors”,
ACS Nano **7** 6123–6128 (2013).

59. Ma, C. *et al.,*
“Seamless Staircase Electrical Contact to Semiconducting Graphene Nanoribbons”,
Nano Letters **17** 6241–6247 (2017).

60. Garcia-Lastra, J. M. & Thygesen, K. S.,
“Renormalization of optical excitations in molecules near a metal surface”,
Phys. Rev. Lett. **106** (2011).

61. Maultzsch, J. *et al.,*
“Exciton binding energies in carbon nanotubes from two-photon photoluminescence”,
Phys. Rev. B **72** 241402R (2005).

62. Yu, P. Y. & Cardona, M.,
"Fundamentals of Semiconductors–Physics and Materials Properties" 4th ed.
(Springer, Berlin, Heidelberg, 2010).

63. Dresselhaus, M. S., "SOLID STATE PHYSICS PART II Optical Properties of Solids", 2005.

64. Berciaud, S., Cognet, L. & Lounis, B., "Luminescence decay and the absorption cross section of individual single-walled carbon nanotubes", Phys. Rev. Lett. **101** 077402 (2008).

65. Piao, Y. *et al.,*
"Brightening of carbon nanotube photoluminescence through the incorporation of sp^3 defects",
Nature Chemistry **5** 840–845 (2013).

66. Harutyunyan, H. *et al.,* "Defect-Induced Photoluminescence from Dark Excitonic States in Individual Single-Walled Carbon Nanotubes", Nano Letters **9** 2010–2014 (2009).

67. Miyauchi, Y. *et al.,*
"Brightening of excitons in carbon nanotubes on dimensionality modification",
Nature Photonics **7** 715–719 (2013).

68. Fox, M., "Quantum optics : an introduction" 378 (Oxford University Press, 2006).

69. Hsu, H. & Reichl, L. E., "Selection rule for the optical absorption of graphene nanoribbons", Phys. Rev. B **76** 045418 (2007).

70. Liao, W., Zhou, G. & Xi, F., "Optical properties for armchair-edge graphene nanoribbons", Journal of Applied Physics **104** 126105 (2008).

71. Chong, M. C. *et al.,*
"Bright Electroluminescence from Single Graphene Nanoribbon Junctions",
Nano Letters **18** 175–181 (2018).

72. Kasha, M., "Characterization of electronic transitions in complex molecules",
Discussions of the Faraday Society **9** 14–19 (1950).

73. Cardoso, C., Ferretti, A. & Prezzi, D.,
"Termini effects on the optical properties of graphene nanoribbons",
European Physical Journal B **91** (2018).

74. Huang, Y. *et al.,* "Intrinsic Properties of Single Graphene Nanoribbons in Solution: Synthetic and Spectroscopic Studies", Journal of the American Chemical Society **140** 10416–10420 (2018).

75. Luo, Y. *et al.,* "Purcell-enhanced quantum yield from carbon nanotube excitons coupled to plasmonic nanocavities", Nature Communications **8** 1 (2017).

76. Perebeinos, V. & Avouris, P.,
"Phonon and electronic nonradiative decay mechanisms of excitons in carbon nanotubes",
Phys. Rev. Lett. **101** 057401 (2008).

77. Matsuda, K., Miyauchi, Y., Sakashita, T. & Kanemitsu, Y.,
"Nonradiative exciton decay dynamics in hole-doped single-walled carbon nanotubes",
Phys. Rev. B **81** 033409 (2010).

78. Demtröder, W., "Laser Raman Spectroscopy" 149–181 (Springer Berlin Heidelberg, 2015).

79. Boyd, R. W., “Nonlinear Optics” (Elsevier Inc., 2008).
80. Dresselhaus, M. S., Dresselhaus, G., Saito, R. & Jorio, A., “Raman spectroscopy of carbon nanotubes”, Physics Reports **409** 47–99 (2005).
81. Kauffmann, T. H., Kokanyan, N. & Fontana, M. D., “Use of Stokes and anti-Stokes Raman scattering for new applications”, Journal of Raman Spectroscopy **50** 418–424 (2019).
82. Graf, D. *et al.,* “Spatially resolved raman spectroscopy of single- and few-layer graphene”, Nano Letters **7** 238–242 (2007).
83. No, Y. S. *et al.,* “Layer number identification of CVD-grown multilayer graphene using Si peak analysis”, Scientific Reports **8** (2018).
84. Eckmann, A. *et al.,* “Probing the nature of defects in graphene by Raman spectroscopy”, Nano Letters **12** 3925–3930 (2012).
85. Dresselhaus, M. S., Jorio, A., Souza Filho, A. G. & Saito, R., “Defect characterization in graphene and carbon nanotubes using Raman spectroscopy”, Trans. R. Soc. A **368** 5355–5377 (2010).
86. Reich, S. & Thomsen, C., “Raman spectroscopy of graphite”, Philosophical Transactions A: Mathematical, Physical and Engineering Sciences **362** 2271–2288 (2004).
87. Borin Barin, G. *et al.,* “Surface-Synthesized Graphene Nanoribbons for Room Temperature Switching Devices: Substrate Transfer and ex Situ Characterization”, ACS Applied Nano Materials **2** 2184–2192 (2019).
88. Grüneis, A., Senkovskiy, B. V., Fedorov, A. V., Hell, M. & Michel, S., “Ultrahigh vacuum optical spectroscopy of chemically functionalized graphene nanoribbons” 367–374 (Elsevier, 2018).
89. Verzhbitskiy, I. A. *et al.,* “Raman Fingerprints of Atomically Precise Graphene Nanoribbons”, Nano Letters **16** 3442–3447 (2016).
90. Binder, J., Stepniewski, R., Strupiński, W. & Wysmołek, A., “In Situ Raman Spectroscopy of Solution-Gated Graphene on Copper”, Acta Physica Polonica A **132** 360–361 (2017).
91. Yu, X., Shen, Y., Liu, T., Wu, T. & Jie Wang, Q., “Photocurrent generation in lateral graphene p-n junction created by electron-beam irradiation”, Scientific Reports **5** 12014 (2015).
92. Wall, M., “The Raman Spectroscopy of Graphene and the Determination of Layer Thickness”, Thermo Fisher Scientific 52252 (2011).
93. Reich, S., Thomsen, C. & Maultzsch, J., “Carbon nanotubes : basic concepts and physical properties” 145–158 (Wiley-VCH, 2004).
94. Casiraghi, C. *et al.,* “Raman Spectroscopy of Graphene Edges”, Nano Letters **9** 1433–1441 (2009).
95. Ferralis, N., “Probing mechanical properties of graphene with Raman spectroscopy”, J. Mater. Sci. **45** 5135–5149 (2010).

96. Zhou, J. & Dong, J., “Vibrational property and Raman spectrum of carbon nanoribbon”, Applied Physics Letters **91** 173108 (2007).

97. Zhao, S. *et al.,* “Optical Investigation of On-Surface Synthesized Armchair Graphene Nanoribbons”, physica status solidi (b) **254** 1700223 (2017).

98. Vandescuren, M., Hermet, P., Meunier, V., Henrard, L. & Lambin, P., “Theoretical study of the vibrational edge modes in graphene nanoribbons”, Phys. Rev. B **78** 195401 (2008).

99. Finge, T. *et al.,* “Investigations on Field-Effect Transistors Based on Two-Dimensional Materials”, Annalen der Physik **529** 1700087 (2017).

100. Tong, X., Ashalley, E., Lin, F., Li, H. & Wang, Z. M., “Advances in MoS_2 -Based Field Effect Transistors (FETs)”, Nano-Micro Letters **7** 203–218 (2015).

101. Britnell, L. *et al.,* “Resonant tunnelling and negative differential conductance in graphene transistors”, Nature Communications **4** 1794 (2013).

102. Shim, J. *et al.,* “Electronic and Optoelectronic Devices based on Two-Dimensional Materials: From Fabrication to Application”, Advanced Electronic Materials **3** 1600364 (2017).

103. Miyoshi, Y. *et al.,* “High–speed and on-chip graphene blackbody emitters for optical communications by remote heat transfer”, Nature Communications **9** 1279 (2018).

104. Itkis, M. E., Yu, A. & Haddon, R. C., “Single–Walled Carbon Nanotube Thin Film Emitter–Detector Integrated Optoelectronic Device”, Nano Letters **8** 2224–2228 (2008).

105. Liu, P. *et al.,* “Fast High-Temperature Response of Carbon Nanotube Film and Its Application as an Incandescent Display”, Advanced Materials **21** 3563–3566 (2009).

106. Mori, T., Yamauchi, Y., Honda, S. & Maki, H., “An Electrically Driven, Ultrahigh-Speed, on-Chip Light Emitter Based on Carbon Nanotubes”, Nano Letters **14** 3277–3283 (2014).

107. Shiue, R.-J. *et al.,* “Thermal radiation control from hot graphene electrons coupled to a photonic crystal nanocavity”, Nature Communications **10** 109 (2019).

108. Koppens, F. H. L. *et al.,* “Photodetectors based on graphene, other two–dimensional materials and hybrid systems”, Nature Nanotechnology **9** 780–793 (2014).

109. Ma, P. *et al.,* “Plasmonically Enhanced Graphene Photodetector Featuring 100 Gbit/s Data Reception, High Responsivity, and Compact Size”, ACS Photonics **6** 154–161 (2019).

110. Bennett Patrick, B. *et al.,* “Bottom-up graphene nanoribbon field-effect transistors”, Applied Physics Letters **103** 253114 (2013).

111. Passi, V. *et al.,* “Field-Effect Transistors Based on Networks of Highly Aligned, Chemically Synthesized N = 7 Armchair Graphene Nanoribbons”, ACS Appl. Mater. Interfaces **10** 9900–9903 (2018).

112. Ohtomo, M., Sekine, Y., Hibino, H. & Yamamoto, H., "Graphene nanoribbon field-effect transistors fabricated by etchant-free transfer from Au(788)", Appl. phys. Lett. **112** 021602 (2018).

113. "Short-channel field-effect transistors with 9-atom and 13-atom wide graphene nanoribbons", Nature Communications **8** 633 (2017).

114. Fairbrother, A. *et al.,* "High vacuum synthesis and ambient stability of bottom-up graphene nanoribbons", Nanoscale **9** 2785–2792 (2017).

115. Zaki, T., "Organic Thin-Film Transistors. In: Short-Channel Organic Thin-Film Transistors" 41–47 (Springer, 2015).

116. Wang, L. *et al.,* "One-dimensional electrical contact to a two-dimensional material", Science **342** 614–617 (2013).

117. Radisavljevic, B., Radenovic, A., Brivio, J., Giacometti, V. & Kis, A., "Single-layer MoS_2 transistors", Nature Nanotechnology **6** 147–150 (2011).

118. Lembke, D. & Kis, A., "Breakdown of high-performance monolayer MoS_2 transistors", ACS Nano **6** 10070–10075 (2012).

119. Liu, B. *et al.,* "High-Performance WSe_2 Field-Effect Transistors via Controlled Formation of In-Plane Heterojunctions", ACS Nano **10** 5153–5160 (2016).

120. Liu, E. *et al.,* "Integrated digital inverters based on two-dimensional anisotropic ReS_2 field-effect transistors", Nature Communications **6** 6991 (2015).

121. Obradovic, B. *et al.,* "Analysis of graphene nanoribbons as a channel material for field-effect transistors", Applied Physics Letters **88** 142102 (2006).

122. Jänsch, D. *et al.,* "Ultra-Narrow Low-Bandgap Graphene Nanoribbons from Bromoperylenes-Synthesis and Terahertz-Spectroscopy", Chemistry - A European Journal **23** 4870–4875 (2017).

123. Kaiser, A. B. & Skákalová, V., "Electronic conduction in polymers, carbon nanotubes and graphene", Chem. Soc. Rev. **40** 3786–3801 (2011).

124. Hong, W., Lee, E., Park, J. K. & Lee, C. E., "Charge transport and photoresponses in a single-stranded DNA/single-walled carbon nanotube composite film", J. Appl. Phys **113** 216101 (2013).

125. Cakmakyapan, S., Lu, P. K., Navabi, A. & Jarrahi, M., "Gold–patched graphene nano–stripes for high-responsivity and ultrafast photodetection from the visible to infrared regime", Nature Communications **7** 20 (2018).

126. Echtermeyer, T. J. *et al.,* "Photothermoelectric and Photoelectric Contributions to Light Detection in Metal–Graphene–Metal Photodetectors", Nano Letters **14** 3733–3742 (2014).

127. Furchi, M. M., Polyushkin, D. K., Pospischil, A. & Mueller, T., "Mechanisms of Photoconductivity in Atomically Thin MoS_2", Nano Letters **14** 6165–6170 (2014).

128. Yao, Y. *et al.,* “High-Responsivity Mid-Infrared Graphene Detectors with Antenna- Enhanced Photocarrier Generation and Collection”, Nano Letters **14** 3749–3754 (2014).
129. Huang, M. *et al.,* “Broadband Black-Phosphorus Photodetectors with High Responsivity”, Advanced Materials **28** 3481–3485 (2016).
130. Suess, R. J. *et al.,* “Mid-infrared time-resolved photoconduction in black phosphorus”, 2D Materials **3** 041006 (2016).
131. Chakraborty, C. *et al.,* “Optical antenna enhanced graphene photodetector”, Appl. Phys. Lett. **105** 241114 (2014).
132. Shiue, R.-J. *et al.,* “High–Responsivity Graphene–Boron Nitride Photodetector and Autocorrelator in a Silicon Photonic Integrated Circuitr”, Nano Letters **15** 7288–7293 (2016).
133. Shi, S. F., Xu, X., Ralph, D. C. & McEuen, P. L., “Plasmon Resonance in Individual Nanogap Electrodes Studied Using Graphene Nanoconstrictions as Photodetectors”, Nano Letters **11** 1814–1818 (2011).
134. Freitag, M. *et al.,* “Photocurrent in graphene harnessed by tunable intrinsic plasmons”, Nature Communications **4** 1951 (2013).
135. Xia, F., Mueller, T., Lin, Y.-M., Valdes-Garcia, A. & Avouris, P., “Ultrafast graphene photodetector”, Nature Nanotechnology **4** 839–843 (2009).
136. Gan, X. *et al.,* “Graphene and graphene-like two-dimensional materials in photodetection: mechanisms and methodology”, Nature Photonics **8** 5 (2014).
137. Lopez-Sanchez, O., Lembke, D., Kayci, M., Radenovic, A. & Kis, A., “Ultrasensitive photodetectors based on monolayer MoS_2”, Nature Nanotechnology **8** 497–501 (2013).
138. Liu, Y. *et al.,* “Plasmon resonance enhanced multicolour photodetection by graphene”, Nature Communications **2** 579 (2011).
139. Lemme, M. C. *et al.,* “Gate–Activated Photoresponse in a Graphene p–n Junction”, Nano Letters **11** 4134–4137 (2011).
140. Rao, G., Freitag, M., Chiu, H.-Y., Sundaram, R. S. & Avouris, P., “Raman and Photocurrent Imaging of Electrical Stress-Induced p–n Junctions in Graphene”, ACS Nano **7** 5848–5854 (2011).
141. Freitag, M., Martin, Y., Misewich, J. A., Martel, R. & Avouris, P., “Photoconductivity of Single Carbon Nanotubes”, Nano Letters **3** 1067–1071 (2003).
142. Bartolomeo, A. D. *et al.,* “Electrical transport and persistent photoconductivity in monolayer MoS_2 phototransistors”, Nanotechnology **28** 21 (2017).
143. Freitag, M., Low, T., Xia, F. & Avouris, P., “Photoconductivity of biased graphene”, Nature Photonics **7** 53–59 (2013).
144. Fang, J. *et al.,* “Enhanced Graphene Photodetector with Fractal Metasurface”, Nano Letters **17** 57–62 (2017).
145. Gabor, N. M. *et al.,* “Hot Carrier–Assisted Intrinsic Photoresponse in Graphene”, Science **334** 648–652 (2011).

146. Buscema, M. *et al.,* "Large and Tunable Photothermoelectric Effect in Single-Layer MoS_2", Nano Letters **13** 358–363 (2013).

147. Han, Q. *et al.,* "Highly sensitive hot electron bolometer based on disordered graphene", Scientific Reports **3** 3533 (2013).

148. Yan, J. *et al.,* "Dual-gated bilayer graphene hot-electron bolometer", Nature Nanotechnology **7** 472–478 (2012).

149. Zhang, S. *et al.,* "Bolometric–Effect-Based Wavelength-Selective Photodetectors Using Sorted Single Chirality Carbon Nanotubes", Scientific Reports **5** 17883 (2015).

150. Mueller, T., Xia, F. & Avouris, P., "Graphene photodetectors for high-speed optical communications", Nature Photonics **4** 297–301 (2010).

151. Xia, F. *et al.,* "Photocurrent Imaging and Efficient Photon Detection in a Graphene Transistor", Nano Letters **9** 1039–1044 (2009).

152. Garcia, C., Pradhan, N. R., Rhodes, D., Balicas, L. & McGill, S. A., "Photogating and high gain in ReS_2 field-effect transistors", Journal of Applied Physics **124** 204306 (2018).

153. Lee, H., Ahn, J., Im, S., Kim, J. & Choi, W., "High-Responsivity Multilayer MoS_2 Phototransistors with Fast Response Time", Scientific Reports **8** 1–7 (2018).

154. Yamamoto, M., Ueno, K. & Tsukagoshi, K., "Pronounced photogating effect in atomically thin WSe_2 with a self-limiting surface oxide layer", Applied Physics Letters **112** 181902 (2018).

155. Fang, H. & Hu, W., "Photogating in Low Dimensional Photodetectors", Advanced Science **4** 1700323 (2017).

156. He, X. *et al.,* "Carbon nanotubes as emerging quantum–light sources", Nature Materials **17** 663–670 (2018).

157. Kwon, H. *et al.,* "Molecularly Tunable Fluorescent Quantum Defects", Journal of the American Chemical Society **138** 6878–6885 (2016).

158. Chatterjee, R., Pavlovetc, I. M., Aleshire, K. & Kuno, M., "Single Semiconductor Nanostructure Extinction Spectroscopy", Journal of Physical Chemistry C **122** 16443–16463 (2018).

159. Brozena, A. H., Kim, M., Powell, L. R. & Wang, Y. H., "Controlling the optical properties of carbon nanotubes with organic colour-centre quantum defects", Nature Reviews Chemistry **3** 375–392 (2019).

160. He, X. *et al.,* "Tunable room-temperature single-photon emission at telecom wavelengths from sp^3 defects in carbon nanotubes", Nature Photonics **11** 577–582 (2017).

161. Paulus, G. L., Wang, Q. H. & Strano, M. S., "Covalent electron transfer chemistry of graphene with diazonium salts", Accounts of Chemical Research **46** 160–170 (2013).

162. Pfeiffer, M. *et al.,* "Observation of Room-Temperature Photoluminescence Blinking in Armchair-Edge Graphene Nanoribbons", Nano Letters **18** 7038–7044 (2018).

163. Liu, C. H., Chang, Y. C., Norris, T. B. & Zhong, Z., "Graphene photodetectors with ultra-broadband and high responsivity at room temperature", Nature Nanotechnology **9** 273–278 (2014).

164. Chen, Z. *et al.,* "Lateral Fusion of Chemical Vapor Deposited N = 5 Armchair Graphene Nanoribbons", Journal of the American Chemical Society **139** 9483–9486 (2017).

165. Lin, Y. *et al.,* "Asymmetric hot-carrier thermalization and broadband photoresponse in graphene-2D semiconductor lateral heterojunctions", Science Advances **5** 1493 (2019).

APPENDIX A

Experimental setups

In this chapter, the typical confocal microscopy setups used in this work are shown in the following figures. The Fig. A.1 is the setup to study photoluminescence at room temperature. A supercontinuum source is fiber coupled (using a photonic crystal fiber, PCF) to a wavelength selector module to cover the wavelength range from 400 to 800 nm. In order to narrow the spectrum, the output is diffracted by a grating (G), passed through an adjustable slit (S), and reflected via the grating into the setup. The light is coupled to the setup using 50:50 beamsplitter (BS), directing the beam toward a microscope objective (Obj) and eventually to the sample. The back reflection and possible emission from the sample surface are collected by Obj. The CCD camera is used to check the reflection from the surface. In the emission pass the light reflected from the sample is filtered (F) in order to resolve the emission from the sample. A pinhole (PH) is used for spatial filtering before a single photon counting module (SPCM). The emission spectra can be measured using a grating spectrometer equipped with a deep-cooled back-illuminated CCD. The polarization configuration of the beam is set using polarizers (PL) and wave plates ($\lambda/2$ or $\lambda/4$). The lenses are labeled (L). Figure A.2 shows a similar setup as in Fig. A.1, which has been used to measure Raman spectra for a broad range of excitation wavelengths. In this setup a home-built tunable grating filter is implemented in which the diffracted light is filtered using an adjustable sharp beam blocker (R).

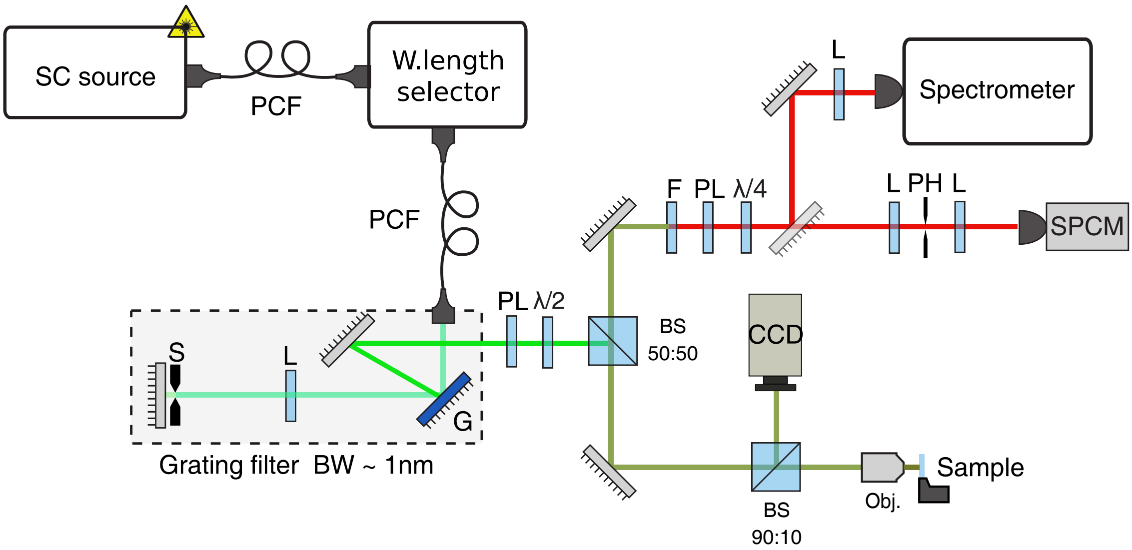

Figure A.1: Schematic of confocal microscopy setup to measure PL emission.

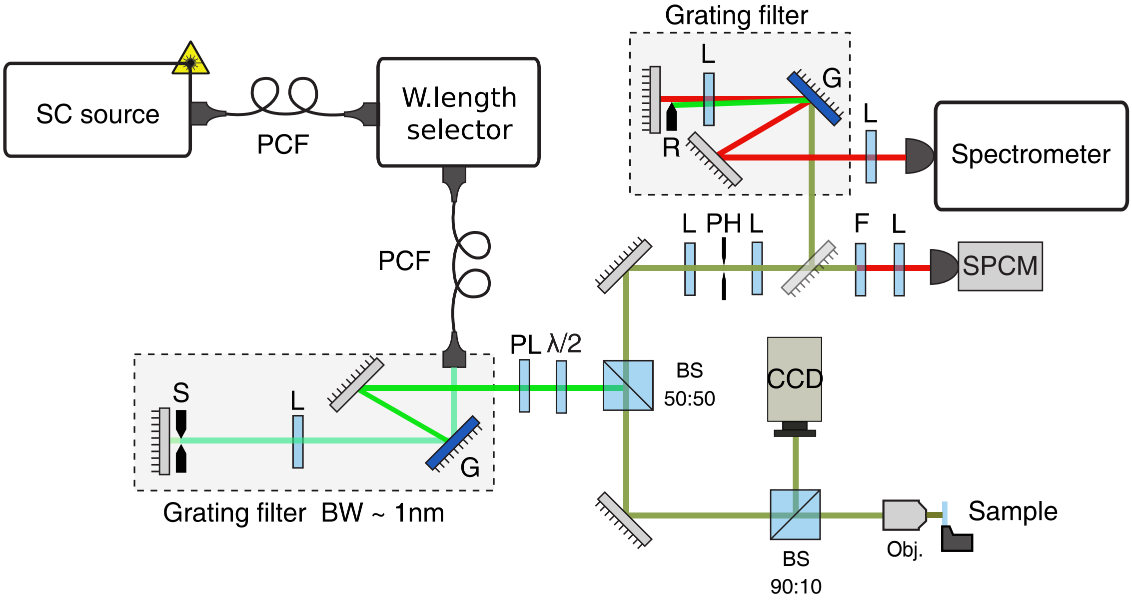

Figure A.2: A schematic of confocal microscopy setup to measure Raman scattering for a broad range of excitation wavelengths.

List of Acronyms

AFM atomic force microscopy.

CNTs carbon nanotubes.

DFT density functional theory.

EL electroluminescence.

FETs field-effect transistors.
FP free particle.

GNRs graphene nanoribbons.
GQDs graphene quantum dots.

hBN hexagonal boron nitride.

PC photoconductive.
PD photodetector.
PG photogating.
PL photoluminescence.
PTE photo-thermoelectric.
PV photovoltaic.

RBLM radial breathing like mode.

SPE single photon emission.
STM scanning tunneling microscope.
STS scanning tunneling spectroscopy.
SWCNTs single-walled CNTs.

TEM transmission electron microscopy.
TMDs transition metal dichalcogenides.

Acknowledgments

This work reflects a part of my life in the last four years, that was the most intense period which I experienced so far, with many challenges and exciting moments. This work is very precious for me not only for bringing me to the next level of my academic life but because it helped me to trust myself. This, however, was not achievable without the help and support of many pleasant people. I would like to take this opportunity and express my all gratitude to them in the following paragraphs.

First of all, I would like to thank Prof. Klas Lindfors for all his great supports, guiding, and encouragements, and importantly, for trusting me in my *unusual* situation when I wanted to join his group. It was a great pleasure to work in his diverse and friendly group. Thanks Klas for giving me the opportunity to work in such an exciting research area. I am really grateful to him for shaping my academic life with all his points, feedbacks, and comments and being always available for fruitful discussions. I had a great chance to work with such a responsible and positive thinking person I did not meet before.

I would also like to thank Prof. Dieter Meschede, who made it possible for me to come to Germany and start my next academic studies. I am grateful to him for all his supports and help in particular to resolve my administrative issues at University of Bonn. I would always remember his advice. It was a great chance for me to work in his fantastic group, although for a short period, in which I have learned lots of experimental points. I would also thank him for being my second supervisor and for reviewing this thesis.

I am thankful to our collaborators that made this work possible, to Prof. Yoichi Ando, Prof. Klaus Meerholz, and Dr. Dirk Hertel for all the supports; and in particular to Prof. Alexander Grüneis and his postdoc fellow, Dr. Boris V. Senkovskiy to provide the GNRs samples, many amazing meetings, and for the support with the DAAD extensions. I am grateful to him for being a member of my teaching advisory committee (TAC).

I acknowledge the Bonn Cologne graduate school (BCGS) and the German Academic Exchange Service (DAAD) for grants and financial supports. I would also like to thank Dagmar Hosseini-Razi for her important and helpful advice and other members of DAAD office for their support particularly when they gave me more time during my research transition.

I would like to express my gratitude to the staff members of IAP at University of Bonn and the physical chemistry institute (PC) at University of Cologne in particular to Annelise Miglo for her help and Peter Müller for useful discussions and being a reliable source of electronic components. I am really grateful to the members of the mechanical workshop at the PC particularly to Viktor Klippert for providing super precise and complicated equipment for our experiments.

I would extend my thanks to the members of both Prof. Klas Lindfors and Prof. Dieter Meschede groups, with whom we had a great time together. I am really indebted to everyone from whom I learned many technical points. To Dr. Markus Pfeiffer for the help and great collaboration. To Dr. Igor Shavrin for *non-stoppable* useful chats. To Mo Lu and Lukas Böhner for sharing the interesting ideas, offices, stories, . . . , and for all the good moments.

In the end, to my family and my wife to whom I would dedicate this thesis, because of all the love, patents and motivations. My special thanks go to my father-in-law Prof. Gholamali Fallah for being a continuous source of stimulation and encouragement and for asking the every-week question: "*How is it going with the thesis?* ".